Numerical study on turbulence induced vibrations of fuel rods

Using an Anisotropic Pressure Fluctuations Model

André Freitas

Delft University of Technology

TU Delft

This page intentionally left blank.

Numerical study on turbulence induced vibrations of fuel rods

Using an Anisotropic Pressure Fluctuations Model

by

André Freitas

to obtain the degree of Master of Science
at the Delft University of Technology,
to be defended publicly on Monday October 9, 2023 at 14:00.

Student number:	5600359	
Project duration:	December 1, 2022 – 31 August, 2023	
Thesis committee:	Dr. ir. M.I. Gerritsma,	TU Delft, chair
	Dr. ir. F. de Prenter,	TU Delft, examiner
	ir. K. Zwijsen,	NRG, supervisor
	Dr. ir. A.H. Van Zuijlen,	TU Delft, supervisor

This thesis is confidential and cannot be made public until October 9, 2025.

Cover: Figure by Kerttu Jaatinen.

An electronic version of this thesis is available at `http://repository.tudelft.nl/`.

TU Delft

NRG

This page intentionally left blank.

Preface

When I started this thesis about 10 months ago, I had no idea of the journey this would be. Through its ups and downs, it provided me with invaluable lessons both in academic terms as well as personally. I would like to thank Kevin and Sander for this opportunity and for your knowledge through the many meetings we had. Your insight and critical perspective pushed me to perform better and conduct more thorough research. Moreover, I would like to express my gratitude to the entire CFD department at NRG for being welcoming and always open for discussions. Specifically, I want to thank Sina. Your help early on the project was crucial in setting the pace and laying the foundation for the coming months.

I'd also like to extend my appreciation to my friends from Portugal for always being there, and to my friends from Delft for making these past two years memorable. Finally, I want to thank my family: Mãe, Pai, and Hugo. Your unwavering support has been the greatest gift throughout my education and life, and it was instrumental in getting me through my thesis. I am profoundly grateful to have you in my life.

André Freitas
Delft, September 2023

This page intentionally left blank.

Abstract

In the evolving landscape of nuclear energy, ensuring the safety and efficiency of nuclear reactors remains paramount, particularly with the increasing demands for energy and a concurrent rise in global temperatures. A significant aspect of nuclear safety involves maintaining the integrity of the fuel rods, which are susceptible to Turbulence Induced Vibrations (TIV) resulting from axial flows of the coolant liquid. TIV can instigate severe repercussions including structural damage such as fatigue, wear, and stress corrosion cracking, posing substantial threats to reactor safety. Despite the historical attention this phenomenon has garnered since the 1950s, conventional semi-empirical methods offer limited predictive accuracy and do not facilitate extrapolations for multi-rod scenarios effectively.

Recent developments have turned to Fluid-Structure Interaction (FSI) simulations as a powerful tool to study fuel rods' behavior under TIV effects, capitalizing on the increase of computational power available today. While Direct Numerical Simulation (DNS) and Large Eddy Simulation (LES) offer more accurate predictions, their computational demands make them unsuitable for complex FSI simulations. This has led to a preference for Unsteady Reynolds-Averaged Navier-Stokes (URANS) simulations, despite them underpredicting the displacement amplitudes of the vibrations.

Evolving from this shortfall, the current study directs its focus on a recently developed Anisotropic Pressure Fluctuation Model (AniPFM). This model generates a synthetic velocity fluctuations field, which is used to solve for the pressure fluctuations. The use of this model together with URANS poses as a possible way to inexpensively simulate the excitation mechanisms of TIV of fuel rods. While previous research has highlighted the potential of this model, it is important to note the considerable level of uncertainty still associated with it. Additionally, there are parameters, definitions and constants whose impacts on the model are not yet fully understood or even explored. This calls for a comprehensive research to fine-tune the model, optimize its performance and further validate it. This is precisely the goal of this study, carried out through the analysis of two pure flow and two FSI cases. Hypotheses were formulated and tested in pure flow scenarios before being further validated in FSI cases. Key advancements were made by optimizing the time correlation method used on the generated velocity fluctuations, which significantly reduced the model's uncertainty. This method was then calibrated using DNS data of turbulent channel flow. Further calibration was undertaken, this time in the parameters part of the modelling of the turbulent kinetic energy spectrum, to address the overprediction of pressure fluctuations near the wall observed in the baseline model. Moreover, the turbulent annular flow was used as the second flow only case, providing more complexity compared to channel flow, by adding curvature, as well as another opportunity to test the hypothesis made.

Furthermore, the hypotheses underwent additional validation via FSI simulations, through a brass beam in turbulent axial flow, showing a substantial decrease in the average difference from the experimental data to 19% from a previous 68%, over the range of inflow velocities considered. Notably, the calibrated AniPFM surpassed LES in accuracy while requiring fewer computational resources. The results obtained are promising, but further validation is needed. This thesis also outlines and lays the foundation for further validation work, through the setup and initial simulations of a flexible cantilever rod in turbulent axial water flow.

This page intentionally left blank.

Contents

This page intentionally left blank.

List of Figures

This page intentionally left blank.

List of Tables

This page intentionally left blank.

Nomenclature

Acronyms

ALE	Arbitrary Lagrangian-Eulerian
AniPFM	Anisotroppic Pressure Fluctuation Model
BC	Boundary Condition
BL	Boundary Layer
BWR	Boiling Water Reactor
C&EC	Convection & Exponential Correlation
CFD	Computational Fluid Dynamics
CFL	Courant–Friedrichs–Lewy
CPS	Conventional Parallel Staggered
CSM	Computational Structural Solid Mechanics
CSS	Conventional Serial Staggered
DNS	Direct Numerical Simulation
EARSM	Explicit Algebraic Reynolds Stress Model
EIE	Extraneously Induced Excitation
EVM	Eddy Viscosity Model
FIV	Flow Induced Vibrations
FSI	Fluid-Structure Interaction
HIT	Homogeneous Isotropic Turbulence
IQN-ILS	Interface Quasi Newton Inverse Least Squares
LES	Large Eddy Simulation
MIE	Movement Induced Excitation
NRG	Nuclear Research & consultancy Group
NS	Navier-Stokes
ODE	Ordinary Differential Equation
PC	Pure Convection
PDE	Partial Differential Equation
pdf	Probability Density Function
PFM	Pressure Fluctuation Model

PIV	Particle Image Velocimetry
PWR	Pressurised Water Reactor
RANS	Reynolds averaged Navier Stokes
RC&EC	Rescaled Convection & Exponential Correlation
RHS	Right Hand Side
RMS	Root Mean Square
RNG	Random Number Generator
RSM	Reynolds Stress Model
RST	Reynolds Stress Tensor
SGS	Subgrid Scale
SSG	Speziale, Sarkar & Gatsk
SST	Shear Stress Transport
ST	Synthetic Turbulence
TCF	Turbulent Channel Flow
TIV	Turbulence Induced Vibrations
TKE	Turbulent Kinetic Energy
UQ	Uncertainty Quantification
URANS	Unsteady Reynolds Averaged Navier Stokes

Greek Symbols

α	Empirical coefficient	-
β	Empirical coefficient	-
γ	Complex scaling factor	-
δ	Half of the height of the channel	-
δ_{ij}	Kronecker delta	-
ϵ	Dissipation rate	$m^2\,s^{-3}$
ϵ_{kl}	Strain tensor	-
ζ	Damping ratio	-
$\boldsymbol{\zeta_n}$	Auxiliary vector	-
η	Kolmogorov length scale	m
θ_n	Random variable	rad
μ	Kinematic viscosity	$m^2\,s^{-1}$
μ_t	Kinematic eddy viscosity	$m^2\,s^{-1}$
ν	Dynamic viscosity	$kg\,m^{-1}\,s^{-1}$
ρ	Density	$kg\,m^{-3}$
σ_{ij}	Stress tensor	Pa
$\boldsymbol{\sigma_n}$	Direction vector	-
τ	Characteristic time scale	s
τ_w	Wall shear stress	Pa
τ_η	Kolmogorov time scale	s
τ_{ij}	Context 1: Viscous stress tensor	Pa
	Context 2: Reynolds stress tensor	$m^2\,s^{-2}$
$\phi_{pp}(\omega)$	Angular frequency power spectrum of pressure fluctuations	$kg^2\,m^{-2}\,s^{-3}$

$\phi_{pp}(k_i)$	Wavenumber power spectrum of pressure fluctuations	$kg^2\,m^{-1}\,s^{-1}$
ϕ_n	Phase shift	rad
ϕ_{ij}	Pressure-strain correlation tensor	$m^2\,s^{-3}$
ψ_n	Random variable	rad
ω	Context 1: Specific turbulent dissipation rate	s^{-1}
	Context 2: Angular frequency	s^{-1}

Roman Symbols

a	C&EC coefficient	-
a_{ij}	Part of the Cholesky decomposition of the Reynolds stress tensor	-
b	C&EC coefficient	-
C_l	Empirical constant	-
D	Diameter	m
d	Distance	m
E	Context 1: Young modulus	Pa
E	Context 2: Energy spectrum	$m^3\,s^{-2}$
f	Frequency	s^{-1}
f_τ	Correlation factor	-
h	Height	m
I	Moment of inertia	$kg\,m^2$
k	Context 1: turbulent kinetic energy	$m^2\,s^{-2}$
k	Context 2: wavenumber	m^{-1}
L	Length	m
l	Length scale	m
l_t	RANS length scale	m
M	Bending moment	N m
p	Pressure	m
q_n	Non-dimensional energy	-
r	Radius / radial position	m
R_{ii}	Two point correlation	-
u_i	Velocity	$m\,s^{-1}$
u_t	Final synthetic turbulence	$m\,s^{-1}$
v_t	Convected velocity fluctuations	$m\,s^{-1}$
w_t	Non-dimensional space only velocity fluctuations	$m\,s^{-1}$
x_i	Spatial dimension	m

Superscripts

$\bar{\cdot}$	Averaged component
$\cdot^+$	Non-dimensional version of $\cdot$ (usually by wall coordinates)
$\cdot'$	Fluctuating component
$\hat{\cdot}$	Cholesky decomposition
$\tilde{\cdot}$	Numerically diffused

Subscripts

$\cdot_e$	· associated with the peak of the TKE spectrum
$\cdot_F$	Fluid component
$\cdot_S$	Structure component
$\cdot_\eta$	Kolmogorov ·
$\cdot_{cut}$	· associated with the cut-off of the TKE spectrum
$\cdot_{start}$	· associated with the start of the TKE spectrum
$\cdot_w$	Wall value of ·

Other Symbols

Re	Reynolds number
Re_τ	Reynolds number based on wall shear stress (friction Reynolds number)
Re_θ	Reynolds number based on momentum thickness

This page intentionally left blank.

This page intentionally left blank.

Part I

Introduction

”*The journey of a thousand miles begins with one step*.”
Lao Tzu

1 Introduction

Nuclear energy is a highly efficient source of power due to its high energy density per unit mass and volume [20]. This means that a small amount of nuclear fuel can produce a large amount of usable energy. In addition to being a clean form of electricity generation (in terms of CO_2 emissions), nuclear energy has also made significant progress in terms of technology and applications. However, it is important to properly handle the potentially hazardous chemicals involved in nuclear energy and to prioritize safety, as demonstrated by the Chernobyl [21], Fukushima Daiichi [22], and Three Mile Island [23] incidents. As the demand for energy increases and the earth's average temperatures continue to rise [24], it is necessary to reduce reliance on fossil fuels. While the development of fully sustainable energy solutions is ongoing [25], nuclear energy will likely play a significant role in meeting our immediate power needs [26]. To ensure the safety of nuclear reactors, all aspects must be carefully controlled and the behavior of each system must be thoroughly studied under all potential conditions.

The coolant liquid, such as water or liquid metal, is an important aspect of nuclear safety, as it is responsible for cooling the fuel rods. Fuel rods are submerged in the coolant liquid, which typically flows axially over them to promote efficient cooling. However, this axial flow can also lead to Turbulence Induced Vibrations (TIV) in the fuel rods, which can cause structural damage such as fatigue, wear [27], and stress corrosion cracking. It is therefore crucial to consider the effects of TIV on fuel rod integrity in order to ensure nuclear safety.

The study of Turbulence Induced Vibrations in fuel rods has been a topic of interest since the development of nuclear reactors in the 1950s. It has been a cause of numerous incidents [28] and has thus been the focus of numerous experiments and semi-empirical analyses. These analyses have attempted to establish a relationship between the amplitude of vibration and various parameters such as flow velocity and fluid density, as well as structural parameters such as the diameter of the fuel rod, natural frequency, and damping ratio [29–31]. However, the results of these studies have shown significant discrepancies between theory and experiment, with semi-empirical relations demonstrating an accuracy of only one order of magnitude at best. Additionally, these studies have often only examined a single fuel rod, leading to uncertainty in the extrapolation of these semi-empirical methods to situations involving multiple fuel rods in a bundle.

In recent years, the use of Fluid-Structure Interaction (FSI) simulations for studying fuel rods has gained attention with the increasing availability of computational resources. While more accurate methods like Large Eddy Simulation (LES) and Direct Numerical Simulation (DNS) are still too computationally expensive for full integration into an FSI simulation, Unsteady Reynolds-Averaged Navier-Stokes (URANS) simulations have been explored for complex FSI simulations of TIV on fuel rods. URANS based FSI simulations show good correlation with validation data in terms of frequency and damping ratio, but they show an underprediction of the amplitudes of the displacement [32, 33].

To address the challenges of accurately predicting TIV, Kottapalli et al. [17] proposed a Pressure Fluctuation Model (PFM), which was integrated in the fluid side of NRG's existing framework for FSI simulations. The PFM simulates pressure fluctuations based on URANS data, which are then applied

to the fuel rod as an external excitation for the Computational Structural Mechanics (CSM) solver. The FSI simulations using PFM showed promising results with amplitudes of displacement of the same order of magnitude as experimental data, but still lacked the desired level of accuracy.

To improve the prediction of pressure fluctuations, van den Bos et al. [34] improved PFM and calling their new version called AniPFM (Anisotropic Pressure Fluctuation Model). AniPFM allows for the reconstruction of anisotropic Reynolds stresses, represents only the resolved scales of velocity fluctuations, and incorporates time correlation methods based on turbulence transport, among other improvements. It was validated with two fluid cases and one FSI case. On the fluid side, AniPFM showed a better representation of the energy near the wall, compared to its previous version. In terms of the FSI validation, AniPFM shows much better results than before. While the results are promising, AniPFM needs to be researched more to reduce its uncertainty, understand its dependency on certain parameters and further improve it.

The current study aims at better understanding and further validating AniPFM as well as compare it with other current methods for predicting TIV in fuel rods in terms of accuracy and computational cost. This research hopes to enhance the understanding and modeling of TIV in nuclear reactor fuel rods to ensure their safe operation.

1.1. Report structure

This report outlines the background and results of the work completed for this graduation project. The report is organized into four parts, each corresponding to a different stage of the project:

Part I serves as the introduction to the work detailed in this report and includes an explanation of the report's structure. Chapter 2 outlines the research questions and objective, which were formulated based on the literature study.

Part II covers the essential background information on subjects that are subsequently explored in this project. Chapter 3 gives the reader a basic understanding of how a nuclear power plant works and introduces the problems associated with flow induced vibrations in the reactors. This chapter aims at showcasing the origin of the problem that the numerical approach taken in this thesis is trying to simulate. Chapter 4 analyses the different approaches taken to study flow induced vibrations in nuclear reactor settings: analytical, experimental and numerical. Since, the numerical approach is the one of most relevance to this thesis, the following chapters cover the basis needed to understand how to tackle the problem numerically. In Chapter 5, the basic principles of fluid-structure interaction are laid out. These entail discussions on reference frames, governing equations, possible boundary conditions at the interface of both domains and coupling algorithms. The framework used by NRG in this context is also presented. Chapter 6 features an overview of turbulence modelling, which is crucial for setting a strong foundation for the understanding of Chapter 7 where the topic of synthetic turbulence is introduced and AniPFM is described to detail.

Part III discusses both the methodology carried out during the thesis as well as the results obtained. It is compromised of four chapters, each one concerning a different validation case. The first two cases are pure flow cases, whereas the latter two are FSI. In Chapter 8, the turbulent channel flow is analysed. Chapter 9 steps up the complexity of the previous case by adding curvature in the form of the annular channel flow. In Chapter 10, the first FSI case is presented, the brass beam in turbulent axial flow. This is essentially annular flow, but now the beam is considered elastic. The results from AniPFM are compared with other numerical approaches. Lastly, Chapter 11 covers the FSI case of a cantilever rod in turbulent axial flow. In this case the beam is clamped on one end and free on the other unlike the brass beam where it is clamped on both sides.

Part IV outlines the conclusions and suggestions derived from the project's outcomes. Chapter 12 offers a comprehensive summary of the findings and insights garnered through the analysis of the research taken. In Chapter 13, guided by the results and learnings from the current work, advice and potential directions for forthcoming studies are proposed.

2 Research outlook

Building on the overview provided in the last chapter, this chapter outlines the research outlook for the problem at hand. Based on a detailed review of the current literature, specific research questions have been formulated to help steer this study in a focused direction. This is followed by the establishment of a clear and concise research objective, which aims to maintain a structured and goal-oriented approach throughout the research process.

2.1. Research questions

Following the literature study performed in the aim of this thesis, it was possible to formulate research questions which are expected to be answered throughout the project.

- *What are the optimal parameters of the AniPFM that maximize accuracy and reduce computational cost and uncertainty?*
- *What is the influence/sensitivity of the AniPFM input Reynolds stresses in the RMS of the generated velocity and pressure fluctuations fields?*
- *What is the accuracy and computational cost of NRG-FSIFOAM with AniPFM in simulating TIV in fuel rods when compared to other state of the art methods?*

2.2. Research objective

Research questions aid in defining the scope of the study, serving as tools to formulate hypotheses or pinpoint gaps in the current body of knowledge. Conversely, research objectives are established to outline clear and attainable goals, guiding the direction of the research process. The main research objective of this thesis can be written as such:

> *To delve into a comprehensive exploration of AniPFM to fully grasp its sensitivity to various user-defined parameters. This endeavor aims not only to enhance understanding but also to pinpoint the optimal set of parameters that can potentially reduce uncertainty and increase accuracy in simulating near wall pressure fluctuations*.

In order to tackle a research objective, an approach should be defined, giving a clear reasoning for pursuing given approach. In the case of this thesis, in order to achieve the goals mentioned, four cases are used to study AniPFM: two fluid only cases, and two FSI cases. The first fluid case is the turbulent channel flow. This case is chosen for the availability of high fidelity data and for being a standard in studying wall bounded turbulence. The second case chosen is the turbulent annular flow. This case increases the complexity of the flow by introducing the effect of curvature, while also being closer to the flow over a fuel rod. Regarding the FSI cases, the two cases are: turbulent axial water flow in an annular domain, where the flexible beam is clamped on both ends; and turbulent axial flow over a cantilever rod, which is clamped on one side and free on the other. The former is chosen due to the

availability of other numerical replications of the original experiment, as well as the simplicity of the setup. The latter is chosen for the extensive data from the experiments performed as well as some numerical replication of this setup.

Part II

Theoretical Background

”*The only thing that you absolutely have to know, is the location of the library*.”

Albert Einstein

3 Nuclear reactors

This report is focused on fluid-structure interaction problems in nuclear reactors. A nuclear reactor is the part of a nuclear power plant where nuclear fission reactions take place to generate heat. This heat is subsequently captured and utilized to produce electricity: in the case of a Pressurized Water Reactor (PWR), it heats a coolant which circulates around the reactor core, and this coolant is then used to generate steam to drive turbines. The primary focus of our examination of fluid-structure interactions is the reactor vessel, which houses both the core and the coolant. This chapter delineates the individual components and architecture of a nuclear reactor, as well as the various classifications of flow-induced vibrations present in such environments.

3.1. Components and Architecture

Nuclear reactors can be classified according to their generation and the type of coolant used. The first generation of reactors, developed in the 1950s and 60s, included prototypes and early industrial reactors intended to demonstrate their profitability. The second generation, started in the early 1970s, aimed to be more competitive during the oil crisis. Third generation reactors, which currently constitute the majority of those in use or under construction, prioritize safety and security in response to major accidents like Chernobyl and Three Mile Island. Fourth generation reactors, which are currently in the research phase, aim to increase power density, improve efficiency, and enhance sustainability. Another possible way to classify reactors is in terms of the coolant used: common types of reactors include PWRs, Boiling Water Reactors (BWRs), Gas Cooled Reactors (GCRs), Fast Breeder Reactors (FBRs), and Pressurized Heavy Water Reactors (PHWRs). The most commonly used is the PWR. Figure 3.1 shows a sketch of this type of reactor.

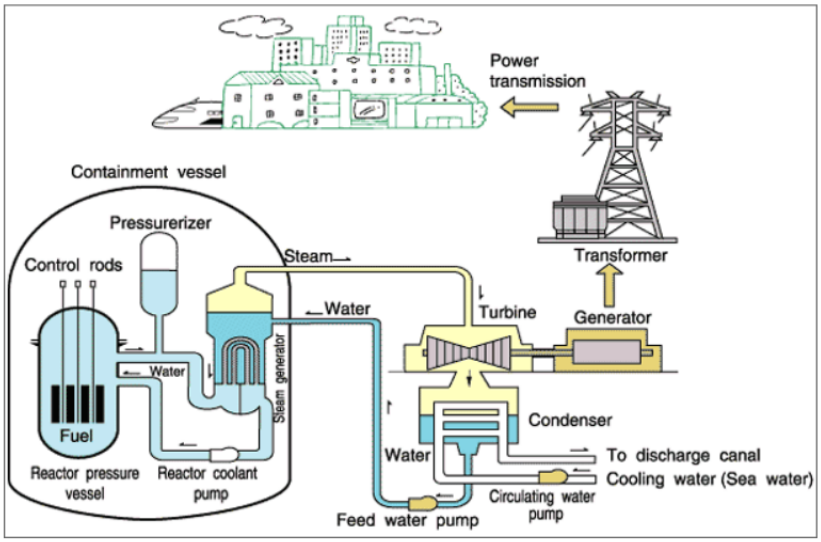

Figure 3.1: Sketch of a Pressurized Water Reactor (PWR) [1].

The fuel rods can be seen in the reactor pressure vessel in Figure 3.1. Figure 3.2 shows a cross section of the reactor vessel of a PWR. In a PWR, the primary coolant loop transports heat away from the fuel rods via high-pressure, high-temperature water. This heat is subsequently transferred to a secondary loop via a steam generator, where the water within the secondary loop is converted into saturated and superheated steam through the absorption of heat from the primary loop. This steam is then utilized to generate electricity through a turbine.

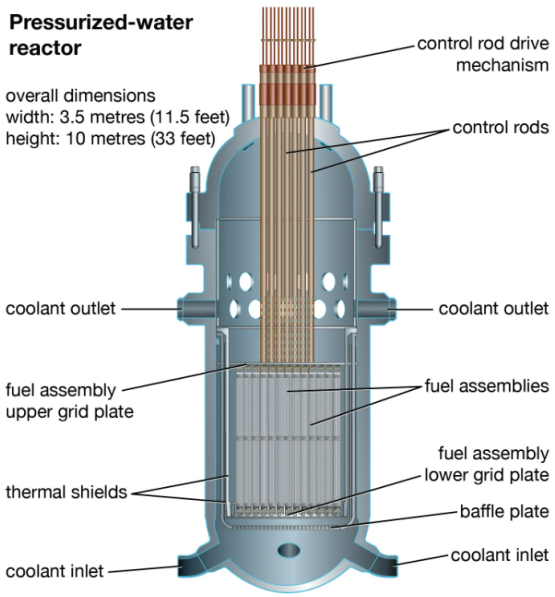

Figure 3.2: Sketch of the fuel rods in the reactor pressure vessel [2].

The focus of this thesis and literature review is the reactor pressure vessel, which houses the fuel rods and is subject to fluid-structure interaction phenomena that can lead to vibrations. Other sources of excitation within the steam generator should also exist. Nuclear power plants can exhibit different types of flow. In steam generators, two-phase flow is often present, while the flow within the reactor pressure vessel can be either single-phase, as in PWRs, or two-phase, as in boiling water reactors BWRs. For the purposes of this thesis, only single-phase flow in the reactor pressure vessel or simplified versions

thereof, such as the fuel rods, will be considered. Specifically, only axial flow will be taken into account in order to narrow the scope of the study.

3.2. Flow induced vibrations

As previously mentioned, the coolant in the reactor pressure vessel can cause vibrations in the fuel rods. These vibrations can have multiple contributing factors, and have been classified in order to facilitate individual study and a better understanding of the underlying physical phenomena. Pettigrew et al. [35] described and classified the different excitation mechanisms:

- **Fluid elastic instability**: fluidelastic instabilities occur when the dynamic forces induced by fluid flow couple with the motion of structures, leading to instability when the flow velocity is high enough for the absorbed energy from fluid forces to surpass the dissipated energy through damping. This type of instability often results in excessive vibration amplitudes and is characterized by a critical velocity below which instability does not occur. While fluidelastic instability is generally not a concern for nuclear components in axial flow due to the high flexural rigidity of these components, it is a significant excitation mechanism for tube bundles in cross flow and can occur in liquid, gas, and two-phase flows.
- **Vortex induced vibrations**: periodic wake shedding, which generates periodic fluid forces, can occur downstream of structures subjected to cross flow. In case the frequency of the shedding and the structure are similar, this can potentially lead to large vibration amplitudes if the vibration response is sufficient to influence the mechanism of wake shedding. This phenomenon, called Karman vortex shedding in the case of an isolated cylinder in cross flow, can also occur in closely packed bundles of cylinders, although the specifics of this phenomenon are not fully understood. Excessive vibration amplitudes due to vortex shedding resonance are more likely to occur in liquid cross flows, where the periodic forces are relatively strong due to the high density of liquids, compared to gas cross flows, where such amplitudes are rare except in the case of high density gases.
- **Turbulence induced vibrations**: vibration excitation may be induced by turbulence, these can be caused by flow fluctuations around the structure of interest (near-field excitation), or by upstream components such as inlet nozzles and elbows (far-field excitation). Turbulence-induced excitation generates seemingly random pressure fluctuations on the surface of the component, leading to vibrations. This is the primary excitation mechanism in axial flow and is also important in cross flow, where it may cause long-term fretting wear damage through sustained vibration response, in addition to the potentially catastrophic failure caused by fluidelastic instability and periodic wake shedding. Turbulence-induced excitation should be considered in both liquid and two-phase cross flow.
- **Acoustic resonance**: acoustic resonance may occur in tube bundles when the frequency of wake shedding coincides with the natural frequency of the acoustic cavity formed by the surrounding structures. This correlation between shedding and resonance can result in intense acoustic noise, which can cause structural damage. Acoustic resonance can also occur in axial flow, such as in the main steam lines of nuclear power plants. Fluctuations in sound pressure, often stemming from sources like pumps or noise from pipe components like valves, can lead to an acoustic resonance in specific segments of the piping network. If the resonance frequency aligns closely with the structure's inherent frequency, it can result in pronounced vibrations.

All of the aforementioned excitation mechanisms are active areas of research within nuclear engineering. However, the focus of this literature study and thesis is to improve the pressure fluctuation model used to model turbulence-induced vibrations. Therefore, only this particular excitation mechanism (TIV) will be considered in this study and subsequent thesis. Specifically, the analysis will be limited to nuclear fuel rods, similar elements, or simplified versions thereof, subjected to single-phase axial flow.

Furthermore, Weaver et al. [28] provided an alternative classification of fluid-structure interaction excitation mechanisms based on their method of production. The categories are as follows below. This classification is being mentioned in this report due to appearing in some relevant papers for TIV.

- **Extraneously Induced Excitation (EIE)**: this kind of FIV arises from fluctuations in the fluid that are not influenced by the movement of the structure.
- **Instability Induced Excitation (IIE)**: sometimes, FIV originates due to flow instabilities that are inherently tied to the flow field shaped by the structure itself. Vortex-induced vibrations are a great example. There are mechanisms that might even further amplify the excitation, like fluid resonance or fluid-elastic feedback. A common example is the ”lock-in” effect, where the frequency of vortex shedding aligns with the structure’s natural frequency, which leads to resonance of the structure. Such an effect can manifest even at different frequencies, especially in the context of rotating structures.
- **Movement Induced Excitation (MIE)**: FIV might also be triggered by variable forces originated from the motions of the oscillating structure. Such vibrations are typically termed ”self-excited”.

In terms of this classification, EIE (turbulent buffeting) is of the most interest. However, for some experiments such as Cioncolini et al. [18] it will be seen that MIE are also relevant.

4

FIV in fuel rods

This chapter offers a review on the existing literature concerning the study of fuel rod vibrations induced by axial flow. The content is organized by the different approaches use to study this complex field: analytical, experimental and numerical.

4.1. Analytical approaches

Païdoussis [36] pioneered the investigation of the linear equation of motion governing slender flexible cylinders in confined axial flow, considering various boundary conditions such as clamped-clamped and clamped-free configurations. Subsequently, numerous researchers, including Rinaldi [37], Ricciardi et al. [38], Chen [39], Basile [29], and Pettigrew [35], expanded upon Païdoussis' theory, refining the expression for fluid forces acting on the slender body.

The equations that are used in the analytical models will be derived and explained. From Equation 4.1 and Equation 4.2, Euler-Bernoulli static beam theory is derived, which relates the deflection of the beam, $y(x)$, and the applied load, q, as it can be seen in Equation 4.3. M represents the bending moment, E stands for the elastic modulus, and I is the second moment of area of the cross section of the beam, which remains constant along its length. When the load, q, is removed, the inertia of the beam will cause it to vibrate around the initial position.

$$M = EI\frac{d^2y}{dx^2} \tag{4.1}$$

$$q = \frac{d^2M}{dx^2} \tag{4.2}$$

$$q = \frac{d^2}{dx^2}\left(EI\frac{d^2y}{dx^2}\right) \tag{4.3}$$

The load is then given by the inertial force on the beam, which is shown in Equation 4.4.

$$q = -m_{rod}\frac{d^2y}{dt^2} \tag{4.4}$$

From Equation 4.3 and Equation 4.4, a differential equation that governs the motion of the free vibration of a slender beam with a uniform cross-section is derived, as shown in Equation 4.5. Here, $y = y(x,t)$ represents the deflection at a certain time, t, and location, x. The equation combines the effects of bending stiffness (represented by the first term) and the inertial properties (represented by the second term) of the beam.

$$EI\frac{d^4y}{dx^4} + m_{rod}\frac{d^2y}{dt^2} = 0 \tag{4.5}$$

The solution to this ODE will provide the natural frequencies, $f_N = \omega_N/2\pi$, and corresponding mode shapes, $\tilde{y}_N(x)$, of the vibrating beam. These natural frequencies and mode shapes represent the unique oscillation patterns that the beam can undergo without external excitation. The general solution is shown in Equation 4.6, where the coefficients a are given by Equation 4.7.

$$y(x) = C_1 e^{ax} + C_2 e^{-ax} + C_3 \sin ax + C_4 \cos ax \tag{4.6}$$

$$a = \sqrt[4]{\frac{m_{rod}\omega_N^2}{EI}} \tag{4.7}$$

For example, in the case of a beam that is free on one end and clamped on the other, it is clear that both the bending moment and shear stress are zero in the free end, which allows us to simplify the equations. This is depicted in Equation 4.8 and Equation 4.9, respectively.

$$M = 0 \Rightarrow \frac{d^2y}{dx^2} = 0 \tag{4.8}$$

$$S = EI\frac{d^3y}{dx^3} = 0 \Rightarrow \frac{d^3y}{dx^3} = 0 \tag{4.9}$$

From the boundary conditions above, the approximate solutions that satisfy such conditions are presented in Equation 4.10 and Equation 4.11, where c_N is the natural frequency parameter. The modes shapes and frequencies for the cantilevered beam can be seen in Figure 4.1.

$$\widetilde{y_N}\left(\frac{x}{L}\right) = y_0\left(1 - \cos\left(\frac{\pi x}{2L}\right)\right) \tag{4.10}$$

$$f_N = \frac{c_N^2}{2\pi L^2}\sqrt{\frac{EI}{m_{rod}}} \tag{4.11}$$

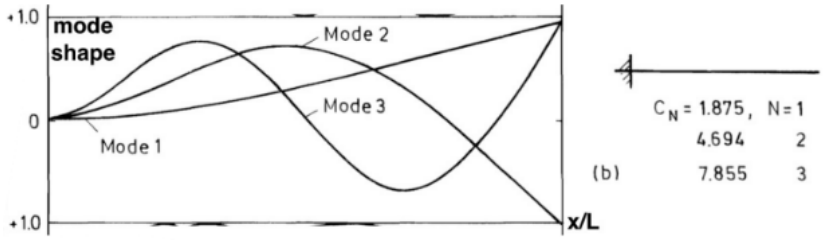

Figure 4.1: Modes shapes and natural frequencies of the first three modes of a straight slender clamped-free beam [3].

In the case of the vibrating beam, the fluid forces are divided into a mean and a fluctuating component, $F = \overline{F} + F'$. The mean component represents the mean hydrodynamic force, whereas the fluctuating component results from the fluid fluctuations, which in the case a fuel rod submerged in fluid flow arise from near wall turbulence. The equation of motion that describes the forced vibration of a uniform slender beam is shown in Equation 4.12, where F^d represents the damping forces, and F^e represents the exciting forces per unit length acting normal to the beam axis. The challenge lies in obtaining an accurate expression for the excitation force of the fluid on the beam.

$$EI\frac{d^4y}{dx^4} + m_{rod}\frac{d^2y}{dt^2} = F = F^d + F^e \tag{4.12}$$

Païdoussis [40] further developed his analytical models, but for conciseness of this report the discussion of his research will not be expanded upon as the introduction has been given. While his model is able to obtain a good expression for $\overline{F}$, it fails to obtain an expression for F' (as other analytical models that are based on equations of motion). Consequently, the model does not account for fluctuations in the pressure field, and thus is not able to predict turbulent buffeting.

To enhance the model's capabilities, Chen [39] extended it to accommodate viscoelastic materials, considering material viscosity and its viscous damping effect. The extension incorporates coefficients for the vibration of the cylinder in a case of a single concentric annulus as well as multiple cylinders.

Basile [29] devised a different approach, whereby based on experimental data, an expression for the dimensionless amplitude of vibration was obtained as a function of non-dimensional flow parameters. Furthermore, Wambsganns [31] used a similar approach to Basile but instead of obtaining the exponents for the non-dimensional flow parameters that are part of the equation by curve fitting the experimental data, they obtained them based on random vibration theory. Païdoussis [30], who also did some work using this approach (with curve-fitting to experimental data), concluded that the maximum order accuracy of these methods is roughly one order of magnitude. These methods are based on the measurement of turbulence statistics upstream of the model being studied, which means that the accuracy is highly dependent on whether the model it is being applied to was part of the curve fitting data or not.

4.2. Experiments

FIV prediction often relies on experimental approaches. There are several studies investigating the influence of tapered shapes on cantilever beams subjected to axial flow [4, 18, 41–44]. The effect of far-field disturbances has also been considered [29, 45]. Non-invasive velocity measurement methods, particularly Particle Image Velocimetry (PIV), accompanied by simultaneous displacement or pressure measurements, have been widely used in current literature to predict FIV frequencies [18, 46, 47].

An early study by Païdoussis examined the influence of cantilever end shape on cylinder dynamics [4, 42]. Further detailed experiments were conducted with flexible cylinders placed horizontally (depicted in Figure 4.2) and vertically, demonstrating that streamlined-end shapes stabilize the structures at significantly lower velocities than blunt-end shapes. The lift force dominated an ideally streamlined end, whereas for a blunt-end, the lift force was compensated by the viscous force in the longitudinal direction. Rinaldi and Païdoussis [44] also investigated the influence of end shape and found that variant end shapes did not significantly affect the cantilever's dynamic response. Similarly, Divaret et al. [41] studied fluid forces on a yawed cylinder and observed that normal forces varied linearly with the angle of inclination, primarily dominated by the lift component.

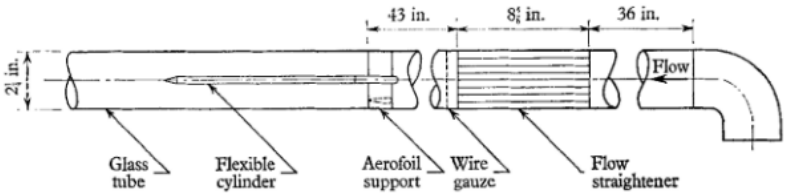

Figure 4.2: Schematic view of the experimental apparatus of the experiment conducted by Païdoussis in 1966 [4].

Experiments in 2018 by Cioncolini et al. [18] tested two opposite beam end shapes, blunt-end, and curved end, revealing that below a certain critical velocity, beam end shape had no influence on cantilever dynamics. However, above the critical velocity, the movement of the rod perturbed the flow field, leading to increased vibration amplitudes. Far-field flow noise, especially from pumps, was found to contribute to increased vibration amplitudes as well, and system parameters such as flow asymmetry and clearance played a significant role in vibration amplitudes. The test rig setup for these experiments was tailored to study FIV in nuclear fuel rods under water-cooled reactor flow conditions, providing valuable data for benchmarking CFD and FSI models. This setup will be analyzed with more detail later on the report, as it is considered to be one of the most promising cases for validation of AniPFM and the whole NRG in-house FSI framework.

Higuchi et al. [47] studied the flow separation at the leading edge of a blunt cylinder and found large-scale vortices impinging on the rod, resulting in low-frequency oscillations. Furthermore, Camussi et al. [48] highlighted that pressure fluctuations near the wall were higher in forward-facing step geometry than in backward-facing steps.

Overall, these experimental studies have significantly contributed to understanding FIV of fuel rods and the influence of various factors on the dynamic behavior of structures under axial flow conditions. The results have practical implications for design and safety considerations in nuclear reactors.

4.3. Numerical approaches

In Chapter 1, a small introduction was given in the use of FSI simulations to address the challenge of studying FIV in fuel rods. This introduction was mainly given to mention AniPFM, which motivates this literature study. In this subsection, a broader overview will be given on the various numerical models developed to study flow-induced vibrations in nuclear fuel rods. Focus will be given to other approaches other than PFM or AniPFM.

Liu et al. [49, 50] utilized a simplified approach in which the fluid forces on a fuel rod were calculated using LES and the fuel rod was approximated using a one-dimensional beam model. Another approach involves simulating the fluid using LES while treating the rod as fixed, and then applying the resulting fluid forces to the rod in a subsequent CSM code [51–53].

DeRidder et al. [32] determined the modal characteristics of a flexible cylinder in turbulent axial flow from URANS simulations, which was later confirmed and extended from one rod to a bundle of fuel rods [33]. Although URANS simulations allowed to determine the eigenmodes of the rods for TIV, the amplitude of the vibrations were underpredicted. However, recently, URANS simulations with Reynolds Stress Models (RSM) showed good results when compared to experimental data of a steel cantilever rod in turbulent water axial flow, both for the amplitudes and frequency [19]. This will be analyzed later in the report.

A comprehensive study by Christon [51] evaluated three turbulence models: LES, Detached Eddy Simulation (DES), and URANS, with mesh refinement. The LES model provided adequate force fluctuations and was applied on the fluid side with rigid structures. The computed flow-induced forces were transferred to vibration analysis software for nuclear fuel rods. The study provided valuable insights into LES flow simulation for fuel assembly design and was validated against PIV experimental results.

The paragraphs above contain a brief summary of the most impactful state of the art numerical approaches to simulating FIV in fuel rods. While numerical simulations open doors for faster, more reliable and safer ways of studying physical phenomena, they also need to be properly validated. In this paragraph, focus will be given to the recent application of Uncertainty Quantification (UQ) to the study of FIV in fuel rods. Numerical research mostly focuses on idealized geometries, while real fuel assemblies deform due to various factors [35, 54]. Recent work acknowledges that in order to achieve more realistic FIV predictions, further developments are needed, for example, considering uncertainties associated with fuel assembly deformations [55]. Besides this, UQ methods play a crucial role in improving simulation confidence. Experimental setups involve inherent uncertainties, complicating numerical validation. By accounting for these uncertainties and propagating them through the model, it becomes possible to predict the expected deviation when comparing with experimental results. This approach enhances simulation accuracy, considering both experimental and numerical uncertainties. Liu et al. [56] established tolerance limits for experimental results of a natural convection lead-bismuth eutectic test-loop using UQ methods. They quantified uncertainties in the simulation results, providing reliable tolerance limits for experimental data. Dolfen et al. [55] investigated the impact of random bow deformation on tube vibration using the Polynomial Chaos method, predicting the stochastic modal behavior of the deformed tube. These studies demonstrate the valuable applications of UQ methods in FIV research, improving the reliability and accuracy of numerical simulations.

5 Fluid-structure interaction

As previously noted in Chapter 1, the literature review for this study focuses on identifying literature that can aid in improving the prediction of vibration amplitudes in nuclear fuel rods experiencing axial flow through FSI simulations. To effectively simulate fluid-structure interaction, a thorough understanding of the basic principles of FSI is necessary to inform the selection and justification of appropriate methodologies. This chapter will discuss the fundamental physics of FSI, reference frameworks, the boundary conditions between fluid and structure, and coupling algorithms. Furthermore, a review of the current NRG framework will be presented, along with the validation of the framework.

5.1. Reference frames

The form of the governing equations for FSI can be affected by the reference frame in which they are expressed. Although the equations remain valid regardless of the reference frame, the chosen frame can significantly impact the complexity of the equations. Therefore, it is crucial to select a reference frame that results in the simplest form of the governing equations, and that makes them easily understandable. This section will present a review of the three most commonly used reference frames in structural dynamics, fluid dynamics, and the interaction between the two, that are deemed most suitable to describe the FSI phenomena.

5.1.1. Lagrangian approach

The Lagrangian reference frame entails a fixed observer's frame of reference that is anchored to the material domain and tracks a designated set of material points within it. This observer's frame moves in correspondence to the displacement and deformation of the selected material particles. In numerical simulations, grid points are established at designated material points, which are generally selected from the initial spatial domain. However, as the spatial domain alters in response to movement and deformation, a mapping function is necessary to correlate the material domain to the spatial domain.

One of the key benefits of the Lagrangian reference frame is its capability of implicit treatment of moving boundaries, as the material points are fixed in the observer's reference frame. Additionally, it does not require accounting for convective terms, as it follows the material particles. However, a limitation of this reference frame is that the mapping function must be well-defined, thus it has a constraint on the maximum deformation that can be mapped.

Given these properties, the Lagrangian reference frame is frequently employed in the field of structural mechanics where deformations are relatively minimal and the mapping function remains well-defined.

5.1.2. Eulerian approach

In the Eulerian reference frame, the observer is fixed at a designated spatial location and uses the spatial domain as its frame of reference. Material properties are calculated at specified points within the domain, regardless of the movement of the material. To measure the variation of a material property over time at a fixed spatial location, it is necessary to take into account both the change in the property at that location and the change due to the convection of the material.

One of the main advantages of the Eulerian frame of reference is that it can handle any deformation as there is no mapping function between the material and the spatial domain. However, special techniques are required to obtain information about boundaries, as there is no boundary description of the material. This framework is commonly utilized in fluid dynamics, where large deformations are often encountered.

5.1.3. Arbitrary Lagrangian-Eulerian approach

The Arbitrary Lagrangian-Eulerian (ALE) reference frame combines aspects of both the Lagrangian and Eulerian reference frames. The observer utilizes a referential domain that moves its frame of reference, but not necessarily at the velocity of the material. Instead, it moves at an arbitrary velocity, resulting in a mesh motion and a material motion in the spatial domain. The velocity of the fluid grid is only determined by the velocity of the structure at the interface of the fluid and the structure.

The geometry is fixed for the observer, but the material can move relative to the referential domain. The material velocity is defined with respect to the referential domain, and the movement of the referential domain with respect to the spatial domain is referred to as the mesh velocity. The main advantage of this method is that the fluid and structural grid do not overlap, as the mesh motion is coupled at the fluid-structure interface. This yields a Lagrangian frame of reference for the structural domain.

The comparison between the different reference frames can be seen in Figure 5.1.

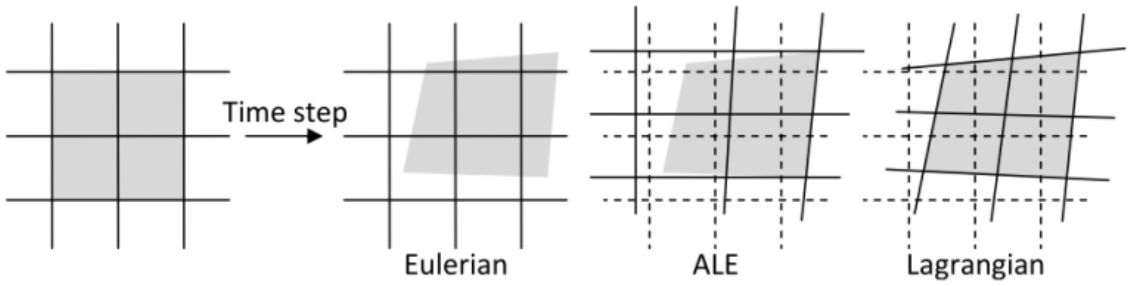

Figure 5.1: The comparison between the Eulerian, arbitrary Lagrangian-Eulerian (ALE) and Lagrangian formulation. The lines represent the grid and the shaded grey areas represent a certain amount of material [5].

5.2. Governing equations

To solve fluid-structure problems numerically, two different approaches can be taken: monolithic and partitioned [57]. The monolithic approach employs a single solver to simultaneously solve both the fluid and structure equations, making it well-suited for fully coupled problems. However, this approach is problem-specific and lacks modularity, making it less viable for situations involving weak or moderately strong coupling.

Alternatively, the partitioned approach employs coupling algorithms to link separate, ”black-box” solvers for the fluid and structure equations. This method involves active data exchange through one-way or two-way mapping, allowing for adaptability to changing boundary conditions. However, the numerical scheme employed in the coupling algorithm can introduce errors into the simulation. Despite this, the partitioned approach is generally considered to be more flexible, making it a viable option in current applications. Thus, it will be the one considered in this chapter. In this section, the governing equations for the fluid and structural dynamics will be analysed as well as the conditions for their interface.

5.2.1. Fluid dynamics

The governing equations of fluid dynamics are the conservation of mass, momentum and energy. In order to close this set of equations, an equation of state is needed. This equation relates the density, pressure and temperature of the fluid. The full equations for the conservation of mass and momentum are presented in Equation 5.1 and Equation 5.2, respectively. These equations are called the Navier-Stokes (NS) equations, and are currently presented in the Eulerian reference frame. In the equations,

ρ is the density, u_i is the velocity in direction i, p is the pressure, τ_{ij} is the viscous stress tensor given by Equation 5.3 and f_i is the sum of the forces in direction i.

$$\frac{\partial \rho}{\partial t} + \frac{\partial \rho u_i}{\partial x_i} = 0 \tag{5.1}$$

$$\frac{\partial \rho u_j}{\partial t} + u_i \frac{\partial \rho u_j}{\partial x_i} = -\frac{\partial p}{\partial x_j} + \frac{\partial \tau_i}{\partial x_i} + \rho f_j \tag{5.2}$$

$$\tau_{ij} = \mu \left(\frac{\partial u_i}{\partial x_j} + \frac{\partial u_j}{\partial x_i} - \frac{2}{3} \frac{\partial u_k}{\partial x_k} \right) \tag{5.3}$$

The Navier-Stokes equations can be further simplified depending on the circumstances. For our application, of cooling liquid in nuclear reactors, the fluid can be considered to be incompressible and of constant density. Thus, the equations can be rewritten as Equation 5.4 and Equation 5.5.

$$\frac{\partial u_i}{\partial x_i} = 0 \tag{5.4}$$

$$\frac{\partial u_j}{\partial t} + \frac{\partial u_i u_j}{\partial x_i} = -\frac{1}{\rho} \frac{\partial p}{\partial x_j} + \frac{1}{\rho} \frac{\partial \tau_{ij}}{\partial x_i} + f_j \tag{5.5}$$

As demonstrated, the conservation of mass for incompressible and constant density flow is simplified to the divergence of the velocity field. This equation, being no longer time-dependent, is commonly referred to as the 'divergence constraint' as it imposes a constraint on the momentum equation for the velocity field. Furthermore, following from this constraint, the last term in the equation Equation 5.3 drops out. The assumption of incompressible flow also results in the decoupling of the energy equation from the momentum equation, rendering the energy equation unnecessary in the solution process.

The equations stated above are presented in the Eulerian reference frame. However, as it was concluded above, the ALE is a better approach for the current application and thus the Navier-Stokes equations for this reference frame are now shown in Equation 5.6 and Equation 5.7. Here, c_i is the convective velocity, which is equal to u_i - $\hat{u}_i$, where u_i is the material velocity with respect to the spatial domain and $\hat{u}_i$ is the mesh velocity with respect to the spatial domain.

$$\frac{\partial c_i}{\partial x_i} = 0 \tag{5.6}$$

$$\frac{\partial u_j}{\partial t} + \frac{\partial c_i u_j}{\partial x_i} = -\frac{1}{\rho} \frac{\partial p}{\partial x_j} + \frac{1}{\rho} \frac{\partial \tau_{ij}}{\partial x_i} + f_j \tag{5.7}$$

As it can be seen above in Equation 5.7, the momentum equation of the Navier-Stokes equations contains a nonlinear differential term, $\frac{\partial c_i u_j}{\partial x_i}$. This nonlinearity present in the NS equations makes them particularly challenging to solve. It is necessary to recur to assumptions in order to solve them for most applications of interest. These assumptions and their consequences will be explained thoroughly in Chapter 6.

5.2.2. Structural dynamics

The Cauchy equation of motion [58] is a fundamental equation in structural dynamics that describes the motion of a mechanical system under the influence of external forces and internal constraints. This equation is derived from the principle of conservation of linear momentum and is commonly used to analyze the dynamics of structures. The equation is given in Equation 5.8, where $\boldsymbol{u}$ is the displacement, σ_S is the stress tensor and $\boldsymbol{g}_s$ is the specific body force on the structure. The equation is written in the Lagrangian formulation, which in the structural domain coincides with the ALE formulation.

$$\rho \frac{\partial^2 \boldsymbol{u}}{\partial t^2} - \nabla \cdot \sigma_s = \rho \boldsymbol{g}_s \tag{5.8}$$

Some assumptions can be made for certain cases to simplify this equation. The linear elastic behaviour assumption states that the stress tensor is related to the strain tensor through Hooke's law [59]. The linear elasticity assumption is valid when the stress-strain behavior of the structure is linear and

the elasticity of the structure is not influenced by the magnitude of the stress. Hooke's law is presented in Equation 5.9 [59], where C_{ijkl} is the stiffness tensor and ϵ_{kl} is the strain tensor.

$$\sigma_{ij} = C_{ijkl}\epsilon_{kl} \tag{5.9}$$

Furthermore, the strain tensor can be approximated by the small displacements assumption, which is related to Equation 5.10. The small displacement assumption is valid when the displacement of each point of the structure is much less than the dimension of the structure.

$$\epsilon \approx \frac{1}{2}\left[\nabla \boldsymbol{u} + (\nabla \boldsymbol{u})^T\right] \tag{5.10}$$

5.2.3. Interface conditions

The interface between the fluid domain Ω_F and the structural domain Ω_S is a critical aspect of the fluid-structure interaction problem, and must be well-defined to obtain a well-posed problem. The fluid exerts a force on the structure, and the movement of the structure in turn affects the flow field in the fluid domain. This information is transmitted through the interface of the two domains, Γ_{FS} , by means of two interface conditions, which are explained below. The interface can be visualized in Figure 5.2.

- **Kinematic Boundary Condition**: this condition arises from the no-slip boundary condition at the interface, and means that the fluid molecules at the interface are "attached" to it and thus have the same velocity as the structure. The kinematic boundary conditions are given by Equation 5.11 and Equation 5.12.

$$\boldsymbol{x}_F = \boldsymbol{u}_S \tag{5.11}$$

$$\boldsymbol{u}_F = \frac{\partial \boldsymbol{u}_S}{\partial t} \tag{5.12}$$

- **Dynamic boundary condition**: this condition stipulates that the traction at the interface between the structure and the fluid must be in equilibrium. This requirement for equilibrium is achieved through a force balancing operation. In other words, the forces exerted on the fluid side of the interface must be equal and opposite to those exerted on the structural side. This ensures that the overall system remains in a state of mechanical equilibrium, which is crucial for the accurate prediction of the behavior of the structure and the fluid. The dynamic boundary condition is shown in Equation 5.13.

$$\sigma_F \cdot \boldsymbol{n}_F = -\sigma_S \cdot \boldsymbol{n}_S \tag{5.13}$$

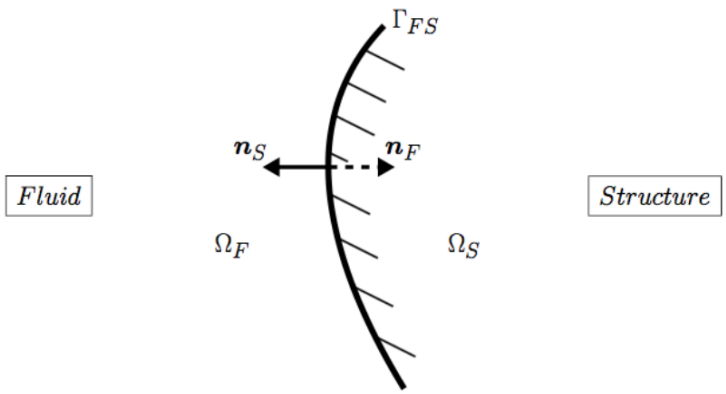

Figure 5.2: Sketch of the interface between a fluid and structure domain [6].

5.3. Coupling algorithms

The governing equations from structural and fluid domains need to be coupled to each other. This allows them to exchange information through their interface, and thus allowing for the solution of a coupled FSI problem. As it was mentioned before, the partitioned approach is preferred over the monolithic. In this approach, both the structural and fluid solvers are seen as black boxes.

There are several ways to couple the two solvers. One way to choose the coupling algorithms is based on the strength of the coupling. Couplings can be distinguished as weak or strong. For weakly coupled problems, explicit algorithms are usually used, whereas for strongly coupled problems, implicit algorithms are used. The difference between both is that explicit algorithms only solve these equations once per time step, whereas implicit algorithms make use of sub-iterations. This difference in approach has important implications for the accuracy and stability of the solution. Specifically, because explicit algorithms only solve the equations once per time step, the equilibrium conditions are not exactly imposed. As a result, the time step size must often be kept small to ensure stability. For the application of this thesis of nuclear fuel rods submerged in liquid coolant, the problem can be considered strongly coupled due to the low densities ratio (ρ_S/ρ_F). Thus, the methods that will be considered are the implicit. Some of the most popular implicit coupling methods are Gauss-Seidel, Jacobi and Newton-Raphson methods.

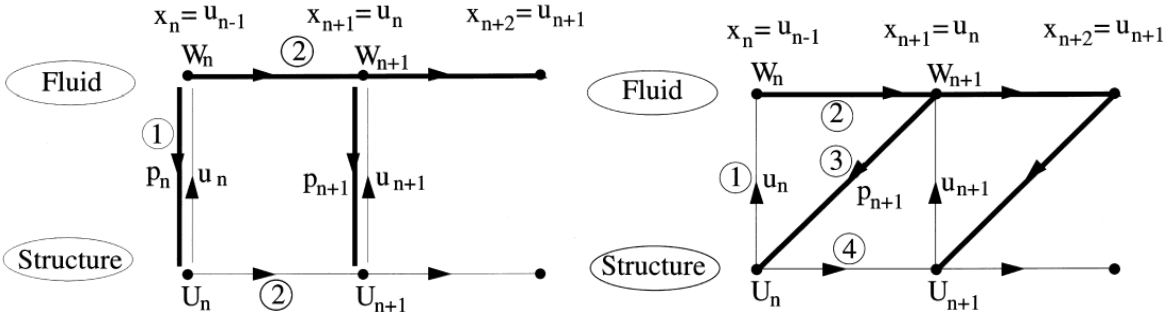

(a) Conventional Parallel Staggered (CPS) **(b)** Conventional Serial Staggered (CSS)

Figure 5.3: Explicit CPS and CSS algorithms which are the basis of Jacobi and Gauss-Seidel implicit coupling algorithms [7].

5.4. NRG application

In the previous sections, the theory and possible algorithms behind FSI simulations were discussed. Now, the framework for FSI simulations at Nuclear Research & consultancy Group will be discussed. This framework has been used for simulating axial flow in fuel rods, but was validated with multiple cases, not only from this domain. This framework was first introduced and validated by Kottapalli et al. [17] with the novel application of a pressure fluctuations model to nuclear applications. Then, De Santis et al. made some adjustments and further validated the framework [33]. They called it the NRG-FSIFOAM framework. Furthermore, van den Bos [34] performed some crucial changes in the PFM model validated the new model. However, the changes that van den Bos et al. performed were not regarding the FSI coupling or algorithms, instead they were purely related to the PFM. Thus, the validation performed by De Santis et al. is still relevant and is the one that will be presented in the following sections (note that the FSI case performed by van den Bos is still useful and will be analyzed later on the report).

5.4.1. NRG-FSIFOAM specifications

This framework uses a partitioned approach. The finite volume Open-FOAM solver [60] is utilized to solve the governing fluid equations using a PIMPLE algorithm, which is a combination of the classical PISO [61] and SIMPLE [62] algorithms. The consistent second order backward difference scheme (BDF2) developed for moving grids is employed for time integration. The fluid mesh is deformed using radial basis function interpolation. For the turbulence cases, URANS is used with $k-\omega$ SST turbulence model. Then, there is also the PFM model, which allows to simulate the pressure fluctuations that

URANS with an eddy viscosity model (EVM), like the $k-\omega$ SST cannot simulate. These fluctuations will act as an excitation mechanism on the structure. The reasoning behind the implementation of this model is to simulate the effect of the pressure fluctuations on the structure without having to use higher fidelity methods such as LES or DNS. The working principles of the PFM model will be explained in Chapter 7.

On the other hand, the governing equations for the solid problem are solved using the finite element approach implemented in the Deal.II library. Linear finite element approximation is used to semi-discretize the governing equations in space, and the θ-method is employed for time integration.

The fluid and solid solvers are coupled through the preCICE library [63] for solving FSI problems, with radial basis functions used to map displacements and forces between the two meshes. A partitioned, parallel implicit coupling solver is used to solve the FSI problem, with quasi-Newton acceleration methods, specifically the IQN-ILS method.

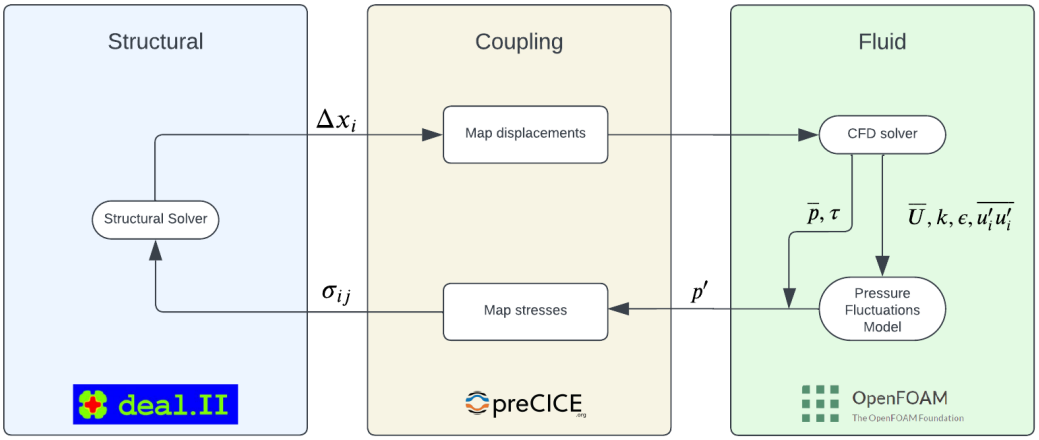

Figure 5.4: Sketch of NRG-FSIFOAM framework with PFM included.

5.4.2. Validation of NRG-FSIFOAM

The NRG-FSIFOAM framework has been extensively tested and validated through a variety of test cases. One of the most well-known benchmarks in the field of fluid-structure interaction, the Turek & Hron case [64], was simulated using the NRG-FSIFOAM framework and the results were compared to those obtained by Turek & Hron in their original study. Another laminar case studied was the experimental freely vibrating rod case [65], which consists of a beam in laminar axial flow.

Additionally, the NRG-FSIFOAM framework was compared to the previously validated FSI framework of STAR-CCM+ in simulating vibrating bare and wire-wrapped rods. The results from both frameworks were found to be similar, further demonstrating the capabilities of the NRG-FSIFOAM framework.

In yet another validation test, the framework was used to replicate an experimental study by Liu et al. [66], in which a cantilever beam was subjected to turbulent axial flow. The simulation results were in good agreement with the experimental data for modal quantities.

5.5. Summary

In this chapter, a review of FSI theory was given as well as the application of these concepts in NRG's framework for simulating turbulence induced vibrations in nuclear applications. First, a big picture look at FSI was given, in the form of reference frames, governing equations for fluid and structural dynamics and interface conditions. Then, coupling algorithms were discussed. Implicit algorithms were deemed as the most fitting for the use case of this thesis, as they perform better than explicit algorithms for strongly coupled problems. NRG's framework, NRG-FSIFOAM, was then presented. This framework makes use of open source tools such as OpenFOAM, deal.II and preCICE, to build a working FSI setup. The use of OpenFOAM allows user development and integration of their own modules, enabling the integration of AniPFM. Moreover, deal.II, through its class based approach to finite element codes, was used to develop a linear finite element method code for the structural dynamics. Since, for turbulence induced vibrations the non-linear effects are not significant, a linear based model was

constructed. Furthermore, preCICE, which includes implicit coupling algorithms with quasi-Newton acceleration, and adapters for OpenFOAM as well as deal.II, serves the function of the 'middle man' in the current framework, providing coupling between the fluid and structural dynamics codes. Moreover, this framework has been extensively validated, mainly with use cases in the domain of turbulence induced vibrations. The technical aspects of the framework alongside its validation repertoire make it suitable for its use during this thesis.

6

Turbulence modelling

In the previous chapter it was seen that in order to simulate turbulence induced vibrations, there was a need to implement a PFM model. In order to fully understand this model and improve it, it is necessary to have an in-depth knowledge of fluid mechanics, in this particular case, of turbulence. Thus, in this chapter, the turbulence characteristics are reviewed, the different methods of solving/modelling turbulence are presented and the governing equation of the pressure fluctuations is derived.

6.1. Turbulence - background

Turbulence is a fascinating and complex phenomenon that has captivated researchers for centuries. As stated by Richard Feynman, "*Turbulence is the most important unsolved problem of classical physics*". The study of turbulence involves understanding the seemingly random and chaotic behavior of fluid flows, and the vast range of scales over which this behavior occurs.

One of the main challenges in understanding and modeling turbulence is the wide range of spatial and temporal scales involved. Turbulent flows are characterized by eddies of varying sizes, from large-scale vortices down to small-scale fluctuations. Understanding the interactions between these eddies and how energy is transferred between them is crucial to developing accurate models of turbulent flows.

Another challenge is the non-linearity of the equations that govern turbulent flows, the Navier-Stokes equations. These equations are highly non-linear and non-local, making it difficult to obtain exact solutions.

6.1.1. Characteristics

Although turbulence is very complex, some of its qualitative features are common among turbulent flows. Tsinober [67], based on Tennekes & Lumley [68], analyzed some of these features:

- *Chaos*: turbulence is a chaotic phenomenon characterized by intrinsic spatio-temporal randomness and irregularity. One of the most important aspects of turbulence is its inherent self-stochastization. Provided that the Reynolds number is high enough there is no need to external random forcing on the flow or its boundaries, or even random initial conditions. Turbulence is extremely sensitive to disturbances (in initial conditions, boundary conditions or external noise). This is because, turbulence acts as a self-amplifier with almost infinite gain, which explains the intrinsic chaos.
- *Wide range of strongly interacting wave numbers*: turbulent flow applications in nuclear have relevant scales that range from meters to millimeters. This interaction between the different length scales happens mostly due to the nonlinearity of the NS equations. Due to the large range of length scales, their interactions, and the above chaotic intrinsic behaviour of turbulent flows, a statistical approach is usually taken to analyze them.
- *Statistical stability*: on a qualitative or even quantitative non-statistical aspect, two turbulent flows nearly identical will show different quantities in everything. However, if a statistical approach is taken, these two flows will show the same statistical properties. This means, that the statistical properties of turbulent flows are insensitive to disturbances, which means statistical stability.

- *Highly dissipative*: turbulent flows are extremely dissipative, which means they carry a lot of strain. Thus, there is a need for a source of energy for turbulence, which happens at low wave numbers. On the other hand, at high wave numbers (small scales) is where dissipation occurs. This concept will be discussed in the following section.
- *3D and rotational*: turbulence shows vortex stretching, which is associates with productions of enstrophy, ω^2, by nonlinear inertial processes. This is characteristic of the large scales and it is not predominant in smaller scales due to viscosity. As a result of vortex stretching, there is production of strain. Both the production of enstrophy and strain are a result of self-amplification of velocity derivatives. For engineering applications, turbulence is always a 3D phenomenon, since for 2D there is no mechanism for vortex stretching. This results in 2D in small scales merging with large scales and forming even larger scales, whereas in reality (3D), the large scales break up into smaller scales.
- *Strongly diffusive*: Turbulent flows show significantly increased transport of momentum, energy and passive objects.

6.1.2. Energy cascade concept

The idea of the energy cascade was introduced by Richardson [69] in 1922. It states that kinetic energy enters turbulence at the large scales through productions. Then, this energy is transferred, through inviscid processes, from the big scales to smaller and smaller scales, until it is dissipated by viscous processes by the smallest scales. Although, Richardson was the first one to introduce the concept of energy cascade, he only analyzed it in macro perspective and was not able to answer some questions such as: what is the length scale of the eddies responsible for dissipation of the energy? What is the relation between the length scale and the characteristic velocity and time scales? Kolmogorov [70] , in the form of three hypothesis, answered those questions and more:

- *Kolmogorov's hypothesis of local isotropy*

  Kolmogorov argued that while the large scales are anisotropic, the direction bias information is lost in the scale-reduction process, where the energy from the large scales is transferred to the smaller scales. Thus, for sufficiently high Reynolds number turbulent flows, the small scales motions are locally isotropic.

- *Kolmogorov's first similarity hypothesis*

  Kolmogorov argued that not only is the direction bias not transferred along the cascade, but actually all information regarding the geometry of the larger eddies is not transferred down the cascade. Thus, the small scale motions can be considered statistically similar in flows with the same Reynolds number. For the small scales, the two important mechanisms are the transfer of energy to successive smaller scales and the viscous dissipation. Thus, two important parameters are the energy transfer rate, which can be approximated by the dissipation rate ϵ and ν.To summarize, for sufficiently high Reynolds number flows, the small scale motions have a universal form that is characterized by ϵ and ν.

- *Kolmogorov's second similarity hypothesis*:

  From the first similarity hypothesis, Komolgorov, using ϵ and ν defined expressions for the length, velocity and time scales, of the smallest scales which are also known as Komolgorov scales. These are shown in Equation 6.1, Equation 6.2 and Equation 6.3.

$$\eta \equiv \left(\nu^3/\varepsilon\right)^{1/4} \tag{6.1}$$

$$u_\eta \equiv (\varepsilon\nu)^{1/4} \tag{6.2}$$

$$\tau_\eta \equiv (\nu/\varepsilon)^{1/2} \tag{6.3}$$

  Furthermore, from the definitions of the Kolmogorov scales and the scaling $\epsilon \sim u_0^3/\ell_0$, the ratios of the smallest to the largest scales were obtained, as it can be seen in Equation 6.4, Equation 6.5

and Equation 6.6. From this relations, it can be seen that for very high Reynolds numbers, the ratio between the small scales and the large gets very low, which means $\eta << l_0$. Kolmogorov concluded that there must be a third range of scales in between the large and small scales.

$$\eta/\ell_0 \sim \mathrm{Re}^{-3/4} \tag{6.4}$$

$$u_\eta/u_0 \sim \mathrm{Re}^{-1/4} \tag{6.5}$$

$$\tau_\eta/\tau_0 \sim \mathrm{Re}^{-1/2} \tag{6.6}$$

The third range mentioned above is the inertial range. It was given this name since inertial forces are predominant in this range and viscous forces are negligible. A sketch of the energy cascade at very high Reynolds numbers is presented in Figure 6.1.

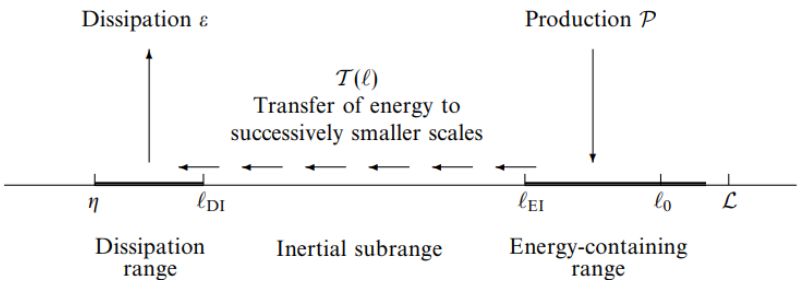

Figure 6.1: Sketch of the energy cascade at very high Reynolds numbers [8].

Energy spectrum

One way of interpreting the energy cascade is through the turbulent kinetic energy spectrum. Turbulent kinetic energy can be defined as Equation 6.7. Or, in wave number terms as Equation 6.8. The wave number κ can be written in function of the length scale of an eddy as $\kappa = 2\pi/l$.

$$k = \frac{1}{2}u_i' u_i' \tag{6.7}$$

$$k = \int_0^\infty E(\kappa)\mathrm{d}\kappa \tag{6.8}$$

From Kolmogorov's first hypothesis it follows that, in the universal equilibrium range (dissipation and inertial range), the spectrum is a function of ϵ and ν. From the second hypothesis, it follows that, in the inertial range, the energy spectrum is given by Equation 6.9, where C is a universal constant.

$$E(\kappa) = C\varepsilon^{2/3}\kappa^{-5/3} \tag{6.9}$$

Homogeneous isotropic turbulence (HIT) is a special case of turbulence. Homogeneity implies that that the turbulence properties are independent of the reference location [8]. Isotropy implies that turbulence properties are invariant to rotations and reflections of the coordinate axes [8]. For HIT, the energy spectrum is represented in Figure 6.2.

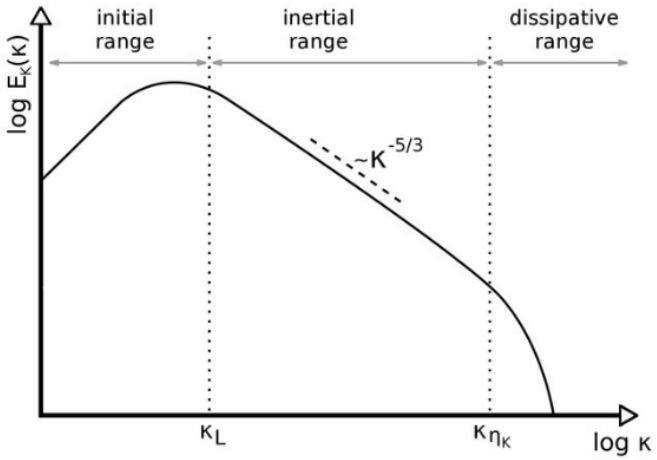

Figure 6.2: Sketch of the energy spectrum for homogeneous isotropic turbulence [9].

6.2. High fidelity methods

High fidelity CFD methods aim to more directly address the physics of turbulence and the Navier-Stokes equations, by not introducing Reynolds-averaged closure approximations. First, direct numerical simulation (DNS) will be discussed, followed by large eddy simulation (LES).

Direct Numerical Simulation

A DNS involves the complete 3D and time dependent solution of the Navier-Stokes equations. Such simulations are a very useful tool for research, as the statistics computed by DNS can be used for example for the testing and calibration of closure approximation models. As it will be seen later, DNS will also provide valuable insights for the improvement of the PFM model. Furthermore, DNS is also very useful to further understand the turbulence structures [71], boundary layer transition and developing turbulence control methods [72], such as drag reduction methods [73]. Additionally, DNS can be used as an unobtrusive 'source of experimental data'.

As it was seen before, turbulent flow has a wide range of scales, from the large scales to the smallest scales, the Kolmogrov scales. In order to perform a true DNS simulation, the mesh would have to be fine enough and the time steps small enough to capture the Komolgorov scales. Due to the computational cost associated with DNS, this tool is usually used only for lower Reynolds number cases [74] [75].

Large Eddy Simulation

For an LES, the large scales are resolved, while the smaller, subgrid-scale (SGS), scales are modelled. The reasoning behind this is that the large scales are the one that are mostly affected by boundary and initial conditions, whereas small scales have more local isotropic and universal characteristics and are less affected by those conditions. Also, the large scales are the ones contributing the most to the Reynolds stresses.

The primary difference between DNS and LES, comes from the use of a filter. The goal of the filter is to filter out the small scales which are meant to be modelled. Many kinds of filters can be used, such as a volume-average box filter or Gaussian filter. The incompressible filtered Navier-Stokes equations are shown in Equation 6.10 and Equation 6.11.

$$\frac{\partial \bar{u}_i}{\partial x_i} = 0 \tag{6.10}$$

$$\frac{\partial \bar{u}_j}{\partial t} + \frac{\partial \bar{u}_i \bar{u}_j}{\partial x_i} + \frac{1}{\rho}\frac{\partial \bar{p}}{\partial x_j} - \nu \frac{\partial^2 \bar{u}_j}{\partial x_k^2} = -\frac{\partial(\overline{u_i u_j} - \bar{u}_i \bar{u}_j)}{\partial x_i} \tag{6.11}$$

The term $(\overline{u_i u_j} - \bar{u}_i \bar{u}_j)$ is the subgrid scale (SGS) tensor. Further decomposition of this tensor results in three stress tensors, one of them can be computed and the other two need modelling [76].

Compared to DNS, with modern computing power LES are already possible to be performed in high Reynolds numbers and somewhat complex geometries [77]. However, in fluid-structure interaction problems, the need for multiple iterations of the fluid solver per coupling step is particularly pronounced, and with implicit schemes, the number of sub-iterations increases as the timestep decreases [5], which further increases computational cost. Thus, for the application of FSI simulations of TIV in fuel rods, LES is still too expensive.

6.3. Reynolds averaged Navier-Stokes

Due to the random fluctuations of turbulence, as said before, a statistical approach is used. Reynolds introduced the so-called Reynolds decomposition in 1895 [78], which separates all quantities into the sum of the mean and the fluctuating component. This is depicted in Equation 6.12.

$$u = \bar{u} + u' \tag{6.12}$$

In terms of averaging, the three most used averaging methods for turbulence research are: *time averaging* for stationary turbulence, *spatial averaging* for homogeneous turbulence and *ensemble averaging*, which is the most general type of Reynolds averaging [79]. The latter is shown in Equation 6.13.

$$\bar{u} = \lim_{N\to\infty} \frac{1}{N} \sum_{N} u \tag{6.13}$$

From the NS equations, one can construct the Reynolds averaged NS equations. These are presented in Equation 6.14 and Equation 6.15. The term $-\rho\overline{u_i' u_j'}$ is called the Reynolds stress tensor, $\rho\tau_{ij}$, so τ_{ij} is formally called the specific Reynolds stress tensor. Aside from the replacement of the instantaneous velocities with the averaged ones, the difference between the original NS equations and the Reynolds averaged ones is the appearance of the Reynolds stress tensor on the right hand side. This tensor is symmetric and thus has six independent components. Hence, with Reynolds averaging, 6 additional unknowns were produced. While there are more unknowns, the number of equations is the same. This means that some additional equations will be needed in order to close the system of equations.

$$\frac{\partial \bar{u}_i}{\partial x_i} = 0 \tag{6.14}$$

$$\frac{\partial \bar{u}_j}{\partial t} + \frac{\partial \bar{u}_i \bar{u}_j}{\partial x_i} = -\frac{1}{\rho}\frac{\partial \bar{p}_j}{\partial x_j} + \frac{1}{\rho}\frac{\partial}{\partial x_i}\left(\bar{t}_{ij} - \rho\overline{u_i' u_j'}\right) \tag{6.15}$$

The most simple turbulence models are the algebraic ones. In order to compute the Reynolds stress tensor, these models use the Boussinesq approximation, which relates the tensor as a product of the eddy viscosity and the mean strain rate tensor, as it can be seen in Equation 6.16. The eddy viscosity, ν_t is often computed in terms of a mixing length, which can be seen as the analogous to the mean free path in a flow. The molecular viscosity is a property of the fluid itself, however the eddy viscosity depends on the flow. This means that also the mixing length depends on the flow. Thus, both the eddy viscosity and mixing length need to be specified in advance. In conclusion, algebraic models are incomplete [79].

$$\tau_{ij} = 2\nu_t \bar{S}_{ij} - \frac{2}{3}k\delta_{ij} \tag{6.16}$$

As the computational power increased, turbulence models based on the turbulent kinetic energy appeared and are now the basis to modern turbulence models. These models are still based on the eddy viscosity and Boussinesq approximation. They can be one or two equation models. The focus of the following section will be on two-equation models.

6.3.1. Eddy viscosity two-equation models

Two-equation turbulence models are based on the equation for k, the turbulent kinetic energy, but also on another equation for the turbulence length scale or equivalent. Due to this, two-equation models are considered to be complete, as they can be used without any previous knowledge of the turbulence

structure of the flow. In this subsection, the two most used two-equation eddy viscosity turbulence models will be introduced, as well as some other models that are derived from them.

The first two-equations turbulence model was proposed by Komolgorov [80]. Kolmogorov chose k as one of the turbulence parameters. This choice is thought to be done because k already appears in the Boussinesq approximation, alongside the eddy viscosity. Furthermore, it is speculated that ω was chosen due to dimensional analysis. Komolgorov set up a transport equation for k and a similar one for ω.

Turbulent kinetic energy transport equation

By taking the trace of the Reynolds stress tensor, it can be seen that there is a relation between it and the turbulent kinetic energy:

$$\tau_{ij} = -\overline{u_i' u_i'} = -2k\,. \tag{6.17}$$

Thus, the equation for k is obtained by taking the trace of the Reynolds stress equation. This results in an equation with very complicated terms such as triple correlations. These terms are modelled, which results in a simplified version of the transport equation for the turbulence kinetic energy, Equation 6.18. The turbulent transport term (triple velocity correlation) was approximated by a gradient-like term and the pressure diffusion was considered to be negligible. The term σ_k is a closure coefficient. The dissipation, ϵ is unknown, and is found by means of another partial differential equation in the case of two-equation models.

$$\frac{\partial k}{\partial t} + \bar{u}_i \frac{\partial k}{\partial x_i} = \tau_{ij} \frac{\partial \bar{u}_j}{\partial x_i} - \varepsilon + \frac{\partial}{\partial x_i}\left[\left(\nu + \frac{\nu_t}{\sigma_k}\right)\frac{\partial k}{\partial x_i}\right] \tag{6.18}$$

$k-\omega$ model

The equation for the specific turbulence dissipation rate, ω, changed a lot after the first postulation by Kolmogorov. All of the developers after Kolmogorov added a production term. Some turbulence researchers used an equation for ω^2 instead of ω. In this section, the focus will be given to Wilcox [79] $k-\omega$ model. Equation 6.19, Equation 6.20 and Equation 6.21 show the equations for the specific turbulence dissipation rate, transport equation for ω and eddy viscosity, respectively, for the $k-\omega$ model. This model shows good results for boundary layer flows, strong adverse pressure gradients and separated flows.

$$\omega = \frac{1}{C_\mu}\frac{\varepsilon}{k} \tag{6.19}$$

$$\frac{\partial \omega}{\partial t} + \rho \bar{u}_i \frac{\partial \omega}{\partial x_i} = -\rho \overline{u_i' u_j'} \alpha \frac{\omega}{k}\frac{\partial \bar{u}_j}{\partial x_i} - \beta \rho \omega k + \frac{\partial}{\partial x_i}\left[(\mu + \sigma \mu_t)\frac{\partial \omega}{\partial x_i}\right] \tag{6.20}$$

$$\mu_t = \rho \frac{k}{\omega} \tag{6.21}$$

$k-\epsilon$ model

This model consists of adding a new transport equation for the dissipation rate, ϵ, in order for the system of equations to be complete. The exact transport for ϵ is far more complicated than the one for k, it involves double and triple correlations of fluctuating velocity, pressure and velocity gradients [79]. These quantities are considered to be unmeasurable and thus, the equation is simplified. Jones & Launder [81] proposed Equation 7.11 for the dissipation rate as well as the closure coefficients. The expression for the eddy viscosity is presented in Equation 6.23. This model shows good results for external aerodynamics, except in the cases of strong curvature, pressure gradients or separation.

$$\frac{\partial \varepsilon}{\partial t} + \rho \bar{u}_i \frac{\partial \varepsilon}{\partial x_i} = -\rho \overline{u_i' u_j'} C_{\varepsilon 1} \frac{\varepsilon}{k}\frac{\partial \bar{u}_j}{\partial x_i} - C_{\varepsilon 2}\rho \frac{\varepsilon^2}{k} + \frac{\partial}{\partial x_i}\left[\left(\mu + \frac{\mu_t}{\sigma_t}\right)\frac{\partial \varepsilon}{\partial x_i}\right] \tag{6.22}$$

$$\mu_t = C_\mu \rho \frac{k^2}{\varepsilon} \tag{6.23}$$

$k-\omega$ SST

In 1992, Menter [82] proposed an improved $k-\omega$ model, called the $k-\omega$ shear stress transport (SST) model. This new model was developed to give similar results to the ones obtained by Wilcox model, but without depending so much on freestream values. Actually, the model is identical to Wilcox model in the first 50% of the boundary layer and then smoothly transitions to the Jones & Launder $k-\epsilon$ model (in a $k-\omega$ formulation) until the edge of the boundary layer. Furthermore, in the cases of boundary layers with adverse pressure gradients, this model accounts for the transport of the principal shear stress.

Non-linear eddy viscosity models

The methods discussed in the sections above are linear eddy viscosity models as they are based on the Boussinesq approximation, which states that the Reynolds stress tensor varies linearly with the mean rate strain tensor. The Boussinesq approximation assumes the eddy viscosity to be a scalar, and this means that it assumes isotropic turbulence. An alternative method for describing the Reynolds-stress tensor without adding extra equations is to assume the Boussinesq approximation is the leading term in a series expansion. With this assumption, various researchers have created constitutive relations that range in complexity. In OpenFOAM there are two non-linear eddy viscosity models: Lien cubic $k-\epsilon$ [83] and Shih quadratic $k-\epsilon$ [84]. The former method extends the Boussinesq approximation to cubic terms, whereas the latter extends it to quadratic terms. Since the methods are extremely similar, only the Shih method will be discussed, as it was the first one to be developed. The equations for k and ϵ are the same ones as for the standard $k-\epsilon$ model. What changes is the constitutive relationship which is presented in Equation 6.24, where C_μ is no longer a constant, as it was in the standard model, but instead it is variable and given by Equation 6.25. Furthermore, C_2 is given by Equation 6.26, S^*_{ij} and Ω^* are defined in Equation 6.27 and Equation 6.28, respectively. The constants needed for the model are described in [84].

$$\overline{u_i u_j} = \frac{2}{3}k\delta_{ij} - C_\mu \frac{k^2}{\varepsilon} 2S^*_{ij} + 2C_2 \frac{k^3}{\varepsilon^2}\left(-S^*_{ik}\Omega^*_{kj} + \Omega^*_{ik}S^*_{kj}\right) \tag{6.24}$$

$$C_\mu = \frac{1}{A_0 + A^*_s \frac{U^* k}{\varepsilon}} \tag{6.25}$$

$$C_2 = \frac{\sqrt{1 - 9C_\mu^2\left(\frac{S^* k}{\varepsilon}\right)^2}}{C_0 + 6\frac{S^* k}{\varepsilon}\frac{\Omega^* k}{\varepsilon}} \tag{6.26}$$

$$S^*_{ij} = S_{ij} - \frac{1}{3}S_{kk}\delta_{ij} \tag{6.27}$$

$$\Omega^*_{ij} = \Omega_{ij} \tag{6.28}$$

One of the problems with linear eddy viscosity models such as the standard $k-\epsilon$ model or RNG variant [85] is the fact they are not realizable. The term ”realizable” means that the turbulence model does not produce unphysical turbulence, which is associated with the mathematical constraints on the Reynolds stresses. These constraints are the non-negativity of the turbulent normal stresses and Schwarz' inequality for shear stresses, $\left(\overline{u_\alpha u_\beta}^2 \leq \overline{u_\alpha^2 u_\beta^2}\right)$. For large mean strain rates, non-realizable turbulence models often produce unphysical results. The turbulence energy in the strain direction will decrease quickly which for non-realizable models often leads to negative normal Reynolds stresses. Furthermore, for high mean shear, the turbulent shear increases quickly and is overpredicted, which results in the violation of Schwarz' inequality. In order to make the $k-\epsilon$ models realizable, the coefficient C_μ cannot be a constant, instead it must change with the mean flow deformation rate. This is exactly what happens with Shih quadratic model and is one of the advantages of this model. The other advantage is the fact that since it is based on a nonlinear equation for the Reynolds stress model, this means that the assumption of isotropic turbulence drops. Lastly, Shih et al. [86] also developed a linear realizable $k-\epsilon$ model.

The quadratic $k-\epsilon$ model improves the representation of the Reynolds stress tensor, however it still assumes a scalar value for eddy viscosity and the closure coefficients. Though eddy viscosity models work well for specific flow types, more precise models that can predict Reynolds stress more accurately are desired. These models will be discussed in the following subsection.

6.3.2. Reynolds stress models

The limitation of the eddy viscosity models discussed above is the reliance on the Boussinesq approximation. There is another family of turbulence models called the Reynolds stress models (RSM) which instead of the Boussinesq approximation, solve a PDE for the Reynolds stress tensor. This equation is

called the stress transport equation and while it increases the accuracy of the turbulence model there is a price to be paid in terms of computational efficiency. The RSM that are implemented in OpenFOAM are the Launder, Reede and Rodi model [87] and the Speziale, Sarkar and Gatski (SSG) model [88], and thus are the ones that will be discussed in this section.

All of the Reynolds stress models start from the same equation, the exact differential transport equation that describes the behaviour of the Reynolds stress tensor, τ_{ij}. This equation is shown in Equation 6.29. On the left hand side is the material derivative of the Reynolds stress tensor, and on the right hand side are the production, dissipation, pressure-strain and diffusion terms. The first term of the diffusion terms is called the turbulent transport term. By analyzing Equation 6.29, it is clear why stress transport models are expected to outperform EVM. The equation accounts for convection and diffusion of τ_{ij}, which means that effects of flow history are included. Furthermore, it accounts for the phenomena involved in streamline curvature, such as convection and production. Lastly, the stresses are not correlated with the mean strain rate, unlike the EVM, and thus their values will depend on the initial conditions and the physics, rather than being affected by sudden changes in mean strain rate [79].

A visually simpler representation of the stress transport equation is given in Equation 6.30 (the material derivative was expanded also).

$$\frac{D\overline{u_i'u_j'}}{Dt} = \overbrace{-\left[\overline{u_j'u_k'}\frac{\partial \overline{u}_i}{\partial x_k} + \overline{u_i'u_k'}\frac{\partial \overline{u}_j}{\partial x_k}\right]}^{\text{Production}} \overbrace{-2v\overline{\frac{\partial u_i'}{\partial x_k}\frac{\partial u_j'}{\partial x_k}}}^{\text{Dissipation}} \overbrace{+\overline{\frac{p'}{\rho}\left(\frac{\partial u_i'}{\partial x_j} + \frac{\partial u_j'}{\partial x_i}\right)}}^{\text{Pressure-strain}} - \underbrace{-\frac{\partial}{\partial x_k}\left[\overline{u_i'u_j'u_k'} - \nu\frac{\partial \overline{u_i'u_j'}}{\partial x_k} + \overline{\frac{p'}{\rho}\left(\delta_{jk}u_i' + \delta_{ik}u_j'\right)}\right]}_{\text{Diffusion}} \tag{6.29}$$

$$\frac{\partial \tau_{ij}}{\partial t} + \overline{u_k}\frac{\partial \tau_{ij}}{\partial x_k} = \underbrace{P_{ij}}_{\text{Production}} + \underbrace{\phi_{ij}}_{\text{Pressure-strain}} - \underbrace{\epsilon_{ij}}_{\text{Dissipation}} + \underbrace{T_{ijk} + D_{ij}^v + D_{ij}^p}_{\text{Diffusion}} \tag{6.30}$$

As it can be seen the production term, P_{ij}, already involves the Reynolds stress and mean velocity gradients, and thus does not need modelling. Same goes for the velocity diffusion term D_{ij}^v. However, the terms ϵ_{ij}, ϕ_{ij}, T_{ij} and D_{ij}^p need modelling as they cannot be computed directly from mean flow quantities.

As it was discussed in section 6.1, dissipation occurs mainly in the smaller scales of turbulence. Because of this, the assumption of local isotropy is usually used. This leads to the dissipation rate tensor being modelled as Equation 6.31, where the scalar quantity ϵ is the dissipation rate appearing in the k equation of two-equation models.

$$\epsilon_{ij} = \frac{2}{3}\epsilon\delta_{ij} \tag{6.31}$$

The turbulent transport term, T_{ij}, was usually modelled assuming a gradient-transport. Daly & Harlow argued that the simplest approximation would be in the form of the derivative of the Reynolds stress tensor,

$$T_{ijk} \approx \frac{\partial \tau_{ij}}{\partial x_k}\,. \tag{6.32}$$

Although simple, this form did not respect the rotationally invariance of T_{ij} (symmetry in all of the three indices) [79]. Later, Launder et al. [87] proposed Equation 6.33, which is used in the LLR RSM.

$$T_{ijk} = \frac{2}{3}C_s\frac{k^2}{\epsilon}\left[\frac{\partial \tau_{jk}}{\partial x_i} + \frac{\partial \tau_{ik}}{\partial x_j} + \frac{\partial \tau_{ij}}{\partial x_k}\right] \tag{6.33}$$

The modelling of the pressure-strain correlation tensor, ϕ_{ij}, is what mainly sets apart the different RSM. The tensor is usually decomposed into a slow and a fast component, as can be seen in Equation 6.34. The slow component models the return to isotropy, whereas the fast one models the immediate effects. The slow component modelling was first proposed by Rotta [89] and is shown in Equation 6.35. The modelling of the fast component is where the RSM mostly differ. First, researchers

assumed this term to be negligible when compared to the slow term [90–92]. However, it was proven that this assumption does not hold true for a variety of flows [93, 94] and thus should be dismissed. The LRR model expresses the fast tensor as a linear function of the Reynolds stress tensor [87], whereas the SSG model also model the quadratic terms [88].

$$\Phi_{ij} = \Phi_{ij}^{S} + \Phi_{ij}^{R} \tag{6.34}$$

$$A_{ij} = C_1 \frac{\epsilon}{k} \left(\tau_{ij} + \frac{2}{3} k \delta_{ij} \right) \tag{6.35}$$

While RSM greatly improve the accuracy of the turbulence modelling when compared to EVM, they are also considerably more computational expensive. An alternative solution would be to use an Explicit Algebraic Reynolds Stress Model (EARSM), which is similar to the nonlinear eddy viscosity models but instead obtains the constitutive relation from the Reynolds stress transport equation. One of the most popular EARSM is the one developed by Wallin & Johansson [95]. However, EARSM have not been implemented in OpenFOAM yet, and therefore their use will be dismissed for this thesis, but might be worth it to consider them in the future if/when implemented.

6.4. Reynolds stress tensor corrections

Linear eddy viscosity models assume that the root-mean-square velocity fluctuations are isotropic, but this assumption is not valid for near-wall flows. To address this, some empirical methods have been developed to reconstruct the Reynolds stress tensor more accurately from URANS data. These methods are only applicable to the diagonal elements of the Reynolds stress tensor, with the cross-terms still estimated using the Boussinesq hypothesis. Laraufi et al. [96] studied the implementation of these empirical methods for generating synthetic turbulence. The two most significant methods were based on Wilcox's hypothesis and Marusic & Kunkel's empirical model [97]. The Wilcox's hypothesis method was built on Wilcox's nonlinear eddy viscosity model [98]. The corrections presented by Wilcox to the Reynolds stress tensor diagonal terms are presented in Equation 6.36. This method was found to be valid for y+ values greater than 100 [96]. The second method, developed by Marusic & Kunkel, considered the effect of Reynolds number, but was only valid for Re_θ greater than 3200 and for zero pressure gradient flows. This method performed better for the inner part of the boundary layer. However, due to its wider applicability and ease of implementation, Wilcox's hypothesis is preferred for computing the diagonal elements of the Reynolds stress tensor. This correction is implemented in AniPFM as will be seen in section 7.3.

$$\overline{u'u'} = \frac{8}{9}k \qquad \overline{v'v'} = \frac{4}{9}k \qquad \overline{w'w'} = \frac{6}{9}k \tag{6.36}$$

6.5. Governing equation of pressure fluctuations

Now that the turbulence modelling has been discussed, which will be part of the URANS section, everything is set up to start talking about the PFM part of the model. In this section, the deduction of the governing equation of the pressure fluctuations will be shown.

First, the decomposition of velocity and pressure in mean and fluctuating component is substituted into the momentum equation of the NS, as it is shown in Equation 6.37.

$$\frac{\partial \left(\bar{u}_j + u'_j \right)}{\partial t} + \frac{\partial \left(\bar{u}_i + u'_i \right) \left(\bar{u}_j + u'_j \right)}{\partial x_i} = -\frac{1}{\rho} \frac{\partial \left(\bar{p} + p' \right)}{\partial x_j} + \frac{1}{\rho} \frac{\partial}{\partial x_i} t_{ij} \tag{6.37}$$

Then, the ensemble average momentum equation (the URANS momentum equation) is subtracted from the instantaneous solution and the divergence operator is taken. The resulting equation is the governing equation of pressure fluctuations, Equation 6.38. This equations shows that the pressure fluctuations are governed by and elliptic PDE, more specifically, the Poisson equation. In this equations, it can be seen that the pressure fluctuations only depend on the velocity mean and fluctuations. The mean component is readily available from URANS data, which means that for the PFM, there is only a need to model the velocity fluctuations in order to get the pressure fluctuations. Furthermore, the right hand side (RHS) of this PDE can be decomposed into a slow and a fast component. The reasoning is

the same as the one taken for the pressure-strain correlation tensor in the RSM. In the Reynolds stress transport equation, Equation 6.29, ϕ_{ij} depends on the pressure and velocity fluctuations. So in order to derive an approximation for this tensor, also the Poisson equation for the pressure fluctuations was derived and separated into two components. The rapid term is the left term on the RHS of Equation 6.38 and the slow term is the one on the right in the RHS of the equation.

$$\frac{\partial^2 p'}{\partial x_i \partial x_i} = -\rho \left[2 \frac{\partial \bar{u}_i}{\partial x_j} \frac{\partial u'_j}{\partial x_i} + \frac{\partial^2}{\partial x_i \partial x_j} \left(u'_i u'_j - \overline{u'_i u'_j} \right) \right] \tag{6.38}$$

6.6. Summary

In this chapter, different aspects of turbulence modelling were discussed. First, a review was given on turbulence, where its different characteristics were considered. Such characteristics are turbulence being chaotic, having a wide range of interacting wave numbers, being statistical stable, highly dissipative and diffusive, 3D and rotational. It is important to understand turbulence characteristics so that they can be modelled correctly with turbulence models, and so that these models do not rely solely on mathematical approximations, but instead consider the physics while not violating the mathematical constraints. Then, the energy cascade concept was presented, alongside Kolmogorov's hypothesis and expressions for the small scales of turbulence, as well as how these relate to the bulk flow quantities. Furthermore, in section 6.2, high fidelity methods such as DNS and LES are discussed. These methods resolve all of the turbulence wave number range scale, in the case of DNS, and a part of it, in the case of LES. Since these methods are too computationally expensive for FSI simulations in nuclear applications, section 6.3 was regarding RANS, a computationally cheaper alternative to the aforementioned methods, but that does not resolve any part of the turbulence spectrum and instead solely models. The Reynolds decomposition was introduced as well as Reynolds averaging. With these two concept in mind the Reynolds averaged NS equations were presented. These equations brought a new term to the mix, the Reynolds stress tensor. This tensor is symmetric, which means that there are 6 additional unknowns brought by the process of Reynolds averaging. In order to close the system, new equations need to be proposed. This is where the eddy viscosity models and Reynolds stress models come in. The EVM are based on a constitutive relation that relates the Reynolds stress tensor with the eddy viscosity, mean strain rate tensor and turbulent kinetic energy. Further, these models use one equation for the turbulent kinetic energy and one for another turbulence quantity. The most popular linear two-equation EVM were discussed, the $k-\omega$ and the $k-\epsilon$. A variation that includes characteristics from both, called $k-\omega$ shear stress transport, was also discussed. Additionally, non-linear eddy viscosity models were then presented. These models are still based on the Boussinesq approximation, which states that the Reynolds stress tensor linearly varies with the mean strain rate tensor. Non-linear eddy viscosity models assume the Boussinesq approximation is simply the leading term of a series expansion and derive a non linear relation between the Reynolds stresses and the mean strain rate tensor. Although these show improved results when compared to linear EVM, they still assume that the eddy viscosity is a scalar and thus assume isotropic turbulence. In order to more accurately model turbulence, Reynolds stress models are needed. These are not based one the Boussinesq approximation, but instead on an approximation of the exact Reynolds stress transport equation. The modelling of this exact equation is discussed as well as two RSM: the LRR and SSG. While these models show better performance than EVMs, they are also more expensive. In AniPFM, only EVMs have been studied to use as input. Van den Bos et al. [34] showed that the $k-\omega$ SST provided the best near wall behaviour among the different linear EVMs available in OpenFOAM and thus was chosen as the most suitable to be used as AniPFM input. This model is also used throughout this thesis. Finally, in section 6.5, the governing equation of the pressure fluctuations is derived from the NS equations. This equation allows better understanding of what fundamentally drives the generation of pressure fluctuations in turbulent flows.

7 Synthetic turbulence

In this chapter, multiple aspects of synthetic turbulence will be discussed. Firstly, taking into account the characteristics of turbulence mentioned in Chapter 6, the requirements of synthetic turbulence (ST) models will be laid out. Secondly, the current active research areas of ST will be described. Furthermore, NRG's model, AniPFM, will be described to detail.

7.1. Requirements

As it was seen in the last chapter, the governing equation for the pressure fluctuation is a Poisson equation. The pressure fluctuations only depend on the mean velocity and velocity fluctuations. Thus, in order to model the pressure fluctuations, the PFM needs to model the velocity fluctuations. There are several characteristics that the synthetic turbulence should have in order to be physical and representative of reality. In this section those characteristics will be discussed.

7.1.1. Adhering to the governing equations

First, the instantaneous solution, i.e. the sum of the ensemble-averaged velocity and velocity fluctuations should follow the Navier-Stokes equations. However, as it was seen before, if the turbulence follows the NS equations, then DNS is required and the turbulence will be resolved and not modelled. Although it is not possible to adhere to the exact NS equations, approximations of these equations can be satisfied. Starting with the continuity equation, decomposing u into mean and fluctuating component, Equation 7.1 is obtained. From Equation 5.1 and Equation 7.1, Equation 7.2 is derived. This means that the velocity fluctuations should also adhere to the divergence constraint.

$$\frac{\partial \left(\bar{u}_i + u_i'\right)}{\partial x_i} = 0 \tag{7.1}$$

$$\frac{\partial u_i'}{\partial x_i} = 0 \tag{7.2}$$

Regarding the conservation of momentum, certain assumptions will need to be made. For the lower wave numbers, the flow can be assumed inviscid as the forces are mainly inertial. Thus, the Euler equations, Equation 7.3 can be used as governing equations.

$$\frac{\partial u_i}{\partial t} + u_k \frac{\partial u_i}{\partial x_k} + \frac{1}{\rho}\frac{\partial p}{\partial x_i} = 0 \tag{7.3}$$

Assuming that the acceleration of flow by pressure gradient is negligible, and substituting u with its Reynolds decomposition, Equation 7.4 is derived.

$$\frac{\partial u_i'}{\partial t} + \bar{u}_k \frac{\partial u_i'}{\partial x_k} + u_k' \frac{\partial u_i'}{\partial x_k} = 0 \tag{7.4}$$

Finally, assuming $\bar{u_i}$ >> u_i', then it can be assumed that the velocity fluctuations are convected at the speed of the mean velocity. What was just described is Taylor's frozen wake hypothesis [99]. It

can be seen that the term $u'_k \frac{\partial u'_i}{\partial x_k} \approx 0$, based on the previous arguments. Thus, the final approximated momentum equation is given by Equation 7.5.

$$\frac{\partial u'_i}{\partial t} + \bar{u}_k \frac{\partial u'_i}{\partial x_k} = 0 \tag{7.5}$$

7.1.2. Modelling of the energy spectrum

As it was seen before, the properties of turbulence vary depending on the length scale. Furthermore, it was also discussed that by representing the turbulent kinetic energy as a continuous energy spectrum of wave numbers (where the wave numbers are inversely proportional to the eddy length scales), the differences in properties can effectively be summarized. This representation allows for an accurate depiction of turbulence, as it ensures that each eddy length scale receives a realistic amount of kinetic energy, which directly influences the magnitude of velocity fluctuations.

Another important property of turbulence is the wide range of scale interactions that occur. While the chaotic nature of turbulence may lead one to believe that it is a disordered and random process, the presence of coherent structures and interactions between them suggests otherwise. These interactions result in spatial correlation within turbulence, which cannot be represented by a white noise field. It is important to note that this spatial correlation is also implicitly modelled through the turbulent kinetic energy spectrum. The energy spectrum tensor of a velocity signal is defined as the Fourier transform of the auto-correlation function of that series [8]. Therefore, by accurately modelling the energy spectrum, the spatial correlation functions are also implicitly and accurately modelled.

In conclusion, to accurately replicate turbulence, it is necessary to consider both the energy distribution and spatial correlation within the phenomenon. A thorough understanding of the properties of turbulence at different length scales, as well as the interactions between those scales, is crucial for an accurate representation.

7.1.3. Reynolds stress tensor

Looking at the PDE governing the pressure fluctuations, it can be seen that the Reynolds stress tensor has an explicit impact on their behaviour, as it is part of the equation. Thus, accurate Reynolds stresses should improve the accuracy of the modelling of the pressure fluctuations. Although it is known that the Reynolds stresses have an effect on the pressure fluctuations [34], regarding the PFM, it is not known yet the sensitivity of the model to the input Reynolds stresses from the URANS. Overall, it was this requirement that led van den Bos [34] to improve Kottapali's PFM [17] to an anisotropic PFM that does not assume isotropy in the Reynolds stress tensor and thus allows for anisotropy. Although van den Bos new model shows better results, multiple changes were made to the whole model, a few validation cases were tested, which makes it impossible to know for sure the sensitivity of the model to the accuracy of the input Reynolds stress tensor.

7.1.4. Temporal decay

As it was seen in section 6.1, turbulent flows are extremely dissipative. This means that they carry a lot of strain, which results in production of energy for turbulence at low wave numbers and dissipation of energy at high wave numbers. The dissipation causes turbulence to decay over time. A clear example of this, is the homogeneous isotropic turbulence box, where there is no production of turbulence, and thus it decays over time [100]. The constant production of turbulence and dissipation creates a decorrelation in time in turbulence. This means that the previous correlation in time caused by convection is not enough to model the conservation of momentum. Hence, the turbulence correlation due to convection and decorrelation due to production and dissipation should be modeled separately.

7.2. Research areas

Synthetic turbulence has been applied to many areas within CFD, such as simulating the wind loads on tall buildings [101], modelling of fatigue loading on wind turbines [102–104], simulating pressure fluctuations on fuel rods subjected to axial flow in FSI simulations [17, 33, 34, 105] among others. However, the most popular ones are generating inflow conditions for LES [106–111], noise modelling [11, 112–114] and for the interface of hybrid RANS/LES models [10, 115–119]. These are the research areas which contribute the most to ST and novel techniques within it.

7.3. NRG model - AniPFM

The method currently employed at NRG for pressure fluctuations is called *AniPFM* (anisotropic PFM) and was developed by van den Bos et al. [34], starting from the model of Kottapali et al [17]. The purpose of this new model is to merge the synthetic turbulence model developed by Billson et al. [11] with the one presented by Shur et al. [10], in order to create a model that incorporates the benefits of both approaches.

7.3.1. Velocity fluctuations

Similarly to Shur et al. [10], there is an auxiliary dimensionless velocity field, $\boldsymbol{v}_t(\boldsymbol{x},t)$, which is related to isotropic fluctuations, and a final velocity fluctuations field, $\boldsymbol{u}_t(\boldsymbol{x},t)$, which is anisotropic. The goal of this method is to introduce the anisotropy of the Reynolds stress tensor into the fluctuations. The relation between these two fields is presented in Equation 7.7, where a_{ij} is part of the Cholesky decomposition of the Reynolds stress tensor, $\widehat{\boldsymbol{R}} = \widehat{\boldsymbol{A}}^T\widehat{\boldsymbol{A}}$, where $\widehat{\boldsymbol{A}}$ is given by Equation 7.6, as in Shur et al. method. Like in this method, this is done so that the final generated velocity fluctuations are defined so that the corresponding covariance is equal to the Reynolds stress tensor. Furthermore, $\boldsymbol{v}_t(\boldsymbol{x},t)$ must obey $\overline{\boldsymbol{v}_t'} = 0$ and $\overline{\boldsymbol{v}_t'\boldsymbol{v}_t'} = \delta_{ij.}$. The non-dimensional isotropic fluctuations $\boldsymbol{v}_t'(\boldsymbol{x},t)$ are computed by applying time correlation methods to non-dimensional spatial only fluctuations, called $\boldsymbol{w}_t'(\boldsymbol{x})$. The latter are calculated by Equation 7.8, similarly to how Shur et al. [10] calculated their non-dimensional fluctuations. Here, q_n is the non-dimensional energy, $\boldsymbol{\sigma}_n$ is the direction vector, $\boldsymbol{k}_n$ is the wave number vector and $\boldsymbol{\phi}_n$ is the phase shift, which is a random number uniformly distributed in the interval [0,2π]. The subscript n denotes that it is relating to the n^{th} Fourier mode.

$$\widehat{\boldsymbol{A}} = \{a_{ij}\} = \begin{pmatrix} \sqrt{R_{11}} & 0 & 0 \\ R_{21}/a_{11} & \sqrt{R_{22}-a_{21}^2} & 0 \\ R_{31}/a_{11} & \left(R_{32}-a_{21}a_{31}\right)/a_{22} & \sqrt{R_{33}-a_{31}^2-a_{32}^2} \end{pmatrix} \tag{7.6}$$

$$\boldsymbol{u}_t(\boldsymbol{x},t) = a_{ij}\boldsymbol{v}_t(\boldsymbol{x},t) \tag{7.7}$$

$$\boldsymbol{w}_t(\boldsymbol{x}) = \sqrt{6}\sum_n \sqrt{q_n}\left[\boldsymbol{\sigma}_n \cos\left(\boldsymbol{k}_n\cdot\boldsymbol{x}+\phi_n\right)\right] \tag{7.8}$$

7.3.2. Turbulent kinetic energy spectrum

The non-dimensional energy, q_n, is defined in the same way as Shur et al. [10], by Equation 7.9. The energy spectrum is the modified von Karman spectrum, as presented in Equation 7.10, where k_e is the wave number corresponding to the TKE peak, k_η is the highest wave number. The wave number k_e can be calculated by Equation 7.11, where l_e can is defined as Equation 7.12, where C_l is a constant equal to 3.0 to match the spectrum of the experimental data of Comte-Bellot & Corrsin [120]. The difference in the definition of l_e in this method when compared to Shur et al. [10] is that van den Bos et al. does not include the term that takes into account the distance to the nearest wall. This term shows to give an underestimation of the pressure fluctuations near the wall due to giving an underestimation of the largest wave number and that is why it was dismissed for the current method. The goal of Shur et al. research was LES inflow and zonal RANS/LES interface and thus it is normal that this effect was not considered. This choice will be discussed further down in this subsection. The highest wave number, also known as the Kolmogorov wave number, is computed by Equation 7.13. To improve the accuracy of the reconstructed energy spectrum, a cut-off filter, f_{cut}, is applied to the modified Von Kármán spectrum. Without the filter, the spectrum extends until the Kolmogorov wavenumber, but this high-wavenumber portion of the spectrum cannot typically be resolved by the mesh, requiring the use of DNS. The cut-off filter helps to prevent an aliasing effect that would result from the unresolved portion of the inputted spectrum, ensuring a more correct distribution in the reconstructed energy spectrum. The cut off filter is calculated in the same way as Shur et al. [10], as presented in Equation 7.14, where $k_{cut} = 2\pi/l_{cut}$ and l_{cut} is the cut off length.

$$q^n = \frac{E\left(k^n\right)\Delta k^n}{\sum_n E\left(k^n\right)\Delta k^n} \tag{7.9}$$

$$E(k) = \frac{(k/k_e)^4}{\left[1 + 2.4\,(k/k_e)^2\right]^{(17/6)}} \exp\left(-\left(12\frac{k}{k_\eta}\right)^2\right) f_{cut} \tag{7.10}$$

$$k_e = 2\pi/l_e \tag{7.11}$$

$$l_e = C_l l_t \tag{7.12}$$

$$k_\eta = 2\pi\left(\frac{\varepsilon}{v^3}\right)^{\frac{1}{4}} \tag{7.13}$$

$$f_{cut} = \exp\left(-\left[\frac{4\max\left(k - 0.9k_{cut}, 0\right)}{k_{cut}}\right]^3\right) \tag{7.14}$$

So far, it has been seen that two different length scales need to be defined in order to model the turbulent kinetic energy spectrum. These length scales are l_e and l_{cut} as explained above.

Starting with the choice of l_e, above it was mentioned that van den Bos et al. optioned for a different way of computing this length scale when compared to Shur et al. While the latter consider the wall distance in the formulation of the length scale (l_e = min[2d_W, $C_l l_t$]), the former does not. In Figure 7.1 is presented the difference between the wall distance and the URANS length scale for a turbulent channel flow at Re_τ = 640. It can be seen that the wall distance is always smaller than 3l_t and thus Shur et al. approach of calculating the length scale will result in twice the wall distance. If l_e is underpredicted near the wall, then k_e is overpredicted, which results in an underestimation of the energy in the lowest wave numbers and therefore an underprediction in the RMS of the pressure fluctuations. However, $3l_t$ will overpredict the energy near the wall and also in the middle of the channel. This will lead to unphysical turbulence near the middle of the channel - l_e more than 2 times bigger than the channel height. This overprediction in the most energetic length scale might be one of the reasons why AniPFM is currently overpredicting the amplitude of displacements in FSI simulations.

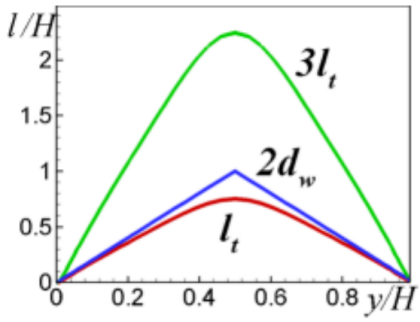

Figure 7.1: Different length scales in turbulent channel flow [10].

Regarding the other length scale, the cut off length scale, l_{cut}, there are two possible approaches. The first one, is the one taken by Shur et al. [10], as seen in Equation 7.15, and the second one is the cubic-root-volume method, as seen in Equation 7.16. The cut-off length will define how much of the energy spectrum will be resolved. For pure fluid flow simulations, van den Bos et al. could not take any conclusion as to which cut off length to choose as they gave different results but both with a similar difference from DNS data. While the cubic root method gave larger estimates of the RMS pressure fluctuations, the Shur et al.'s method gave lower estimations. Due to this reason, van den Bos et al. performed FSI simulations of a flexible brass beam in turbulent water and studied the effect of the cut off length method. The results showed that the cubic root method overpredicts the amount of energy resolvable by the mesh and therefore overpredicts the RMS pressure fluctuations as well as the amplitude. Thus, the Shur et al. method was the chosen one.

$$l_{\text{cut}} = 2\min\left\{\left[\max\left(h_y, h_z, 0.3h_{\max}\right) + 0.1d_w\right], h_{\max}\right\} \tag{7.15}$$

$$l_{cut} = 2V_{cell}^{\frac{1}{3}} \tag{7.16}$$

7.3.3. Wave numbers and vector calculations

The wavenumber corresponding to the energy peak represents the most energetic length scale, and thus should be captured accurately. In order to capture this wave number, k_e, a starting wave number is defined, k_{start}, which should be smaller than k_e. Van den Bos et al. defined two different k_{start} equations, Equation 7.17 and Equation 7.18, where the first one is a more conservative approach and the second one is only applicable for stationary flows. Then, a user input length scale is defined, l_{user}, which denotes the maximum length that can be captured for a certain problem. From here, van den Bos et al. define the k_{start} as Equation 7.19. This is done in order to bound this wavenumber by geometrical constraints. Furthermore, the end of the wave number spectrum, k_{end}, is defined based on the cut off wave number, as seen in Equation 7.20.

$$k_{\text{start}^*} = \frac{\varepsilon}{\max\left(\|\boldsymbol{u}\|^3\right)} \tag{7.17}$$

$$k_{\text{start}^*} = \frac{2\pi}{L} = \frac{2\pi\varepsilon}{K^{3/2}} \tag{7.18}$$

$$k_{\text{start}} = \max\left[\min\left(k_{\text{start}^*}, \frac{1}{2}k_e\right), \frac{2\pi}{l_{\text{user}}}\right] \tag{7.19}$$

$$k_{end} = \frac{3}{2}k_{cut} \tag{7.20}$$

Regarding the wave number space, it goes from k_{start} to k_{end} and the space is divided in N intervals. There are N+1 edge wave numbers. These are used to define Δk_n. Similarly to Kottapalli et al. [17], the wave numbers are distributed logarithmically, as shown in Equation 7.21, where γ is defined as Equation 7.22. The wave numbers are defined as $k_n = \tilde{k}_{n+1/2}$ and Δk_n is defined as $\tilde{k}_{n+1} - \tilde{k}_n$.

$$\tilde{k}_n = k_{start} \cdot e^{\gamma i} \tag{7.21}$$

$$\gamma = \frac{\log\left(k_{end}/k_{start}\right)}{N} \tag{7.22}$$

AniPFM uses the same definition as Kottapali for the wave number vector, Equation 7.23, with θ_n, φ_n as random variables with distribution as shown in Equation 7.24. It can be visualised in Figure 7.2. The continuity constraint is applied the same way as Kottapali et al., $\boldsymbol{k_n} \cdot \boldsymbol{\sigma_n}$ = 0, however the direction vector is obtained in a different way in AniPFM. Kottapali et al. way of determining the direction vector resulted in anisotropic distribution, which in turn resulted in overprediction of the streamwise velocity component and underprediction of the wall normal one. The current method of AniPFM to determine the direction vector makes use of another randomly generated vector denoted $\boldsymbol{\zeta_n}$. This vector has a uniform distribution over a unit sphere and is obtained in a similar way to $\boldsymbol{k_n}$, as seen in Equation 7.25. The direction vector is the normalized cross product between this vector and $\boldsymbol{k_n}$, as shown in Equation 7.26.

$$\boldsymbol{k_n} = k_n \left[\sin\theta_n \cos\psi_n, \sin\theta_n \sin\psi_n, \cos\theta_n\right]^T \tag{7.23}$$

$$P\left(\psi_n\right) = \frac{1}{\pi}, \quad P\left(\phi_n\right) = \frac{1}{2\pi}, \quad P\left(\theta_n\right) = \frac{1}{2}\sin\left(\theta_n\right) \tag{7.24}$$

$$\boldsymbol{\zeta}_n = \left[\sin\theta_\zeta \cos\psi_\zeta, \sin\theta_\zeta \sin\psi_\zeta, \cos\theta_\zeta\right]^T \tag{7.25}$$

$$\boldsymbol{\sigma}_n = \frac{\boldsymbol{\zeta}_n \times \boldsymbol{k}_n}{|\boldsymbol{\zeta}_n \times \boldsymbol{k}_n|} \tag{7.26}$$

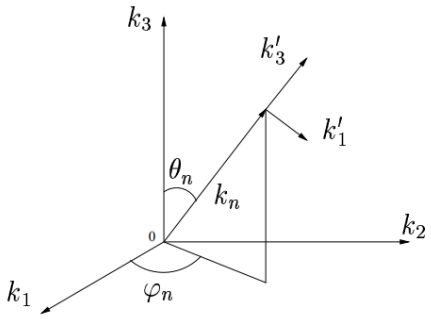

Figure 7.2: Wave vector representation of the n-th Fourier mode [11].

7.3.4. Time correlation

At the end of subsection 7.3.1, a non dimensional spatial only fluctuation field, called $\boldsymbol{w_t}(x)$, was presented. In this subsection it will be presented how AniPFM, through the use of time correlation methods, is able to create a velocity fluctuation signal that is dependent in space and time, from a starting point of an only space dependent velocity fluctuations signal. As it was seen in section 7.1, two main phenomena have to be taken into account: convection of the turbulence and decorrelation due to constant production and dissipation. Van den Bos et al. [34] tested four different methods for temporal correlation/decorrelation. These methods will now be discussed.

Convection and exponential correlation

This method aims to incorporate both effects. The velocity fluctuations are convected by solving Equation 7.27, where $\boldsymbol{v}_t^{m-1}$ are the non-dimensional velocity fluctuations generated at the time step $m-1$ and U_j is the mean velocity component from URANS. Then, a new solution is generated, $\boldsymbol{v}_t^m$, from the previous convected solution, $\tilde{\boldsymbol{v}}_t^{m-1}$ (the twiddle here denotes that the solution of the advection equation is a numerically diffused one and not the exact solution), and a newly generated field $\boldsymbol{w}_t^m$. This is depicted in Equation 7.28, where the coefficients a and b are defined in Equation 7.29 and Equation 7.30, respectively. Here, τ is the turbulent time scale determined from the URANS simulation and f_τ is a modification factor for having some control over the correlation. A factor of f_τ = 17 is used, which was the one that Billson et al. [11] used for the simulation of a 3D jet. The use case of interest for PFM (fuel rod) is very different from the flow in a jet and thus this is a parameter that should be studied in case this time correlation method is used. The coefficients a and b are defined in a way that respects the square mean properties of v_t, $< \boldsymbol{v}_t^2 >= \delta_{ij}$.

$$\frac{\partial \boldsymbol{v}_t^{m-1}}{\partial t} + U_j \frac{\partial \boldsymbol{v}_t^{m-1}}{\partial x_j} = 0 \tag{7.27}$$

$$\boldsymbol{v}_t^m(\boldsymbol{x}, t) = a\tilde{\boldsymbol{v}}_t^{m-1}(\boldsymbol{x}, t) + b\boldsymbol{w}_t^m(\boldsymbol{x}) \tag{7.28}$$

$$a = e^{-f_\tau \Delta t/\tau} \tag{7.29}$$

$$b = \sqrt{1-a^2} \tag{7.30}$$

This method is different from the one from Billson et al. [11], as in theirs, the actual velocity fluctuations, $\boldsymbol{u}_t$, are used for the correlation, which is only possible for steady state simulations. In the case of unsteady simulations, the velocity fluctuations from the previous time step may not contain the same amount of energy as the newly generated ones. The use of non-dimensional velocity fluctuations, $\boldsymbol{v}_t$ and $\boldsymbol{w}_t$, which have constant statistical properties allows them to be used in unsteady simulations. The disadvantage of this method is that by solving the advection equation numerically, numerical diffusion is introduced. Billson et al. [11] used a four-point stencil to avoid this, but still there was energy loss. OpenFOAM only provided second order methods, and thus this problem will be aggravated. This can cause a underestimation of the Reynolds stresses, which leads to an underestimation of the pressure fluctuations.

Rescaled convection and exponential correlation

In the previous method it was seen that numerically solving the advection equation introduced numerical diffusion which causes the solution of $\boldsymbol{v}_t^{m-1}$ to be smeared out. The magnitude of $\boldsymbol{v}_t^m$ should ideally be $\sqrt{3}$ while due to the diffusion error it is less. The rescaled convection and exponential correlation method tries to avoid this by rescaling the newly generated velocity fluctuation field, $\boldsymbol{w}_t^m$, so that overall no energy is lost. Thus, an adjusted value should be used for b. This in turn, will mean that the decorrelation is not exactly met. But, then again, this already happened with the previous method as the $\boldsymbol{v}_t^{m-1}$ is changed when solving the advection equation, which in turn will have an effect on the decorrelation between $\boldsymbol{v}_t^{m-1}$ and $\boldsymbol{v}_t^m$.

In this method, b is defined so that $< (\boldsymbol{v}_t^m)^2 >$ is equal to 1 in each normal direction, which means no energy is lost. The definition of this coefficient is presented in Equation 7.31. It is worth noting that this rescaling may have an impact on the distribution of energy, because in actual cases, the distribution of $< (\tilde{v}_t^{m-1})^2 >$ is not uniform due to differences in diffusion error across the domain.

$$b = \sqrt{1 - \frac{1}{\sqrt{3}} < \tilde{\boldsymbol{v}}_t^{m-1} \tilde{\boldsymbol{v}}_t^{m-1} > a^2} \tag{7.31}$$

Solely exponential correlation

This approach only employs Equation 7.28 to generate time-correlated velocity fluctuations, neglecting the convection of previous fluctuations $\boldsymbol{v}_t^{m-1}$. While this method does not result in an underestimation of Reynolds stresses, it also does not accurately reflect the convection experienced by eddies. This has implications for the frequency spectrum's shape, which is crucial for FSI simulations.

Solely convection

This time-correlation method is widely used in synthetic turbulence generation and has been employed by various authors such as Shur et al. [10], Poletto et al. [121], and Ewert et al. [113]. It generates the velocity fluctuations directly as a function of time (i.e. $\boldsymbol{v}_t(\boldsymbol{x}, t)$) using equation Equation 7.32, where $\boldsymbol{U}$ represents the velocity from a URANS simulation. Unlike Kottapalli et al. [17], who utilized a different definition for the convection velocity, this method accurately captures the Reynolds stresses by utilizing the exact solution of the advection equation, eliminating the need for numerical methods. The random variables in this method are created in the first iteration and stored, as they are not a function of time. This leads to a strong dependence on the random seed of the random number generator, which increases the uncertainty of the results.

$$\boldsymbol{v}_t(\boldsymbol{x}, t) = \sqrt{6} \sum_n \sqrt{q_n} \left[\sigma_n \cos \left(\boldsymbol{k}_n \cdot (\boldsymbol{x} - \boldsymbol{U}t) + \phi_n \right) \right] \tag{7.32}$$

7.3.5. Pressure fluctuations

Now that the modelled velocity fluctuations are completely defined, the pressure fluctuations can be computed. In this subsection it will be discussed the governing equation and the boundary conditions needed.

Governing equation

The governing equation of the pressure fluctuations is a Poisson equation that depends solely on the Reynolds averaged velocity and on the velocity fluctuations, as it can be seen in Equation 6.38. AniPFM calculates the pressure fluctuations based on this equation. Kottapalli et al. [17] started out similarly but then assumed that $\Delta \cdot \boldsymbol{u}'$ holds. While the exact divergence criterion is met, the discrete one is not. This is also why some methods even though classified as divergence-free, in reality their discrete divergence may be non-zero. Therefore, in AniPFM, the pressure fluctuation equation, shown in Equation 6.38, is used to avoid introducing errors from assuming the exact divergence criterion. While this equation considers the full pressure fluctuations, it only accounts for the fluctuations caused by the resolved velocity fluctuations, not the effect of unresolved turbulence. Thus, this method does not fully capture the impact of unresolved turbulence on the pressure fluctuations.

In order to calculate the pressure fluctuations, the spatial mean is subtracted from the right hand side of Equation 6.38, because if the spatial mean is different from zero it causes the solution to be dominated by a three dimensional parabola. In Equation 7.33, this is shown for a 1D Poisson equation,

where the right hand side is decomposed into a spatial average and a fluctuation component. The solution of this equation is shown in Equation 7.34, where it can be seen that the solution has a parabolic behaviour. In order to avoid this, before Equation 6.38 is solved, the spatial average is subtracted to the right hand side. Equation 7.34 still has a linear and constant term, which are determined by the boundary conditions.

$$\frac{\partial^2 p'}{\partial x^2} = rhs' + \overline{rhs} \tag{7.33}$$

$$p' = \frac{1}{2}\overline{rhs}x^2 + c_1 x + c_2 + \iint rhs' dx dx \tag{7.34}$$

Boundary conditions

As it was mentioned, in order to solve the governing equation of the pressure fluctuations, Equation 6.38, boundary conditions are needed. While for RANS, boundary conditions can be very simple, as a uniform value suffices, for the case of AniPFM, it is not so simple. Like DNS and LES, AniPFM has the same problem with regards to boundary conditions: since the flowfield involves fluctuating components, then the boundary conditions cannot be a simple uniform value. The application of AniPFM is in incompressible internal flows, and thus three boundary conditions will be discussed: inlet, outlet and wall. The inlet and outlet conditions are related and thus will be discussed together.

At the wall, the typical boundary condition used regarding the pressure is a zero pressure gradient. This boundary condition applies for the instantaneous solution and for the Reynolds averaged solution, then it must apply also for the fluctuations. Equation 7.35 shows the boundary condition for the pressure fluctuations at the wall.

$$\frac{\partial p'}{\partial n} = 0 \tag{7.35}$$

Regarding the inlet and outlet boundary conditions, there are many options, which can be divided into three types: Dirichlet (fixed value), Neumann (fixed derivative) and Robin (fixed value and derivative). In the case of Dirichlet BC there are three options: periodic, mapped and calculated boundaries. The periodic BC are used for flows that can be considered periodic, i.e. the flow statistics are the same at the inlet and the outlet. Since in reality this is equivalent to prescribing one boundary condition, this means that the problem is underdetermined and thus an extra equation is needed. This is normally the assumption that the mean of the quantity of interest is zero. In this case, that the pressure fluctuations mean is zero across the whole domain. For non periodic flows, mapped or fixed value boundary conditions can be used. For the case of the mapped BC, a slice at a chosen location in the previous method is mapped onto the boundary at the new time step. Concerning the fixed value BC, which is the one used in the inlet/outlet by van den Bos et al. [34] in AniPFM, from dimensional analysis, it is formulated an estimation of the pressure fluctuations with respect to the density and the velocity fluctuations. This relation is then modified calibrated so that the average is zero. This is shown in Equation 7.36.

$$p' = \frac{\rho u'^2}{\sqrt{2}} - \frac{\overline{\rho u'^2}}{\sqrt{2}} \tag{7.36}$$

Lastly, there was also the option of using a Neumann BC for the inlet and outlet. The behavior of using such BC in the full domain will be shown by the comparison with a simpler one-dimensional example , Equation 7.37. The solution to the equation (Equation 7.38) must oscillate around zero and have an average of zero. This requires the coefficient c_1 to be equal to zero. If c_1 is not equal to zero, a linear profile will be present in the solution. With a zero gradient boundary condition at x = 0, Equation 7.39 holds. If the indefinite integral of $f(x)$ at the boundary is not equal to zero, c_1 will also not be equal to zero and a linear profile will be present in the solution. To avoid a linear profile, it is suggested not to use Neumann boundary conditions for the inlet and outlet.

$$\frac{\partial^2 p'}{\partial x^2} = f(x) \tag{7.37}$$

$$p' = c_1 x + c_2 + \iint f(x) dx dx \tag{7.38}$$

$$\frac{\partial p'}{\partial x} = 0 = c_1 + \int f(0)dx \tag{7.39}$$

7.3.6. Flowchart

The working structure of AniPFM is outlined in the flowchart shown in Figure 7.3. This chart lays out the various steps and workflows in the AniPFM system, giving a clear overview of its operational framework. It acts as a useful guide to understand the complex aspects of the model and to track the sequential stages involved in its operation. Consulting this flowchart can provide readers with a solid understanding of how AniPFM functions, laying the groundwork for the discussions in the following chapters.

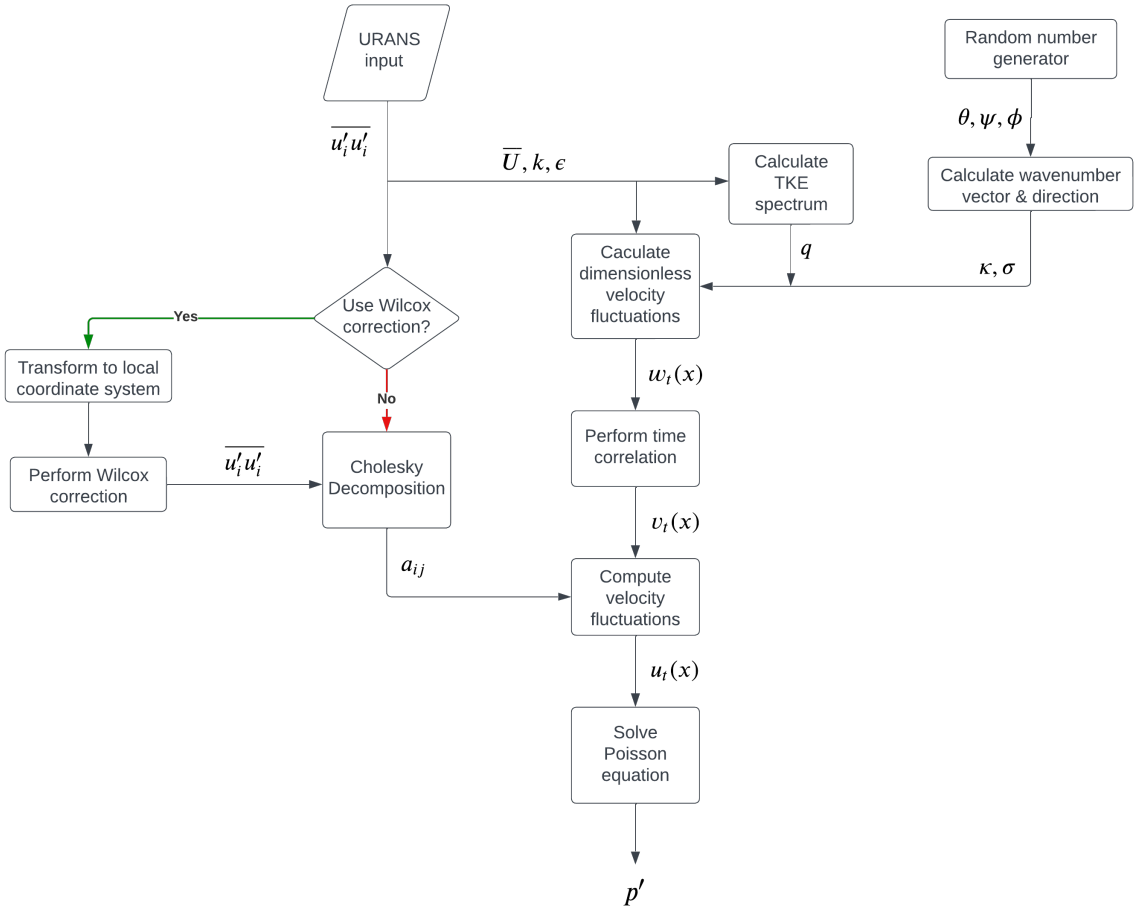

Figure 7.3: Flowchart of AniPFM.

7.3.7. Sensitivity analysis

As it was mentioned, the main problem of AniPFM is the lack of understanding of the model on its different parameters definitions, as well as its uncertainty. With the goal of better understanding the model, reducing the uncertainty and possibly improving the accuracy, a plan will be drafted for what possible parameters need to be studied. For this it will be analysed what was already discussed by van den Bos et al. [34] and whether or not their studies were conclusive to the future choice of said parameter. This overview can be seen in Table 7.1. This table will serve as guidance throughout the research performed during the thesis.

Table 7.1: Sensitivity analysis plan

Parameter / Definition	Brief description	Studied by van den Bos et al. [34]?	Conclusive ?	Study in this thesis?
Number of modes	Used in the Fourier series that generates the non-dimensional space only velocity fluctuations	Only for pure convection	No	✓
Random seed	Used in the pseudo-random number generator to obtain the angles that go into wavenumber vector expression	Limited	Further research is needed	✓
Time Correlation	Applied to the non-dimensional velocity fluctuations to create a velocity fluctuation signal that is dependent in space and time	Yes	Further research is needed	✓
l_e	Length scale that corresponds to the peak of the TKE spectrum	Limited	No	✓
C_l	Calibration constant part of the definition of l_e	No	-	✓
Cut-off length scale	Defines the cut-off wavenumber for the TKE spectrum	Yes	Further research is needed	✓
f_τ	Correlation factor part of C&EC time correlation method	No	-	✓

7.4. Summary

After discussing the turbulence modelling, synthetic turbulence is presented. The requirements of the ST models are discussed based on the characteristics of turbulence reviewed in Chapter 6. Such characteristics entail adhering to the governing equations, modelling of the energy spectrum, replicating the Reynolds stresses and modelling the convection of turbulence and temporal decorrelation caused by constant production and dissipation. Then, the active research areas of ST were presented. From here, the foundation was built and the model this thesis revolves around, AniPFM, was presented. It was analyzed with detail in terms of the generation of the velocity fluctuations, turbulent kinetic energy spectrum, wave number and vector calculations, time correlation and pressure fluctuations. From the discussion of the generation of the velocity fluctuations and its time correlation, it was seen that there is no consensus yet on which time correlation method provides the best accuracy with the least uncertainty. This was one of the gaps identified in the model, which this thesis aims to cover. In the C&EC time correlation method, a fine tuning factor, f_τ, was identified as a parameter which needs to be studied, as the default value from the model of Billson et al. [11] is still being used. Moreover, still in terms of the velocity fluctuations generation, two additional parameters were suggested for further study: the number of modes and the random seed. The sensitivity of the model to these parameters is not fully understood yet. Lastly, regarding the TKE spectrum, two length scales were assessed as requiring further study: the length scale associated with the peak of the spectrum, l_e, and the cut-off length scale, l_{cut}. In the definition of l_e, an empirical constant, C_l, was also identified as a parameter to

be studied in this thesis, as the value that is being currently used is calibrated for a plane mixing layer, which is inherently different from the flow case of interest of this thesis.

Part III

Towards a Robust Model: Improvements, Verification & Validation

”*All models are wrong, but some are useful*.”
George E.P. Box

8 Turbulent channel flow

Now that all the theory and literature has been presented, it is time to analyze, further understand and hopefully improve AniPFM.

There are three distinct components involved in the verification and validation process for the implementation of AniPFM. These are verifying and validating the AniPFM's capability to accurately model pressure fluctuations, validating the accuracy of the URANS turbulence model + AniPFM in representing the Reynolds stress tensor, and evaluating the ability of implementing the AniPFM within the NRG-FSIFOAM framework to predict the vibration amplitude of a nuclear fuel rod under axial flow conditions.

AniPFM is quite complex by itself. It has a lot of parameters that need to be defined by the user, which require understanding of the model but also of the flow in question. In order to further understand the model and the best parameters configurations for a certain flow, validation is needed. Running complete FSI simulations increases even more the complexity of the simulations and thus increases the run time and the difficulty to draw conclusions regarding the accuracy of the AniPFM by itself as well as the optimal parameters. That is why pure flow simulations play an important role in the validation of AniPFM. They provide less complexity as well as more data regarding flow quantities, which are crucial to validation. In this chapter and the next one, the fluid-only simulations are presented.

8.1. Introduction

In this chapter, the simulations of the turbulent channel flow (TCF) case are discussed. This case was chosen due to its simplicity and because of the high availability of DNSs. The setup was made to replicate the DNS results of Abe et al. [122]. These researchers performed a DNS study on the Reynolds-number dependence on pressure fluctuations in TCF. Their highest Reynolds number is Re_τ = 640, and thus this is the one chosen to replicate in our setup. This DNS was selected because it provided data on the mean flow characteristics, such as velocity profiles and Reynolds stresses, but also other quantities, such as spectral information regarding pressure and velocity. Furthermore, it also provides two-point correlations of velocity fluctuation signals which will prove to be useful for calibration of time correlation methods.

A sketch of TCF is shown in Figure 8.1. In the TCF, the flow is between two parallel plates, as shown in Figure 8.1, where $L \gg \delta$ and $b \gg \delta$. L and b are large enough so that the flow in the edges can be considered uncorrelated. This allows us to take a smaller section in the middle of this larger channel and use periodic boundary conditions in the streamwise and spanwise directions. The flow is statistically homogeneous in these directions which means that it can be averaged in space, resulting in one final line of data depending only on the wall normal direction, y. This is the beauty of the turbulent channel flow and why so many turbulence researchers use this case to study wall bounded turbulence.

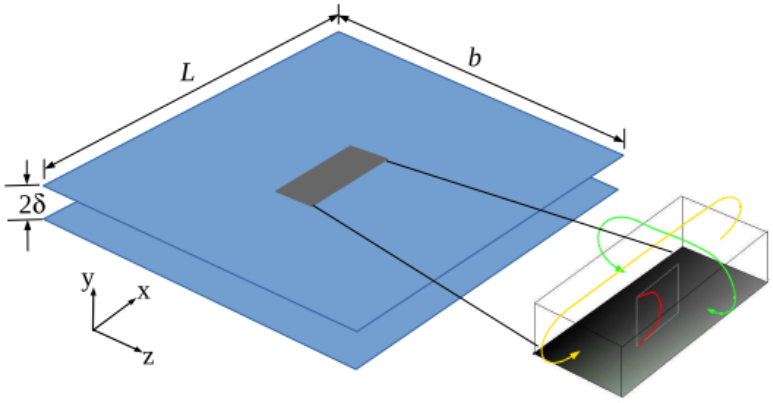

Figure 8.1: Sketch of turbulent channel flow [12] (Modified).

8.2. Simulation setup

Although this setup was already mentioned in van den Bos et al. thesis, it will be described here also for completeness of this thesis. The simulation domain is set at dimensions of $6\delta \times 2\delta \times 3\delta$, with δ representing the mid-channel height, which is equal to 1 in this case (in meters). The mesh dimensions are $N_x \times N_y \times N_z$, where these values are varied resulting in different mesh resolutions. The grid is evenly spaced in the x and z directions, but expands geometrically from the wall towards the mid-channel in the y direction. All the different meshes are wall resolved and such that $y^+ \leq 1$. This parameter y^+ is a non-dimensional wall distance and it is given by Equation 8.1, where u_τ is the friction velocity (shown in Equation 8.2), y is the distance to the closest wall and ν is the kinematic viscosity, which is set to ν = 2e-5 $m^2 s^{-1}$.

$$y^+ = \frac{y u_\tau}{v} \tag{8.1}$$

$$u_\tau = \sqrt{\frac{\tau_w}{\rho}} \tag{8.2}$$

The findings from this test case will be benchmarked against the DNS of Abe et al. [122] with a Reynolds number of Re_τ = 640, as detailed in Equation 8.3. Abe et al. established that Re_τ equates to a bulk Reynolds number, Re_{bulk} = 24,228, further described in Equation 8.4 and Equation 8.5. The same Re_{bulk} as Abe et al. is used. Given the periodic boundary conditions, to ensure flow, a pressure gradient needs to be set, achieved by adding a momentum source to the Navier-Stokes equations. In OpenFOAM, a bulk velocity force is applied, setting the resultant flow's speed. The viscosity and mid-channel height determine this bulk velocity. There's no wall model as the y+ value of the first cell is smaller than 1, ensuring the flow is resolved to the wall. A backward time scheme offers second-order accuracy in time. The time step is constrained by the CFL number, capped at 0.5. The PISO algorithm handles the equation system per time step. For the convergence of the governing equations, an absolute threshold of 1e-6 is set for all equations, including the pressure fluctuation equation.

$$Re_\tau = \frac{u_\tau \delta}{v} \tag{8.3}$$

$$Re_{\text{Bulk}} = \frac{U_{\text{Bulk}} 2\delta}{v} \tag{8.4}$$

$$U_{\text{Bulk}} = \frac{1}{\delta} \int_0^\delta u \, dy \tag{8.5}$$

The coarsest mesh used can be visualized in Figure 8.2. This mesh has 40x80x60 elements.

First, a steady state simulation using the $k - \omega$ SST turbulence model is ran until the residuals are converged. This simulation is used to initalize the flowfield of an unsteady simulation using AniPFM, which is run for 300 seconds (equivalent to roughly 12 flow-throughs). This was found to be enough for having converged root mean square pressure fluctuations for all the meshes considered.

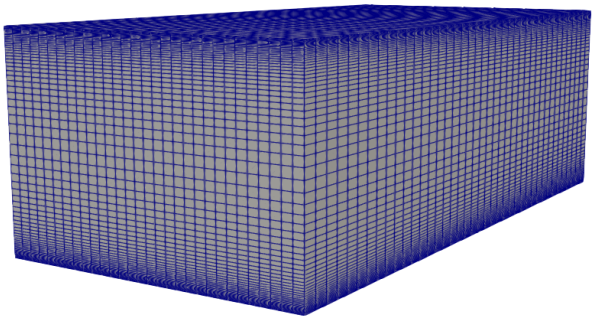

Figure 8.2: TCF mesh.

The AniPFM settings used in each section/subsection of this chapter are summarized in Table 8.1, such that the reader has a more clear overview of what parameters are being used.

Table 8.1: Summary of AniPFM parameters used in each section/subsection

(Sub)section	#modes	Rand. seed	Time corr.	f_τ	l_e	C_l	Cut-off
section 8.3	256	Default (0)	C&EC	25	$C_l l_t$	3.0	Shur
section 8.4	256	Default (0)	C&EC	25	$C_l l_t$	3.0	Shur
subsection 8.5.2	Varying	Default (0)	C&EC, PC	25	$C_l l_t$	3.0	Shur
subsection 8.5.3	256	Varying	C&EC, PC	25	$C_l l_t$	3.0	Shur
subsection 8.5.4	256	Default(0)	(R)C&EC, PC	Varying	$C_l l_t$	3.0	Shur
section 8.6	256	Default(0)	C&EC	25	$C_l l_t$	3.0	Shur
subsection 8.7.1	256	Default(0)	C&EC	25	Both	Varying	Shur
subsection 8.7.2	256	Default(0)	C&EC	25	$C_l l_t$	Varying	Both
subsection 8.7.3	256	Default(0)	C&EC	25	$C_l l_t$	2.0	Shur

As mentioned before, the channel flow is only statistically inhomogeneous in the y direction and thus unless mentioned otherwise, the results presented have been averaged in the statistical homogeneous directions. Furthermore, when one-dimensional spectra are displayed, they are averaged over the other homogeneous direction. For example, if a spectrum is shown in the streamwise direction, it's averaged over the spanwise direction.

8.3. Qualitative results

Statistics of the flow quantities, while extremely relevant, can sometimes paint a misleading picture. Relying solely on quantitative information can risk omitting nuances or the broader context. Therefore, it is crucial to complement statistical analyses with qualitative data. By examining such data, a more comprehensive understanding can be ensured as well as validate whether the numbers truly align with what is seen and expected.

In Figure 8.3, the instantaneous velocity and pressure fluctuations are shown for a cutoff plane in the middle of the channel. In the case of the velocity fluctuations, the x-direction component is shown. At first glance, these fluctuations seem chaotic and do not follow any clear pattern. In terms of the pressure fluctuations, these seem to be stronger near the wall and weaker near the middle of the channel.

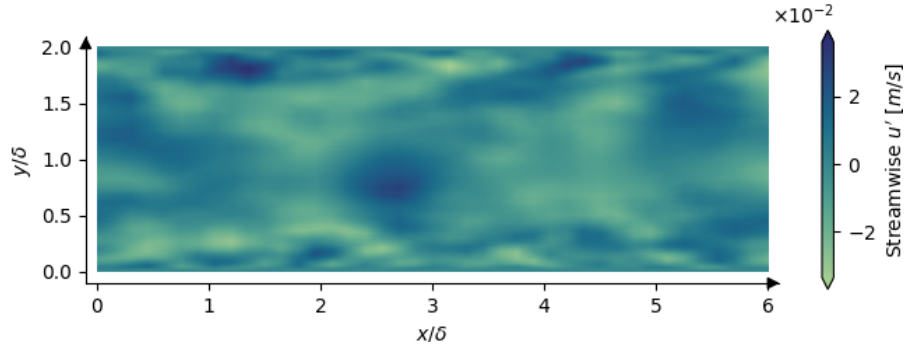

(a) Velocity fluctuations

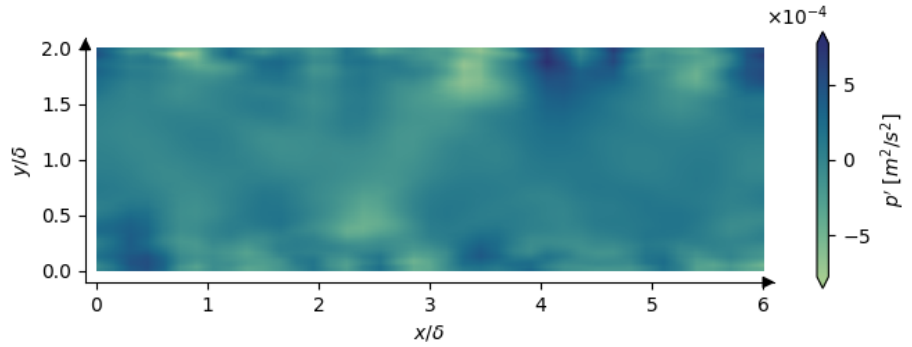

(b) Pressure fluctuations

Figure 8.3: Instantaneous velocity and pressure fluctuations fields in a plane in the middle of the channel.

Figure 8.4a shows the mean squared velocity (x-component) fluctuations as well as the mean squared pressure fluctuations. Here a tendency can be seen for both with increasing value near the wall and decreased near the middle of the channel. As it was seen before, to obtain the pressure fluctuations, the model solves a Poisson equation where the RHS only depends on the mean squared velocity fluctuations (normal components of the Reynolds stress tensor) and on the mean velocity. This is why the behaviour of the mean squared pressure fluctuations resembles the one of the mean squared velocity fluctuations. It can be noted, however, that the tendency, while similar, shows some differences, with the mean squared pressure fluctuations showing a higher value only very close to the wall while the mean squared velocity fluctuations show this also a bit further away from the wall. This will be addressed later on the report.

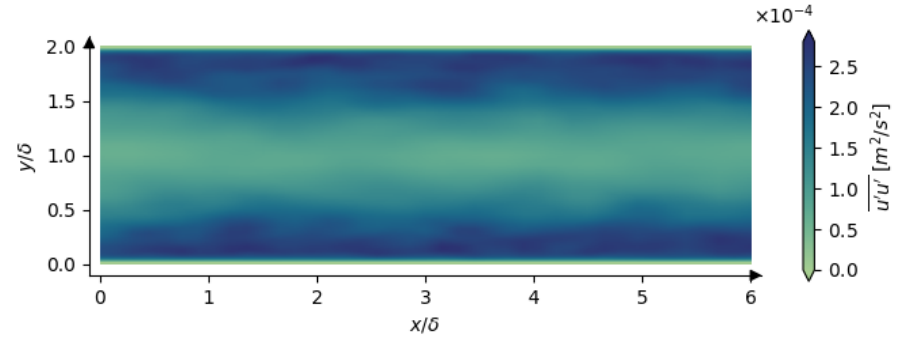

(a) Mean squared velocity fluctuations

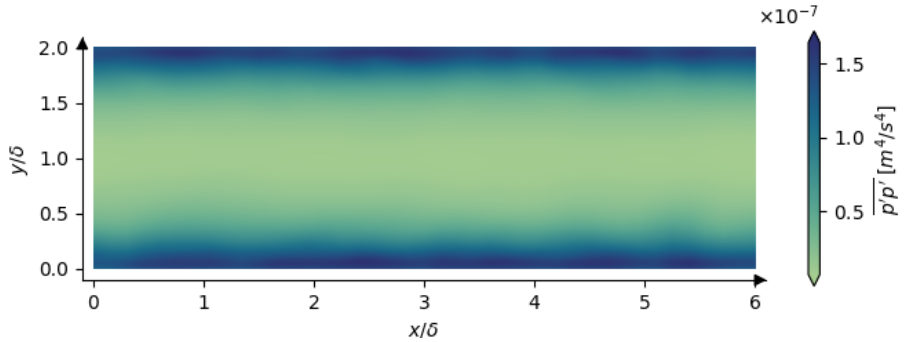

(b) Mean squared pressure fluctuations

Figure 8.4: Mean squared velocity and pressure fluctuations in a plane in the middle of the channel.

8.4. Mesh study

Mesh studies are important in ensuring the accuracy and fidelity of computational fluid dynamics simulations. The quality and resolution of the mesh can significantly influence the results, potentially leading to numerical errors or convergence issues. Recognizing this significance, in Table 8.2, the different mesh resolutions employed for this case are shown. Furthemore, as mentioned before, the CFL number was constrained at 0.5 for all meshes by using a dynamic time step. The average CFL number for all meshes is roughly 0.45.

Table 8.2: TCF mesh Resolutions

Mesh	N_x	N_y	N_z	N_{cell}
M1	40	80	30	96,000
M2	50	96	40	192,000
M3	80	112	60	537,600
M4	120	128	90	1,382,400

Figure 8.5 shows the root mean squared pressure fluctuations along the wall normal coordinate for the different meshes compared to DNS data. When comparing the meshes, a clear convergence is observed: as the mesh resolution increases, the curves come closer together. An increase in resolution also leads to higher pressure fluctuations due to the greater amount of resolved turbulence kinetic energy (up to a certain converged value). Moreover, the finer meshes capture the increase in turbulent production in the buffer layer more accurately. When set against DNS data, the overall shape of the curves is quite similar, with a few key differences: an underestimation of the production term increase in the buffer layer, a reduced prediction of pressure fluctuations away from the wall (which is not of primary concern for AniPFM), and close to the wall at $y^+ < 10$, an overestimation of RMS pressure fluctuations.

This overprediction might be why the FSI simulations by van den Bos et al. [34] reported increased displacement amplitudes. If this is indeed the reason, it becomes essential to determine what aspect of the AniPFM model is responsible for it, how it can be adjusted, and then validate the changes in both fluid and FSI scenarios.

In the following sections the mesh used by default is the coarse one, unless mentioned otherwise. This is done to speed up the simulation time. The conclusions taken from the results are considered valid and generalizable for finer meshes in terms of trends but not absolute values. The generalization to finer meshes is done in subsection 8.7.3.

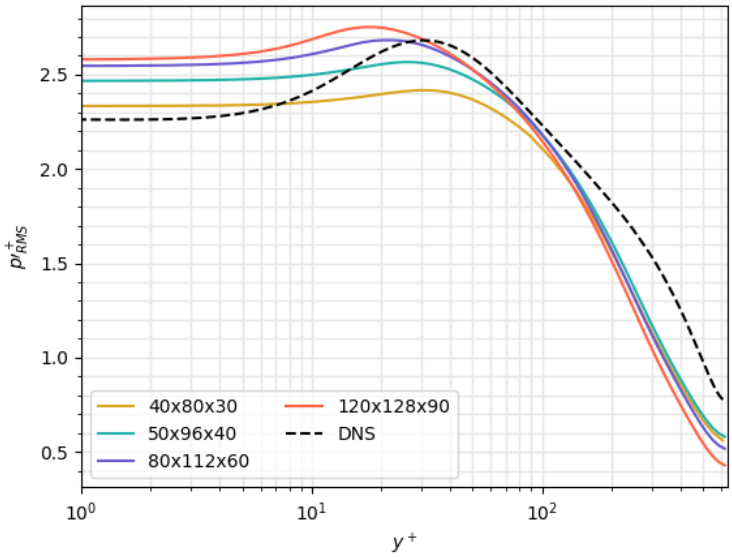

Figure 8.5: Root mean square of the pressure fluctuations along the wall normal coordinate for different meshes.

8.5. Time Correlation

In Chapter 7 AniPFM was presented. One of the sections discussed was the different time correlation methods that are possible to use with AniPFM.

Van den Bos et al. [34] analyzed different aspects of the influence of the different time correlation methods on both fluid and FSI simulations. In the end the pure convection method and the convection & exponential correlation proved to have somewhat similar results from their analysis, and since the pure convection is more computationally friendly, it was the one that was used in most of the simulations. While it is indeed the most computationally friendly method, it has some clear drawbacks. This was already hinted at in the end of van den Bos' thesis as one of the likely reasons of AniPFM uncertainty. In this section, the time correlation methods will be assessed, mainly the pure convection and the convection & exponential correlation, looking to continue van den Bos' studies and to decide which method is more suitable.

8.5.1. Analytical analysis

First, an analysis can be made just by looking at the equations and making some predictions, which can later be corroborated by numerical simulations.

The convection & exponential correlation shows great potential as it incorporates both convection and turbulence decorrelation due to production and dissipation. Its main drawbacks being the fact that additional equations (compared to pure convection) need to be solved which might increase simulation time, and the fact that these equations involve numerical approximation of derivatives introducing numerical diffusion, which might decrease the magnitude of the velocity fluctuations near the wall and thus decrease the magnitude of the pressure fluctuations. There is a rescaled version of this method as it was shown, which rescales the energy such that in principle no energy is lost. The only drawback

seen when looking at the equations of this method is that by rescaling the energy, then it changes the decorrelation term of the velocity fluctuations. If this method indeed rescales the energy correctly then it is a promising method.

Lastly, the pure convection method, as shown in Equation 7.32, utilizes the exact solution of the advection equation, which means that no numerical diffusion is introduced. From an analytical point of view, the drawbacks are: not considering turbulence decorrelation; since the generated velocity field is not a function of time (the field is always the same just convected), it should have a greater dependence on the random seed as well as the number of modes of the Fourier series than the other methods. An upside from this method, besides not introducing numerical diffusion, is its simplicity.

8.5.2. Number of modes

Now that the equations have been analysed and some hypothesis/predictions have been laid out, it is time to check them. This is done by running simulations with the different correlation methods.

First, the dependency on the number of modes used in the Fourier series that generates the velocity fluctuations is analyzed. This is done by running simulations with both time correlation methods (C&EC and pure convection) with number of modes varying from 64 to 2048. The RMS pressure fluctuations along the wall normal coordinates for these various number of modes are shown in Figure 8.6.

From Figure 8.6a, it can be seen that, as expected, the pure convection method is very dependent on the number of modes. While the curves collapse for higher y^+, for the lower y^+ values (which are the ones of interest) there is a great difference in the magnitude of the RMS of pressure fluctuations. Furthermore, the method shows no signs of convergence (at least with the number of modes analysed here): there is no clear trend in the curves. It can be speculated that a higher number of modes would need to be used to achieve some level of independence. This would lead to an increase in computational cost.

On the other hand, Figure 8.6b shows that the C&EC method is independent on the number of modes used. This is a great plus for this method as higher number of modes increase computational cost.

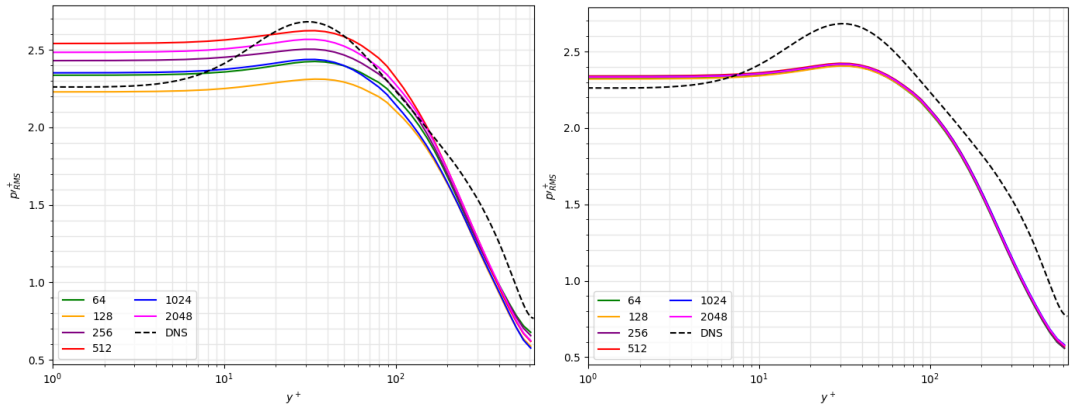

(a) Pure convection **(b)** Convection & Exponential Correlation

Figure 8.6: Root mean square of the pressure fluctuations along the wall normal coordinate for various numbers of modes.

It is also important to understand what is the relation between the number of modes used and the simulation time. A higher number of modes is expected to increase the time AniPFM spends generating the velocity fluctuations. Furthermore, it is also crucial to see what is the difference in simulation time between the C&EC and pure convection methods.

Before delving deeper into the analysis, it's essential to address a procedural detail regarding the execution of the simulations. To maintain consistency and mitigate any potential bias in the results due to performance variability, all simulations were conducted on the same node of NRG's cluster. It is noteworthy that even nodes with identical hardware in NRG's cluster show performance variations. Hence, using the same node for all simulations ensured a standardized environment and more reliable outcomes.

Figure 8.7 shows the simulation duration for different number of modes for both time correlation methods. Unlike what was expected, C&EC and pure convection show essentially the same simulation time. It was expected that since C&EC has to solve more equations it would be more costly. Although in this analysis the same time step was used in both methods, in reality the C&EC method requires stricter time steps than pure convection to ensure convergence. This means that if the maximum allowed time steps are used, then simulations using the C&EC method will take longer than those using pure convection. This will be mentioned later in the context of FSI simulations.

Moreover, as expected, the simulation time increases with the number of modes. By fitting a linear curve to the data, the slope obtained is m = 0.45 for the C&EC method and m = 0.44 for the PC method. The difference between them is negligible. The data does not seem to exhibit a linear behaviour. Instead, it shows more of a exponential one. By fitting an exponential curve of the form $y(x) = ae^{bx}$, the coefficients obtained are a = 1.39e3, b = 6.67e-4 for the C&EC method and a = 1.33e3, b = 6.78e-4 for the PC method. These values can be used as future reference for similar setups to estimate the increase of simulation time by increasing the number of modes.

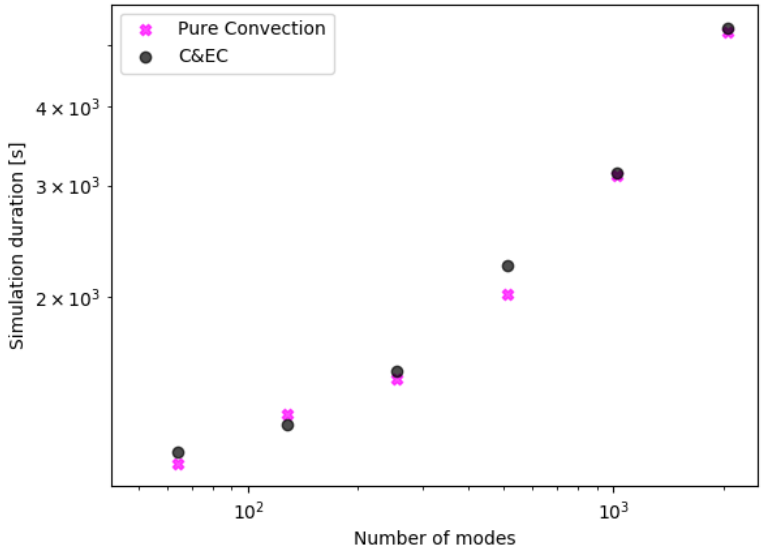

Figure 8.7: Simulation duration for different number of modes.

8.5.3. Random seed

As it was seen in Chapter 7 (Equation 7.23 and Equation 7.24), the wave number vector, $\boldsymbol{k_n}$, and the auxiliary vector, $\boldsymbol{\zeta}_n$, which will be part of the expression for the direction vector, are obtained through sines and cosines of random variables. These random variables are generated by a pseudo random number generator (RNG). Although RNGs generate numbers that seem random, most of them are actually deterministic in nature (hence 'pseudo'). Given the same seed, they will produce the same sequence of numbers every time. This property can be useful in situations where reproducibility is desired, which is the case of AniPFM. As such, the random seed is one of the user inputs of the model.

AniPFM is inherently a stochastic model, depending on random variables for the generation of the velocity fluctuations field. While this dependency is intrinsic to the method, ideally, the generated velocity fluctuations would not differ much when different random seeds are using. This would allow a more 'deterministic' like (but still stochastic) turbulence generation. This in turn, would lead to lower standard deviation in the RMS pressure fluctuations and thus less uncertainty in the predicted amplitude of displacements in the case of FSI simulations. In light of this, the effect of the random seed on the different time correlation methods will now be analysed.

Figure 8.8 shows the RMS pressure fluctuations in wall coordinates at y^+ = 10 averaged over time, w.r.t the random seed for different time correlation methods. As expected from our analytical analysis, the pure convection method shows a clear dependence on the random seed, whereas the C&EC does

not (or at least to a much lower extent). Quantifying this dependency, in the case of PC, on average, the difference between using different random seeds and the baseline seed (considered 0 here) is roughly 5%. On the other hand, for C&EC simulations, this value is 1.37%.

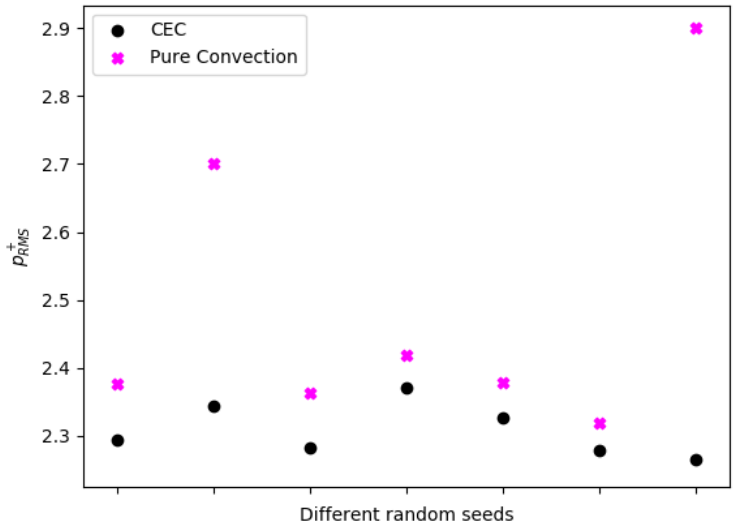

Figure 8.8: RMS pressure fluctuations at y^+ = 10 for different random seeds.

8.5.4. C&EC calibration

The C&EC method has shown very promising results compared to the other time correlation methods. Much like other areas of AniPFM, this method also needs to be calibrated. As mentioned in section 7.3, there is a control parameter, f_τ, which can be seen in this model's equations (Equation 7.27 - Equation 7.30). This parameter is one of the user inputs of AniPFM. Until now, a value of f_τ = 17 was used which is the same as the one used by Billson et al. [11] (this time correlation method partially built from his approach). Billson et al. used this value for a simulation of a 3D jet. And since our use case is different, it is worth seeing what is the model sensitivity to this parameter and what is its optimal value.

Let us start by looking at the equations and analyse the influence this parameter is expected to have:

$$\uparrow f_\tau \Rightarrow \downarrow a \Rightarrow \uparrow b \Rightarrow \text{ Less weight to } \boldsymbol{v}_t^{m-1} \text{ and more to } \boldsymbol{w}_t^m \,,$$

$$\downarrow f_\tau \Rightarrow \uparrow a \Rightarrow \downarrow b \Rightarrow \text{ More weight to } \boldsymbol{v}_t^{m-1} \text{ and less to } \boldsymbol{w}_t^m \,.$$

Remember that $\boldsymbol{v}_t^{m-1}$ is the convected previous velocity fluctuations field and $\boldsymbol{w}_t^m$ is the newly generated field. This means that a higher f_τ will put more weight onto the newly generated field and a lower f_τ onto the convected field from the previous solution. As it was seen, to obtain the convected field, $\boldsymbol{v}_t^{m-1}$, the advection equation, Equation 7.27, is solved, which introduces numerical diffusion. So it is expected that a lower f_τ velocity fluctuations field will have less energy than a higher f_τ one.

During the rest of this subsection, the effect of this parameter will be assessed as well as the comparison with other methods such as the rescaled version or pure convection.

TKE, pressure fluctuations and Reynolds stresses

In this part, the models will be evaluated in terms of the quantity of most interest for this project, the pressure fluctuations. Since the pressure fluctuations rely on velocity fluctuations and the latter on turbulent kinetic energy, those will also be evaluated.

In Figure 8.9 is shown the resolved turbulent kinetic energy w.r.t the wall normal coordinates for C&EC with different f_τ values ranging from 1 to 100 as well as to RC&EC and pure convection. The

resolved TKE is determine dividing the input TKE from the URANS simulation by the one obtained though the velocity fluctuations generated by AniPFM. As expected, lower f_τ values cause a greater and greater loss of energy. This is very pronounced for f_τ = 1, which shows the degree of energy that is lost due to numerical diffusion when solving the advection equation. For values of f_τ from 25-100 the difference very near the wall is none, with only difference starting from around y^+ = 50. The pure convection shows almost no loss of energy as expected. Furthermore, the rescaled version of C&EC shows an incorrect rescaling of the energy. It rescales the energy for greater values than the ones taken as input from URANS. Furthermore, the rescaling does not work well: ideally the rescaling should rescale the energy to the same value (1, which means no loss of energy) for different f_τ values. As it can be seen in the figure this is not the case. f_τ values which originally have a lower resolved TKE get a much greater increase, resulting in as much as 1.6x of the input TKE. It is not clear what is causing this. If this method were to be used, the equation for the coefficient b would have to be revised. As it is now, it is overpredicting the energy lost by numerical diffusion and thus in the rescaling processing it is introducing more energy in the system than it originally had from the URANS input.

From this plot, it can be concluded that f_τ values ranging from 25 to 100 have a similar behaviour near wall, which is the part of most interest to the application of AniPFM. It also shows that the rescaled version of C&EC can be discarded. The pure convection shows good results in this section.

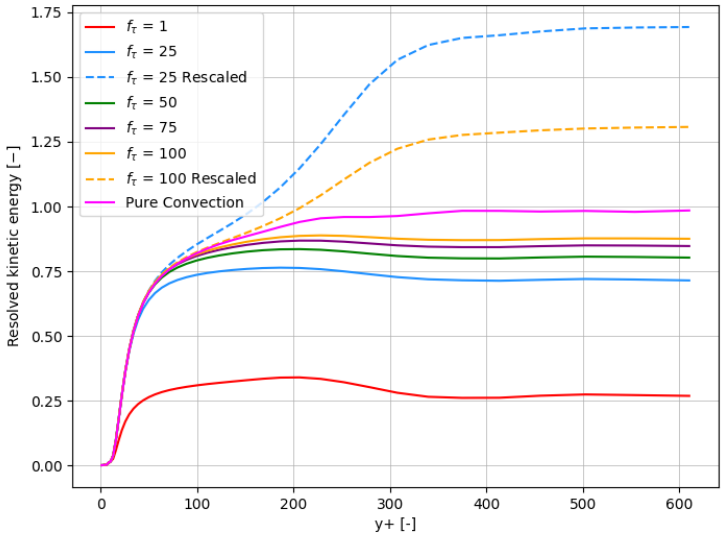

Figure 8.9: Resolved TKE for different time correlation methods.

Now that the TKE has been analysed, the next step is to study the effect on the Reynolds stresses. These are shown in Figure 8.10 (DNS data is not shown here as its $\overline{uu}$ component is considerably higher in magnitude than the ones seen here, causing this data to become barely distinguishable). Only the normal components are shown as those are the ones that are more important. In terms of the C&EC method, the conclusions that can be taken from here are very similar from the ones taken from the previous figure: higher f_τ values show more energy, converging towards f_τ = 100. On the other hand, the pure convection method shows some interesting results. It shows some wiggles, which are not characteristic of the Reynolds stresses and are probably due to the periodic nature of this method, that fails to account for other physical phenomena happening in turbulence, other than convection.

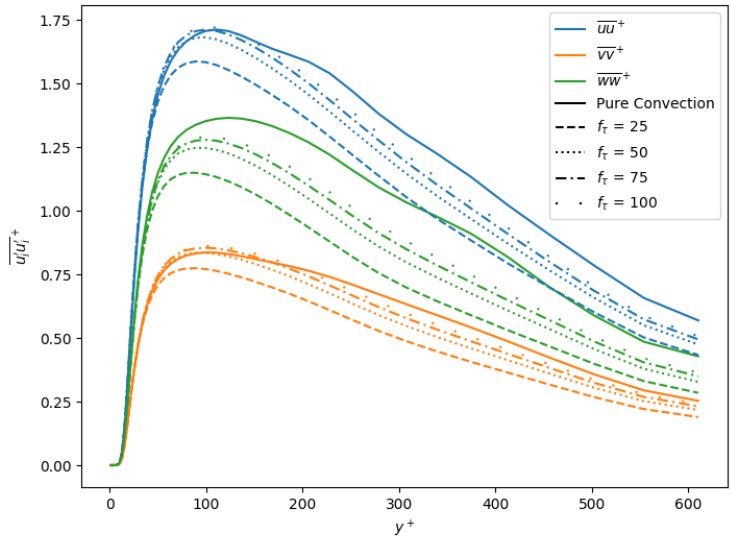

Figure 8.10: Normal Reynolds stresses along the wall-normal coordinate for various time correlation methods.

Finally, the RMS of the pressure fluctuations in wall coordinates along the wall normal coordinate are show in Figure 8.11. For the C&EC, the results show what had already seen before. Using values of $f_\tau \geq 25$ is the ideal. While at a first glance the pure convection method seems to yield results akin to those of the C&EC method, it is essential to note that this resemblance is coincidental, stemming from the specific combination of the random seed and number of modes used in this case. Indeed, the pure convection method demonstrated a pronounced sensitivity to variations in these parameters, as detailed in subsection 8.5.2 and subsection 8.5.3, a characteristic not shared by the C&EC method which maintains its performance relatively unaffected by changes in the number of modes and the random seed.

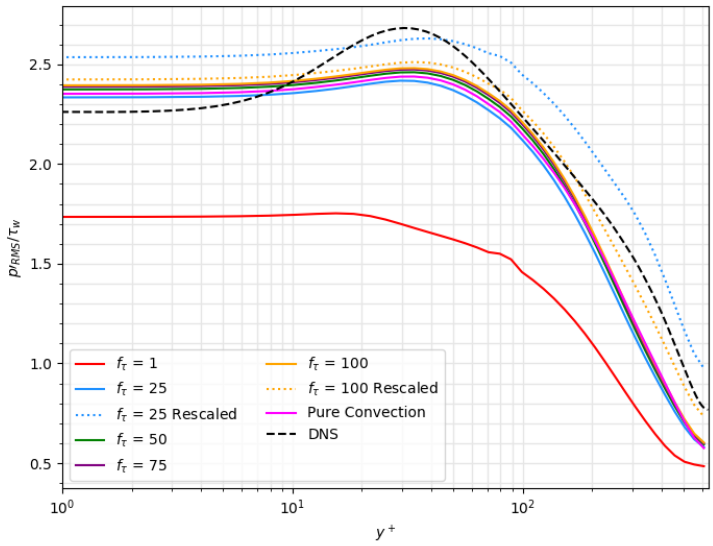

Figure 8.11: RMS pressure fluctuations along the wall-normal coordinate for various time correlation methods.

From this analysis, some conclusions can already be taken, but those are solely based on the energy based quantities and not so much on the physicality of the generated turbulence. This last part is what will be analysed in the following two parts.

Two-point correlation

Turbulence, with its complex and multi-scale nature, demands effective tools for analysis. One of the widely-used methods to study turbulent flows is the two-point correlation technique. This method measures the similarity or correlation between signals at two spatial points based on their separation distance. When applied to velocity fluctuations in a turbulent flow, it provides valuable information about spatial relationships and coherence within the flow.

Mathematically, the two-point correlation, $R(\mathbf{r})$, for a velocity fluctuation field, $u(\mathbf{x})$, can be expressed as:

$$R(\mathbf{r}) = \langle u(\mathbf{x}) \cdot u(\mathbf{x}+\mathbf{r}) \rangle \,, \tag{8.6}$$

where $\langle \cdot \rangle$ denotes the ensemble average, **x** is the set of points in space, and **r** is the separation vector between the two points being considered. The use of this technique aids in the assessment of the physicality of the generated turbulence by the different time correlation methods. Note that in the following figures if a two-point correlation is showed in the spanwise direction it means it was averaged in the streamwise direction and vice-versa. Moreover, all the two-point correlations were averaged in time for the last 0.5 flow-throughs with sets of data every time step. As such the expression for the two-point correlation used is slightly different from the one presented above:

$$R_{ij}(\mathbf{r}) = \frac{\Big\langle \langle u_i(\mathbf{x},t) \cdot u_j(\mathbf{x}+\mathbf{r},t) \rangle_{\text{space}} \Big\rangle_{\text{time}}}{\Big\langle \langle u_i(\mathbf{x},t) \cdot u_j(\mathbf{x},t) \rangle_{\text{space}} \Big\rangle_{\text{time}}} \,. \tag{8.7}$$

The correlation is normalized as to ensure that the maximum absolute value is 1.0, which corresponds to a fully correlated signal if positive and fully uncorrelated if negative.

Limited by the available DNS data of two-point correlation of velocity fluctuations for the Re_τ of the current study, once again the valuable data of Abe et al. [122] DNS was used. They have available data both for streamwise and spanwise two-point correlation, for the three velocity fluctuations components at two different y^+ values: y^+ = 325.8 (around mid-channel) and y^+ = 5.38.

Figure 8.12 shows the streamwise two-point correlation coefficients of velocity fluctuations for y^+ = 325.8 for C&EC with different correlation factors and for pure convection. R_{ii} corresponds to the two-point correlation of the i^{th} component of the velocity fluctuations vector. The different plots have a few features in common: correlation factors of 25-100 provide similar results whereas a correlation factor of 1 and pure convection show very different results; there is a relation between the initial gradient of the curve and the correlation factors - lower correlation factors (more focus on convection) show a less steep gradient (take slightly longer to decorrelate), whereas higher correlation factors show a steeper gradient; pure convection and C&EC with f_τ = 1 show some periodicity in the results, with it being more chaotic and irregular in the former and smoother in the latter - it is noteworthy that even after extensive averaging both spatially and temporally, sufficient to eliminate local variations and irregularities, this periodicity persists, which reaffirms that the periodicity is intrinsic to the method. Furthermore, comparing with DNS data, it is noticeable that while the u component is not very close to the data, the v and w components are quite close in the overall shape. However, AniPFM decorrelates slower than DNS and it also shows more amplitude of correlation/decorrelation after reaching 0 correlation. Lastly, in the middle of the channel (x^+ = 2000), AniPFM ends up at a slightly deviation from zero (R_{ii} = -0.05), whereas DNS is at zero for R_{ii}. This deviation, at half the computational domain, indicates that there are large scales structures present in the center of the channel, for which the computational domain used is not large enough to capture [122]. This deviation from DNS data, may mean that the energy in the middle of the channel is being overpredicted. While the area near the middle of the channel is not the most important one, it still has an effect on the system's dynamics and overall energy.

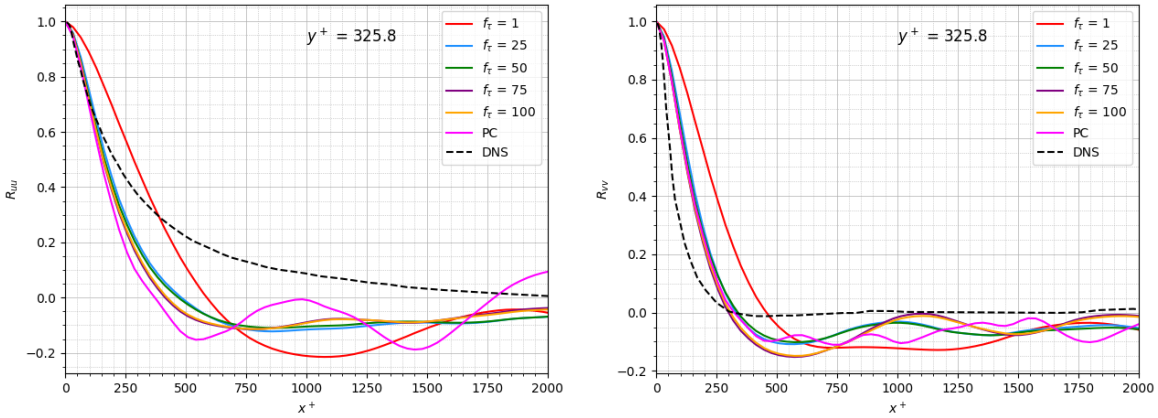

(a) R_{uu} **(b)** R_{vv}

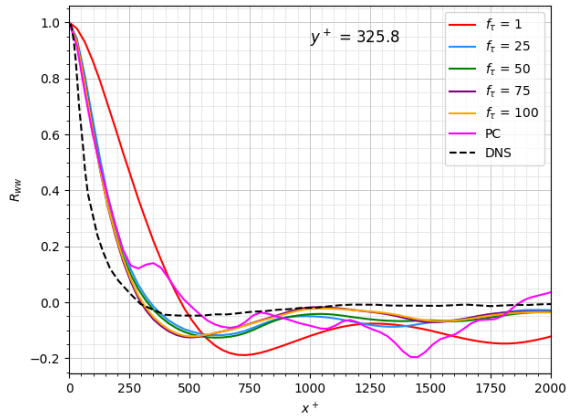

(c) R_{ww}

Figure 8.12: Streamwise two-point correlation coefficients of velocity fluctuations for y^+ = 325.8.

Figure 8.13 shows also the streamwise two-point correlation but for y^+ = 5.38 instead. In this case, AniPFM for all methods shows a very fast decorrelation which is in agreement for the v and w components, but not so much for the u component. This difference between AniPFM and DNS for the streamwise component was also seen in for y^+ = 325.8. One possible explanation would the presence of streaks in DNS which AniPFM is not able to simulate. This would also help explain why the difference is more prominent for lower y^+ values, which is where streaks are seen. While this might be one of the causes, it is not clear what is causing the faster decorrelation of AniPFM compared to DNS for y^+ = 325.8, as there are usually no streaks there. Furthermore, Pure convection shows strong periodicity, unlike C&EC and DNS. This periodicity is dangerous especially near the wall as it might cause physically incorrect excitation to the structure in the case of FSI simulations. Moreover, it is interesting to note that f_τ = 1, unexpectedly, performs similarly to other correlation factors for this case.

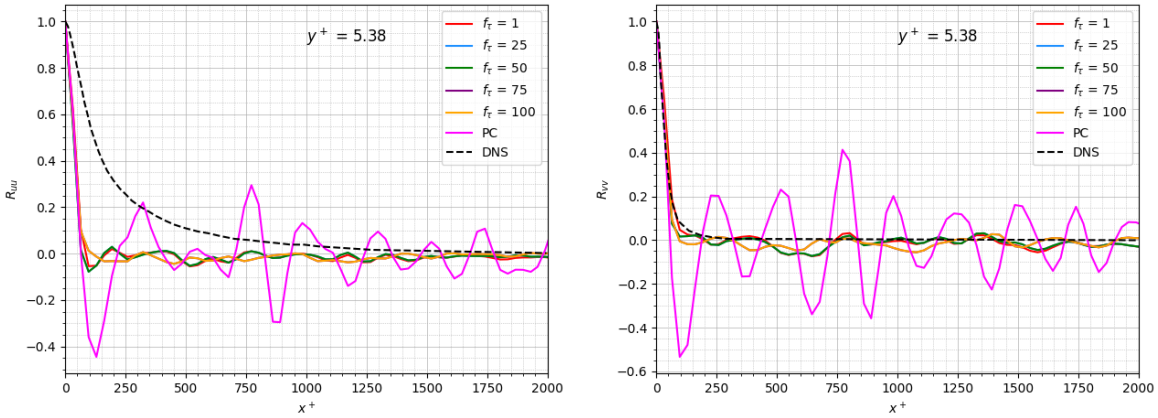

(a) R_{uu}

(b) R_{vv}

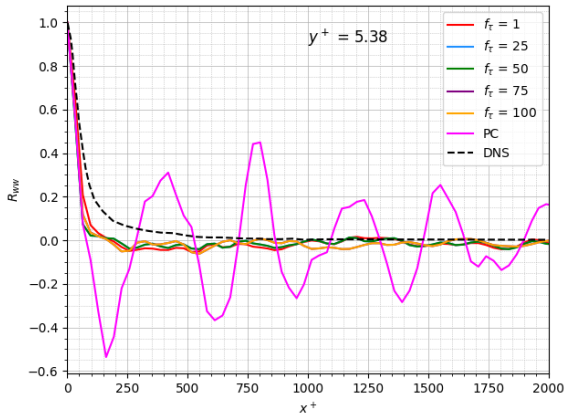

(c) R_{ww}

Figure 8.13: Streamwise two-point correlation coefficients of velocity fluctuations for y^+ = 5.38.

Now that the streamwise two point correlations have been assessed, it is time for the spanwise ones. In Figure 8.14 this is shown for y^+ = 325.8. It is noteworthy how close AniPFM is to DNS data. This is most likely because the time correlation of the velocity fluctuations does not have a large impact on the spanwise direction and mostly on the streamwise direction. In this case the deviation from zero at z^+ = 640 is in agreement with DNS data [122]. In terms of the differences between the different methods, there is not as much as the one seen before (which is likely also explained by the same argument mentioned above regarding the impact of the time correlation in the spanwise direction). Although, pure convection and a correlation factor of 1 still stand out compared to the others.

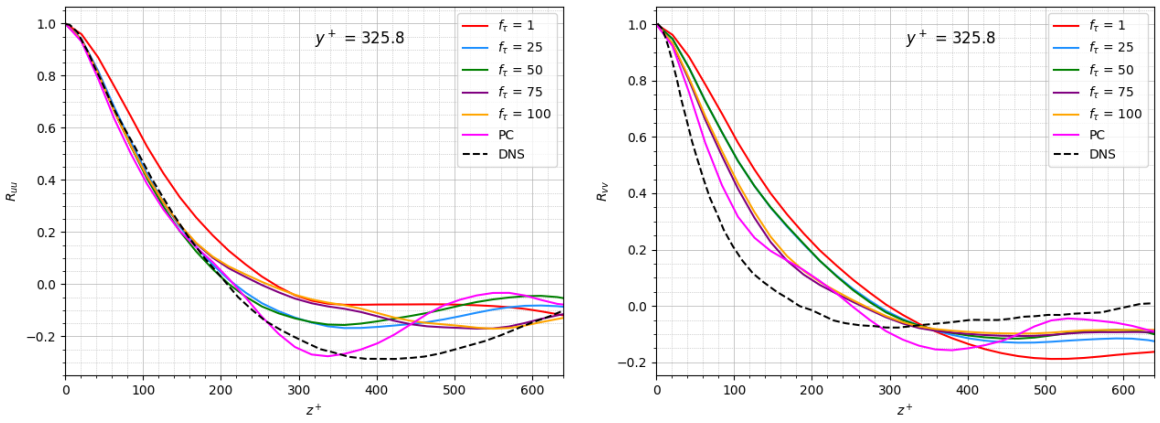

(a) R_{uu}

(b) R_{vv}

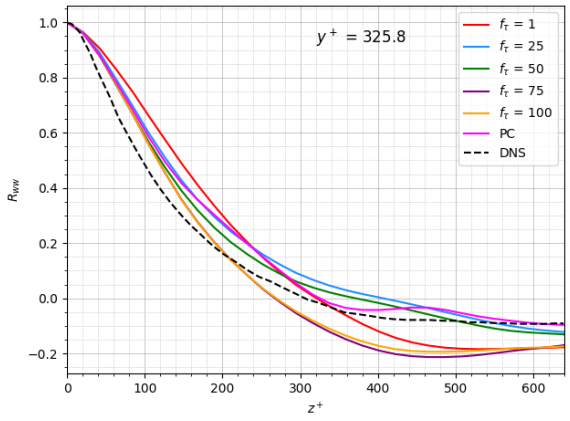

(c) R_{ww}

Figure 8.14: Spanwise two-point correlation coefficients of velocity fluctuations for y^+ = 325.8.

Lastly, in Figure 8.15 is shown the spanwise two-point correlation for y^+ = 5.38. The plots here show a similar behaviour to the ones in the same y^+ but in the streamwise direction: a rapid decorrelation for the C&EC methods and a very high periodicity for the pure convection method. The results are in good agreement with DNS data, except for the v component, which fails to predict the decorrelation of the signal close to the wall. Moreover, it can be seen how similar AniPFM plots look for the different components. This similarity was also observed in the previous figures. While DNS data of the v and w component was similar for most of the plots seen, the u component usually standout as different, which AniPFM failed to predict. This is tied with the fact that AniPFM treats the different components in the same way in a lot of its parts. One possible improvement is to further increase the anisotropy in AniPFM, by for example having an energy spectrum for each direction, with a cut-off frequency that is a vector instead of a scalar. These are just a few examples, but this can be applied in other parts of the model.

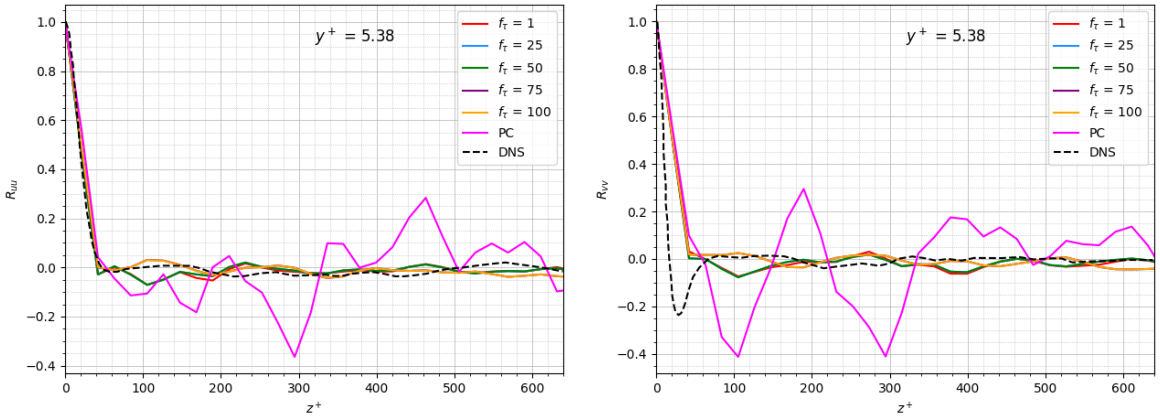

(a) R_{uu}

(b) R_{vv}

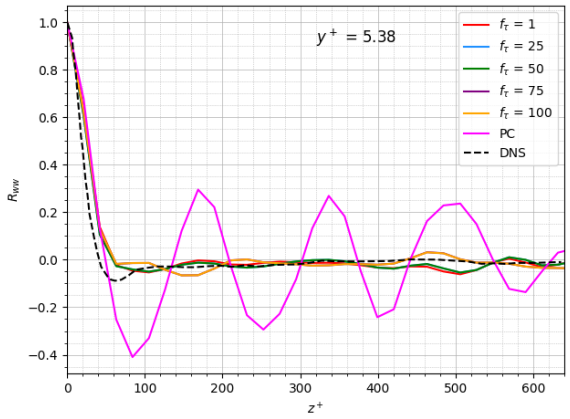

(c) R_{ww}

Figure 8.15: Spanwise two-point correlation coefficients of velocity fluctuations for y^+ = 5.38.

Physicality of the synthetic turbulence

To continue the study of the physicality of the generated turbulence, a quadrant analysis was performed and will be presented here. First, an introduction on quadrant analysis of turbulent flows will be given.

In 1972, Wallace et al. [123] introduced the concept of quadrant analysis for the Reynolds shear stress. Wallace's team discerned value in the signs of the velocity fluctuations and categorized their products into four distinct groups: Q1 (+u, +v), Q2 (-u, +v), Q3 (-u, -v), and Q4 (+u, -v). These groups later became known as the quadrants of the Reynolds shear stress plane. It is evident that the Q2 and Q4 motions correspond to the ejection and sweep events, where ejections correspond to a movement away from the wall and backwards and sweep events correspond to a down and front movement. Meanwhile, Wallace et al. termed the Q1 and Q3 motions as "outward" and "inward" interactions respectively [124].

As an example as well as validation information, in Figure 8.16 is show a quadrant analysis of a turbulent channel flow at Re_τ = 180 at a location of $y^+ \approx 20$, performed by Kim et al. [13]. As it can be confirmed by the figure, in the buffer layer (10 < y^+ < 30), the events that are most common are Q2 and Q4 events, ending up with a joint probability density function (pdf) that looks like a normal distribution stretched in the diagonal between Q2 and Q4.

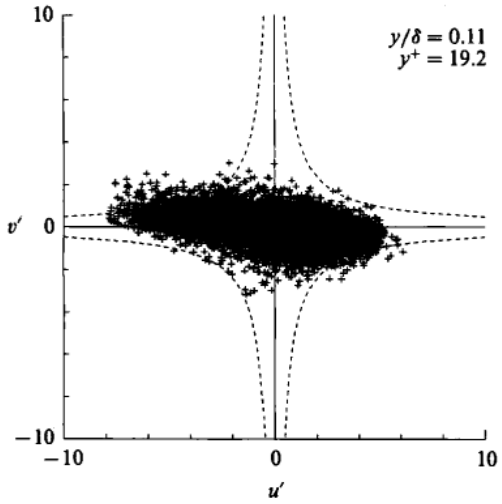

Figure 8.16: Distribution of (u', v') at y^+ = 20 [13].

In order to perform the quadrant analysis in this thesis, multiple probes were placed at a location of y^+ = 10 throughout the domain. From these probes, the velocity fluctuations were retrieved and averaged ending up with one final vector with the size of the amount of measured time steps. In Figure 8.17 are shown the joint probability density functions between the streamwise and wall-normal velocity fluctuations for the pure convection method and C&EC with different correlation factors. When looking at the plots, clear differences emerge in the pure convection and C&EC graphs when $f_\tau = 1$, which matches what was seen earlier. For convection and exponential correlation with correlation factors between 25 and 100, the results are very similar. This similarity fits our expectations. The stretching we mentioned before is clearly visible, with a strong emphasis on Q2 and Q4 events. The distribution for a correlation factor of 1 is a bit different but still highlights Q2 and Q4 events. The joint pdf of pure convection, however, is different from typical patterns in literature for such y^+ values. Overall, the C&EC method performs well, especially with correlation factors of 25 or higher, while the pure convection method doesn't align as closely with DNS data.

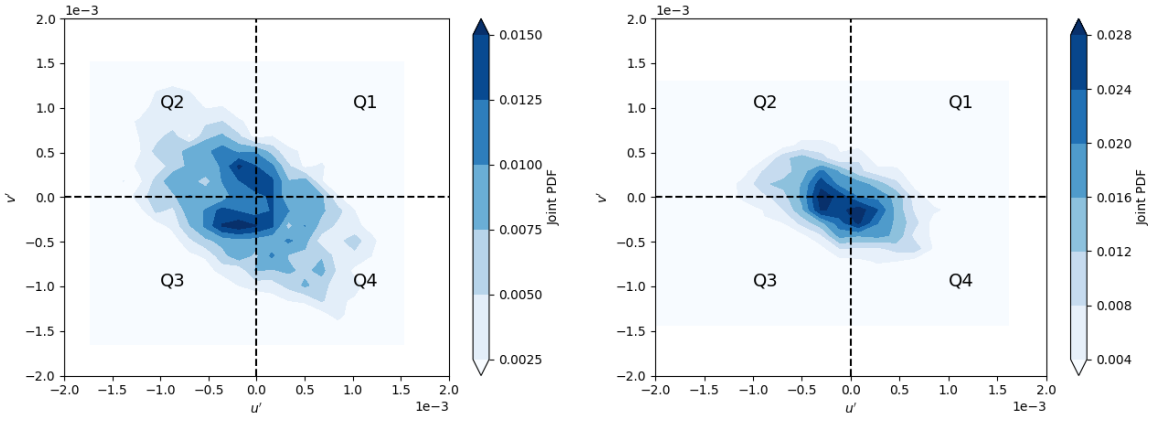

(a) Pure Convection

(b) C&EC w/ f_τ = 1

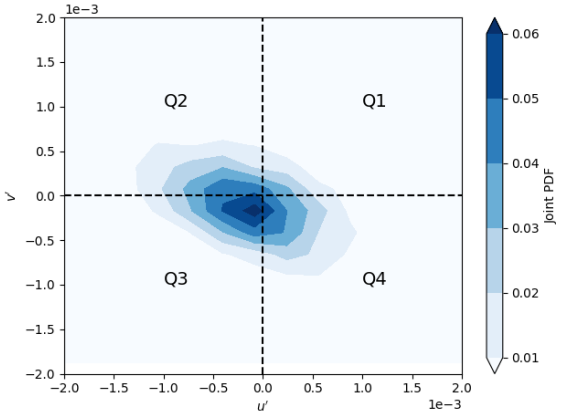

(c) C&EC w/ f_τ = 25

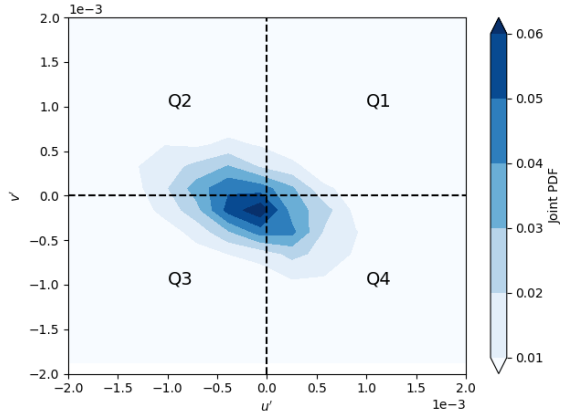

(d) C&EC w/ f_τ = 50

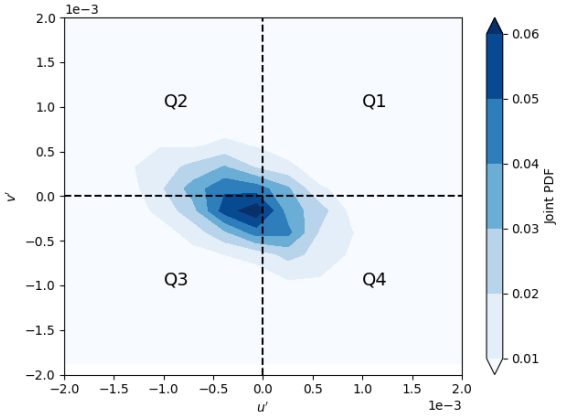

(e) C&EC w/ f_τ = 75

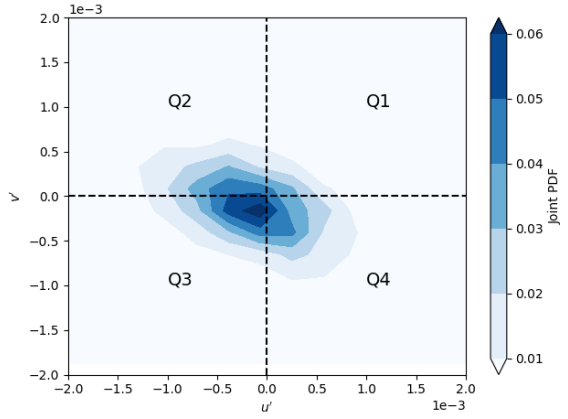

(f) C&EC w/ f_τ = 100

Figure 8.17: Joint pdf of u' and v' at y^+ = 10.

8.6. Why are the pressure fluctuations being overpredicted?

At the end of section 8.4 it was seen that AniPFM was overpredicting the pressure fluctuations near the wall (y^+ < 10). It was hypothesized that this could be the reason why the FSI simulations performed by van den Bos et al. [34] were overpredicting the root mean square of the amplitude of displacements. In that section, the ending thought was that it if indeed this hypothesis was true, then it would be important to understand what in AniPFM is causing the increased pressure fluctuations near the wall, or at least what can be done to decrease them.

To better understand the potential cause, it is important to first examine the pressure fluctuations equation, which is shown in Equation 6.38. As it can be seen there is a clear effect from the velocity fluctuations on the pressure fluctuations. Thus, in order to better understand what is causing the overprediction of the pressure fluctuations, the Reynolds stresses will be analysed.

Figure 8.18 shows the comparison of the normal Reynolds stresses between DNS, AniPFM and the input RANS (with Wilcox correction) for the different meshes. Comparing AniPFM results with DNS, it is evident that the streamwise and spanwise components of the Reynolds stresses are far from being resolved. The wall-normal component on the other side is much better resolved. Comparing the results between differerent meshes, it becomes clear that the increase in mesh resolution increases the amount of turbulent kinetic energy resolved, with this increase most noticeable very near the wall. Finally, comparing with the input RANS RST (which in reality is just RANS TKE to which the Wilcox correction is applied), it becomes clear that as the mesh resolution increases the Reynolds stresses of AniPFM become closer and closer to the input ones. In van den Bos thesis [34], the effect of the turbulence model used in URANS in AniPFM results were studied, mainly $k-\omega$ SST and $k-\epsilon$. The former showed better results near the wall in terms of the Reynolds stresses (after Wilcox correction) and thus was the chosen one. Indeed this model performs better (at least in the wall normal component, not so well in the streamwise one), but it is still not perfect, obviously. For the medium and fine meshes it shows an overprediction of the $\overline{v'v'}$ component near the wall.

Now that the Reynolds stresses have been analysed, the focus can go back to the main question of this section: why are the pressure fluctuations being overpredicted? In the previous paragraph it was seen that the streamwise and spanwise components of the Reynolds stresses are for from being resolved. So, from a crude analysis, it could be said that it would only make sense that the pressure fluctuations should be underpredicted. However, this is not what is happening. This can be explained by simplifying the pressure fluctuations equation for the case of TCF. In this case, the derivatives of the mean flow velocity and of the Reynolds stress tensor in the x and z-direction are equal to zero. From this, Equation 8.8 is derived. One can notice that especially the derivative of the Reynolds stress in the wall-normal direction is important. This dependency on the wall-normal component of the Reynolds stresses helps explains why the pressure fluctuations were being overpredicted near the wall. However, the relation between both is not trivial. For example, for M1, as it can be seen in Figure 8.18a, AniPFM underpredicts the v component when compared to DNS, however from Figure 8.5 it was observed that this mesh is already overpredicting the root mean square of the pressure fluctuations near the wall. While the relation between these quantities is still not clear, there is a clear dependency of the pressure fluctuations on the $\overline{v'v'}$ component.

$$\frac{\partial^2 p'}{\partial x_i \partial x_i} = -\rho \left(\frac{\partial U}{\partial y} \frac{\partial v'}{\partial x} - \frac{\partial \overline{v'\nu'}}{\partial y^2} + \frac{\partial}{\partial_i \partial_j} u_i' u_j' \right) \tag{8.8}$$

Note the in the case of interest of this thesis (annular flow) this equation will be similar with dependence only on the streamwise and radial component (considering cylindrical coordinates with r, θ and z). This will be discussed in the next chapter.

Now, that the origin of the overprediction of pressure fluctuations near the wall is better understood, it is time to shift the focus of the attention to possible solutions for this problem. This will be the theme of the following section.

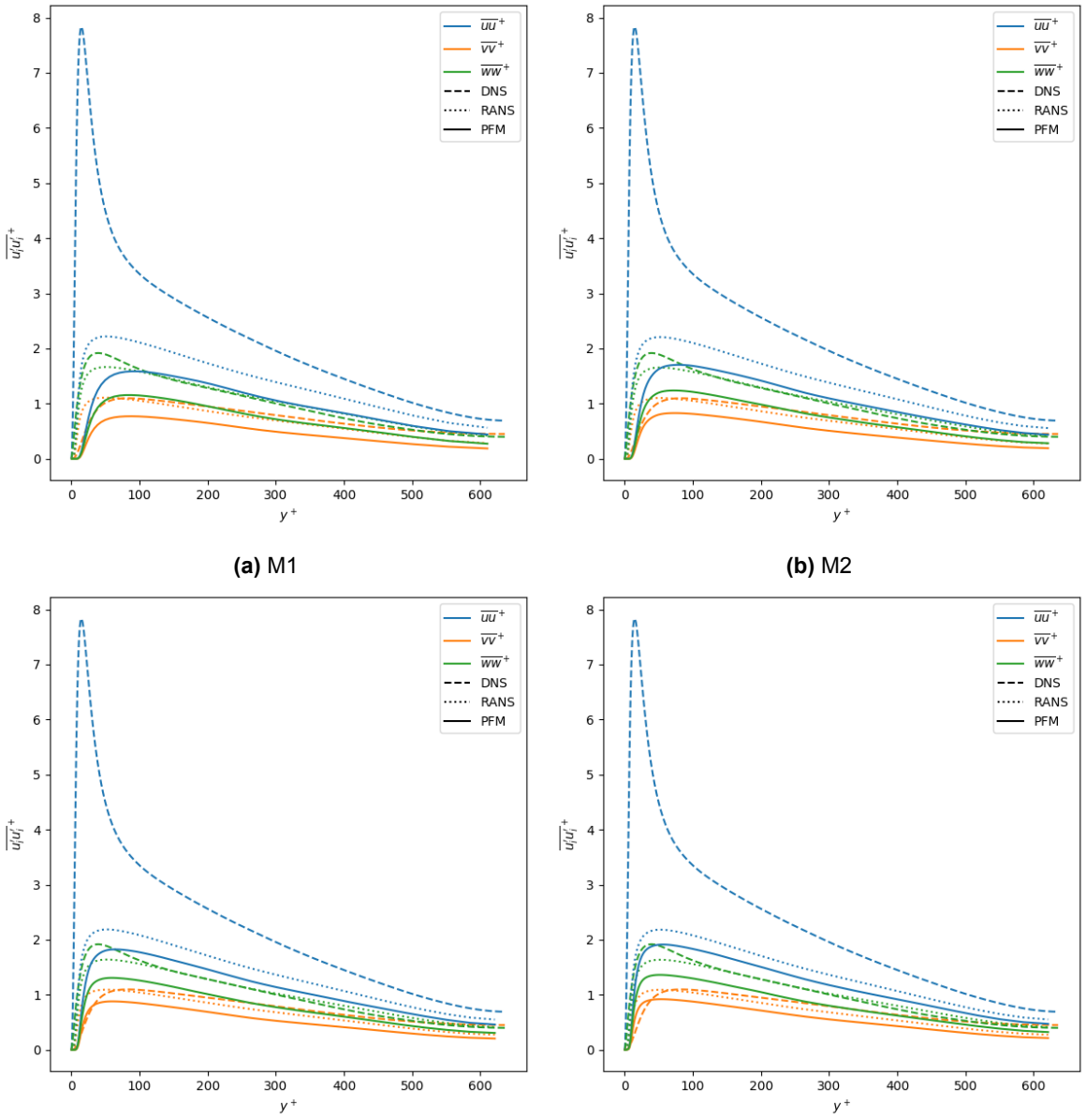

(a) M1 **(b)** M2

(c) M3 **(d)** M4

Figure 8.18: Normal Reynolds stresses for different meshes.

8.7. Turbulent kinetic energy spectrum

To address the overprediction of pressure fluctuations near the wall using AniPFM, the turbulent kinetic energy spectrum equation and its terms were examined, checking for consistency, physical meaning and underlying assumptions.

This analysis starts by reviewing the equation used for the TKE spectrum, Equation 7.10. This equations depends on: the wavenumbers, k (unchangeable); the wavenumber which corresponds to the TKE peak, k_e; the highest wavenumber, k_η; and the cut off frequency, f_{cut}. The expression k_η, Equation 7.13, is based on Kolmogorov's second similarity hypothesis and it is usually the expression used for computing this wavenumber. Where the model has more room for change is in the definition of k_e and f_{cut}. These are the ones that will be given focus in this thesis. The wavenumber k_e will be analysed first, followed by f_{cut}.

8.7.1. TKE peak wavenumber

As it was mentioned in subsection 7.3.2, there are two possible ways of defining l_e:

$$l_e = C_l l_t = C_l \frac{k^{3/2}}{\epsilon} \qquad \text{and} \qquad l_e = \min(2d_w, C_l l_t)\,.$$

They are both taken from Shur's model [10], although van den Bos et al. [34] opted for the first definition and Shur opted for the second one. Van den Bos et al.'s choice was motivated by a brief study that indicated that the second definition would lead to lower magnitude of pressure fluctuations. The goal of this section is to further understand the effect the definition of this length scale has on the generated velocity fluctuations and pressure fluctuations as well as possibly adapt it to possibly correct the overprediction of pressure fluctuations near the wall.

Figure 8.19 shows the RMS pressure fluctuations w.r.t y^+ for the two different definitions of l_e mentioned above as well as for $2d_w$. The last one is also included to understand what is actually happening inside the minimization function. As the figure shows, the curve of $2d_w$ and Shur's definition collapse, which means that $2d_w$ is always smaller than $3l_t$. This is a confirmation of Figure 7.1, which already showed this. The only reason Shur [10] still chose this approach is because they use their zonal RANS/LES not only on TCF but also other cases (for example: turbulent BL), where $2d_w$ is not always smaller than $3l_t$. That being said, using the minimization function in AniPFM case which is always meant for wall bounded flows makes no sense. Furthermore, it also confirms van den Bos [34] study, showing that indeed it underpredicts the pressure fluctuations. Thus, from now on, the focus will be on the first definition of l_e.

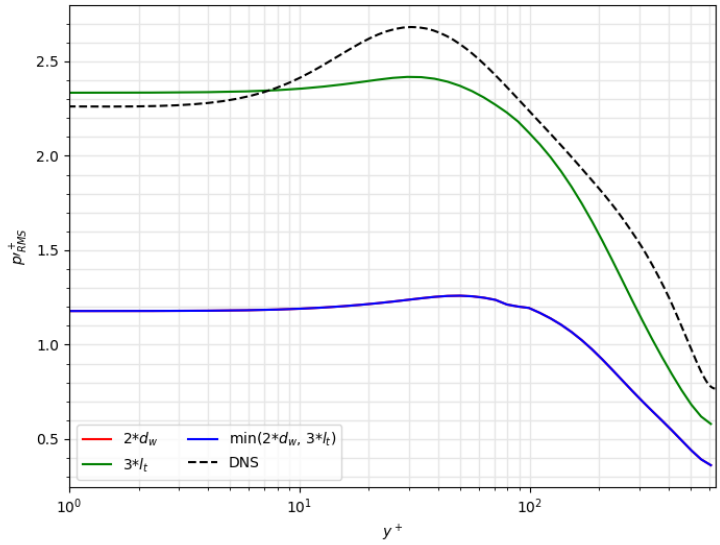

Figure 8.19: RMS pressure fluctuations along the wall-normal coordinate for different l_e definitions.

The C_l value of 3.0 used in AniPFM in the definition of l_e comes from Shur et al. [10] who adjusted this empirical constant to match experimental simulations of a plane mixing layer. This case is clearly very different from the use case of AniPFM, which is more geared towards wall bounded flow over fuel rods. Thus, it is important to calibrate this constant for AniPFM. In Figure 8.20 it is showed that by decreasing the value of C_l, the RMS pressure fluctuations at the wall better align with DNS data. Let us try to understand what is happening by lowering the C_l value that leads to this. By lowering it, the predicted length scale at which the TKE spectrum has its peak is lower, which means that the corresponding wavenumber, k_e, is higher. This then means that the peak of the TKE spectrum goes to the right. Moreover, it is hypothesised the energy content associated with a higher wavenumber will be lower than the one associated with a lower wavenumber. While this is true for the most part of the

TKE spectrum, it is not necessarily true for the initial part of the spectrum, where the spectrum can show an increasing behaviour instead of a decreasing one. However, this assumption seems valid for the range of wavenumbers studied here. This means that the peak itself will happen at a lower TKE, which means that the energy content of the lower wavenumbers before the peak will also have a lower energy content. So, the lowering of C_l can be visualised as a down shift of the TKE spectrum as well as a shift to the right of the spectrum. The implications of this on the pressure fluctuations are seen in the figure: as C_l is lowered, the curve shifts downwards and the peak slightly shifts to the right.

From the figure, one can observe that while the shift downwards is true for y^+ < 100, it is not true for higher y^+ values, as the curves collapse onto themselves for different C_l values. This is something that is going to be explored in the next chapter.

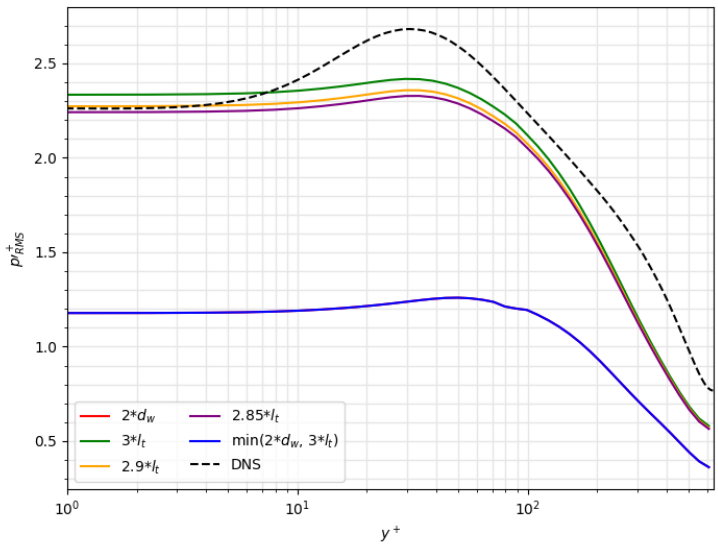

Figure 8.20: RMS pressure fluctuations along the wall-normal coordinate for different l_e definitions and C_l values, using the Shur cut-off.

8.7.2. Cut-off wavenumber

As mentioned in the beginning of this section, one of the definitions where AniPFM has room for change as well as need for deeper understanding on its influence on the model is the cut-off frequency. Two possible definitions are considered: the one by Shur et al. [10], Equation 7.15, and a simpler definition, Equation 7.16, which will be named cubic cut-off from here on. The latter was discarded by van den Bos et al. [34] as it was shown to overpredict the TKE and thus the pressure fluctuations near the wall. In the previous subsection it was shown that by modifying the C_l value, it is possible to scale the turbulent kinetic energy near the wall and match the RMS pressure fluctuations to DNS data. Consequently, if this same approach is applied to the cubic cut-off it is possible to scale down the energy near the wall and better compare both filters. Because in the end, what is of most interest is the shape of the l_{cut} along the channel height, as it was shown it is possible to shift the energy up or down easily.

Figure 8.21 shows the comparison of the RMS pressure fluctuations w.r.t the y^+ for simulations using the cubic cut-off with different C_l values for the l_e definition. Like it was shown for the Shur cut-off, it is shown here that it is also possible to calibrate the constant C_l for this cut-off method. As expected a smaller value is needed as the cubic cut-off cuts the energy spectrum at a higher wavenumber than the Shur cut-off. Comparing both cut-offs with the optimised coefficients, the cubic cut-off shows a better overall shape. It shows a more pronounce peak than the one with Shur cut-off.

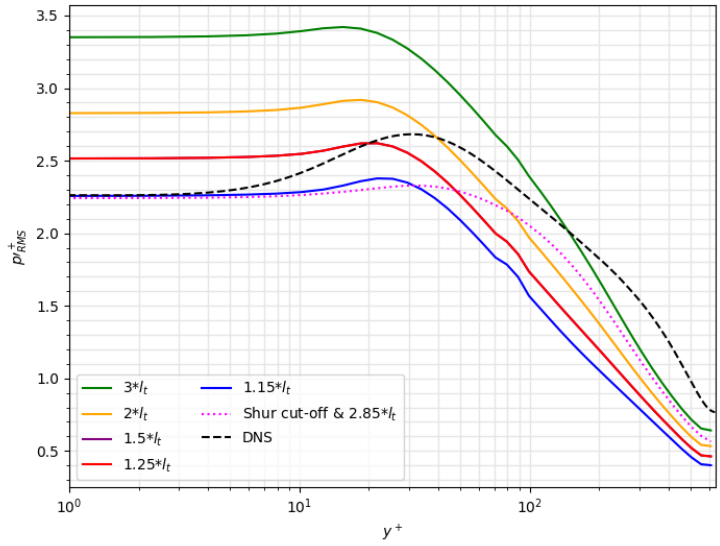

Figure 8.21: RMS pressure fluctuations along the wall-normal coordinate for different l_e definitions and C_l values, using the cubic cut-off.

To better understand the influence of the cut-off definition and of the C_l value, the focus will now be shifted towards the velocity fluctuations, more specifically the Reynolds stresses. In Figure 8.22 is depicted the Reynolds stresses for both cut-off length definitions for the standard C_l value and for the optimized one. The Reynolds stresses of the cases using the cubic cut-off show a steeper gradient close to the wall compared to the ones using Shur cut-off. Moreover, this steeper gradient is also seen in the DNS data, making the use of cubic cut-off promising. Comparing the different coefficients: for the Shur cut-off case, the change is minimal, but there is a slight decrease in overall magnitude of the Reynolds stresses; in the case of the cubic cut-off, for the optimised C_l, the $\overline{v'v'}$ component matches DNS data until around y^+ = 25.

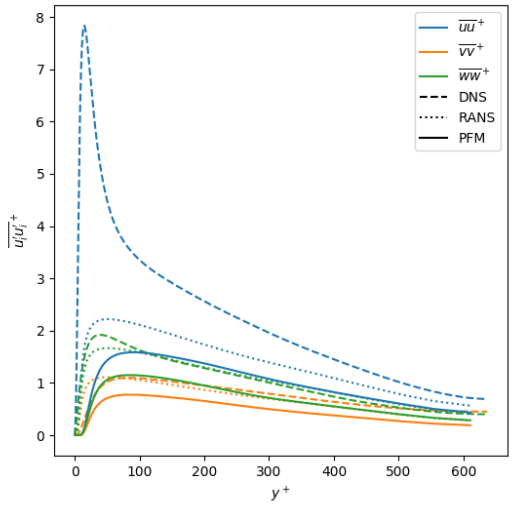

(a) Shur cut off w/ C_l = 3

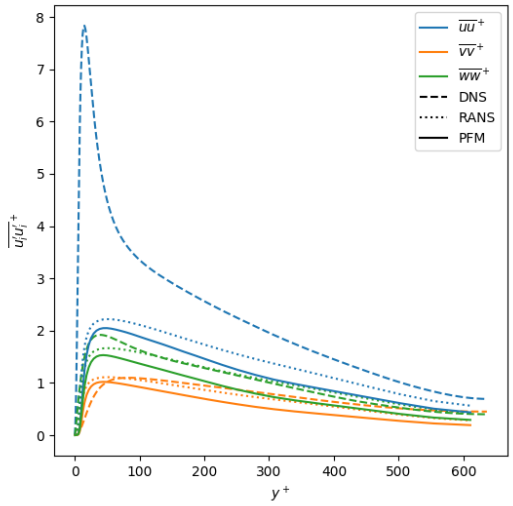

(b) Cubic cut-off w/ C_l = 3

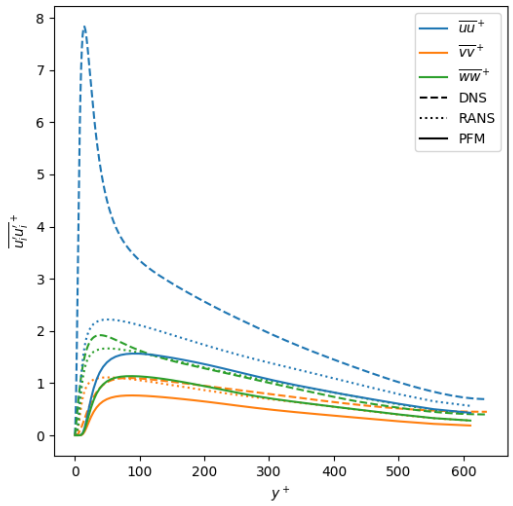

(c) Shur cut-off w/ C_l = 2.85

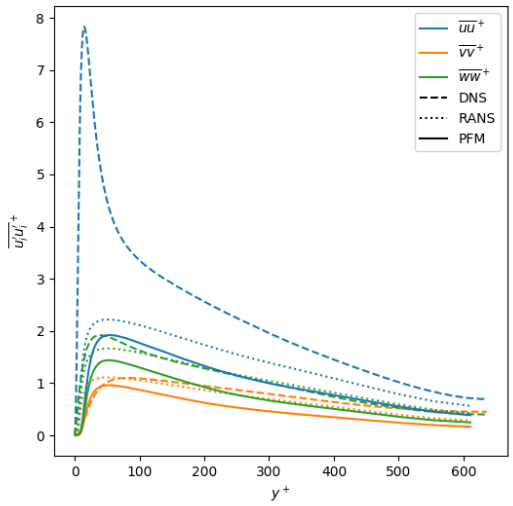

(d) Cubic cut-off w/ C_l = 1.15

Figure 8.22: Reynolds stresses for different cut off length definitions.

Until now, the different cut off methods, and their calibrated versions w.r.t C_l, have been analysed in terms of magnitude of pressure and velocity fluctuations. While this is very relevant, it is also important to understand what is the distribution of the pressure fluctuations in the spectral domain at the wall , as this is what matters the most to the application of AniPFM.

Figure 8.23 shows the angular frequency power spectra of the wall pressure fluctuations for the two cut-off length definitions and their calibrated versions. Since Abe et al. [122] had no data on the frequency spectrum, the DNS data used here for comparison is taken from Hu et al. work [125]. The experimental data is from Brungart et al. [126]. The DNS data from Hu et al. is at Re_τ = 720, while the simulations performed in this thesis are at Re_τ = 640. Moreover, the experimental data from Brungart et al. [126] was performed at Re_θ = 1120, and the simulation performed in this thesis at $Re_\theta \approx 800$. However, for this range of Reynolds numbers, it was shown that, if properly non-dimensionalised, the frequency spectra for the different Re_τ or Re_θ overlap [125].

To obtain this frequency spectra, multiple probes were place in the domain at a height equal to the

height of the center of the first cell in the y direction. These probes sample the pressure fluctuations at a constant frequency, from which then the spectra are computed and averaged over the different probes, resulting in one final spectrum. To understand the plots, one should first compare Figure 8.23a with Figure 8.23b: here the difference in energy is clear and confirms what had already been seen before, whereby for the same C_l, using the cubic cutoff results in a greater energy content compared to using Shur's cutoff. It can be noticed however that this distribution of energy is not equal for both methods though. While the spectrum of the cubic cut-off follows almost a straight line across the entire range of angular frequencies, the spectrum of the Shur cut-off shows a drop for higher frequencies. While this drop is not alike the DNS one, it is still more similar. The lack of this drop in the case of the spectrum of the cubic cut-off might have do to with aliasing: the filter is allowing for wavenumbers which are not represented by the mesh, which leads to an incorrect distribution of energy. Now comparing Figure 8.23c and Figure 8.23d with Figure 8.23a and Figure 8.23b, it is good to see that the calibration of the C_l value has an effect on all scales. Specially for the lower frequencies, the results from AniPFM are very close to DNS and experimental data, and in the case of the cubic cut-off they are even overlapped.

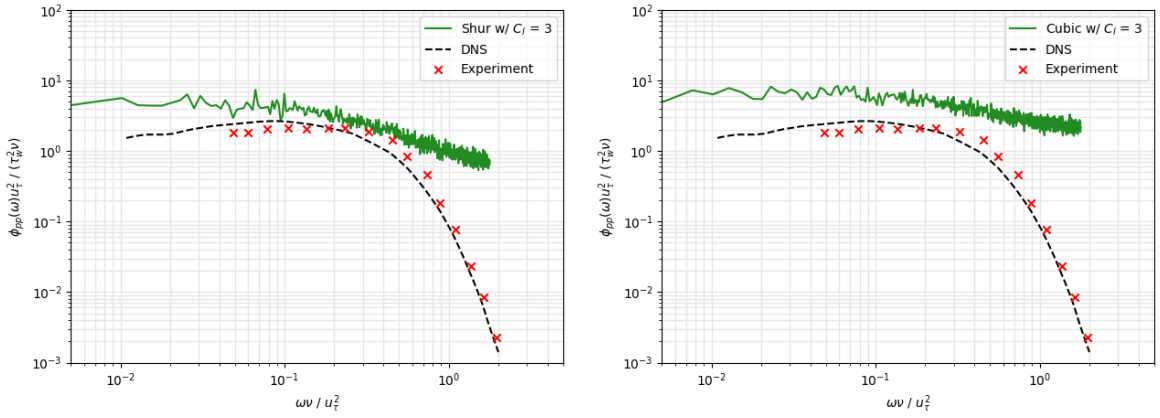

(a) Shur cut off w/ C_l = 3

(b) Cubic cut-off w/ C_l = 3

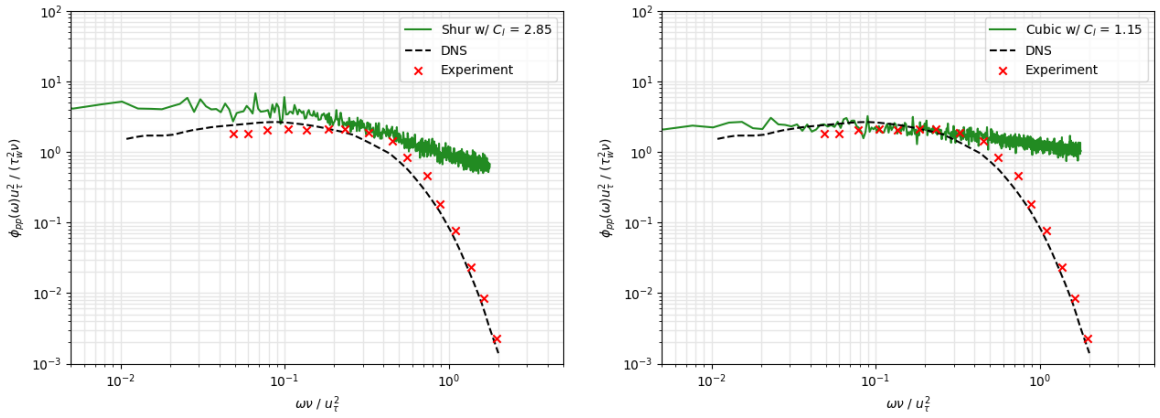

(c) Shur cut-off w/ C_l = 2.85

(d) Cubic cut-off w/ C_l = 1.15

Figure 8.23: Angular frequency power spectra of the wall pressure fluctuations.

Having analyzed the time-frequency domain, the attention is now turned to the evaluation of the wavenumber domain. Abe et al. [127] performed a DNS study of Reynolds number dependence on pressure fluctuations in TCF, in which they have data for wavenumber power spectra of pressure fluctuations at the wall for Re_τ = 640. This data will be used as comparison for AniPFM.

Figure 8.24 shows the streamwise wavenumber power spectra of the wall pressure fluctuations. The results look more spurious than expected, which might be due to the analysis being performed on the coarse grid. Nevertheless, some conclusions can be taken. Comparing Figure 8.24a with Figure 8.24b, the plots look very similar with both showing the drop in the power spectra for higher wavenumbers, that

in the frequency domain was not present in the cubic cut-off. Moreover, the cubic cut-off for the lower wavenumber shows an increase in energy of the pressure fluctuations as the wavenumber increases. This increase is more pronounced than in DNS. Figure 8.24a does not show this increase and remains roughly flat until the drop down. Comparing the calibrated versions, Figure 8.24c and Figure 8.24d, with the previous plots, it is essentially just a shift down in the overall energy across all scales, which is in line with what had been seen before.

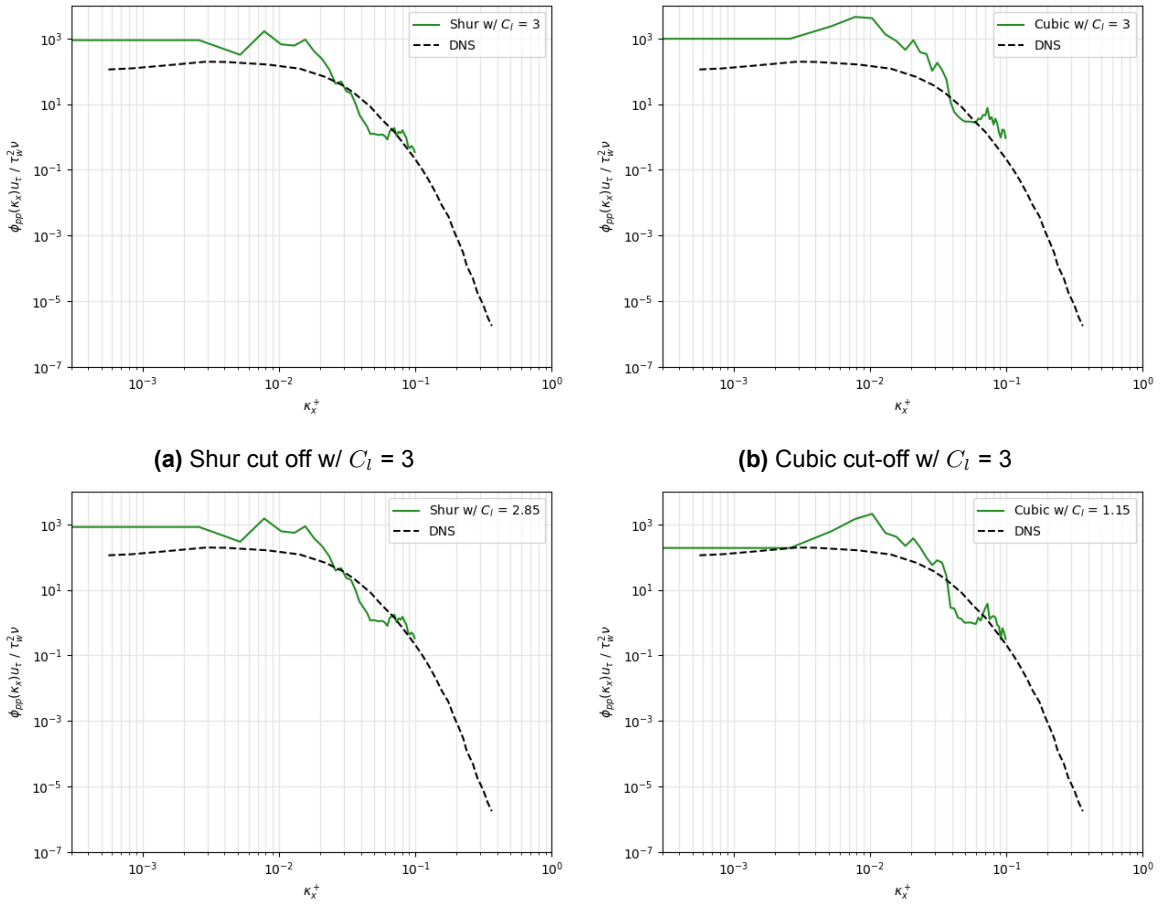

(a) Shur cut off w/ C_l = 3

(b) Cubic cut-off w/ C_l = 3

(c) Shur cut-off w/ C_l = 2.85

(d) Cubic cut-off w/ C_l = 1.15

Figure 8.24: Streamwise wavenumber power spectra of the wall pressure fluctuations.

In Figure 8.25, the spanwise wavenumber power spectra of the wall pressure fluctuations are presented. Observing Figure 8.25a and Figure 8.25b, the plots show strong similarities, with the cubic cut-off displaying higher values, consistent with previous observations. The shape of these plots closely aligns with the DNS data, though there is a notable overprediction, especially at lower wavenumbers. Turning to the calibrated versions in Figure 8.25c and Figure 8.25d, the cubic cut-off reveals a clear reduction in power spectra magnitude. However, the Shur cut-off does not show such a change, appearing much like its non-calibrated counterpart. This similarity might be attributed to the log-log scale of the plots, wherein a small change in C_l value may not result in a visually discernible difference.

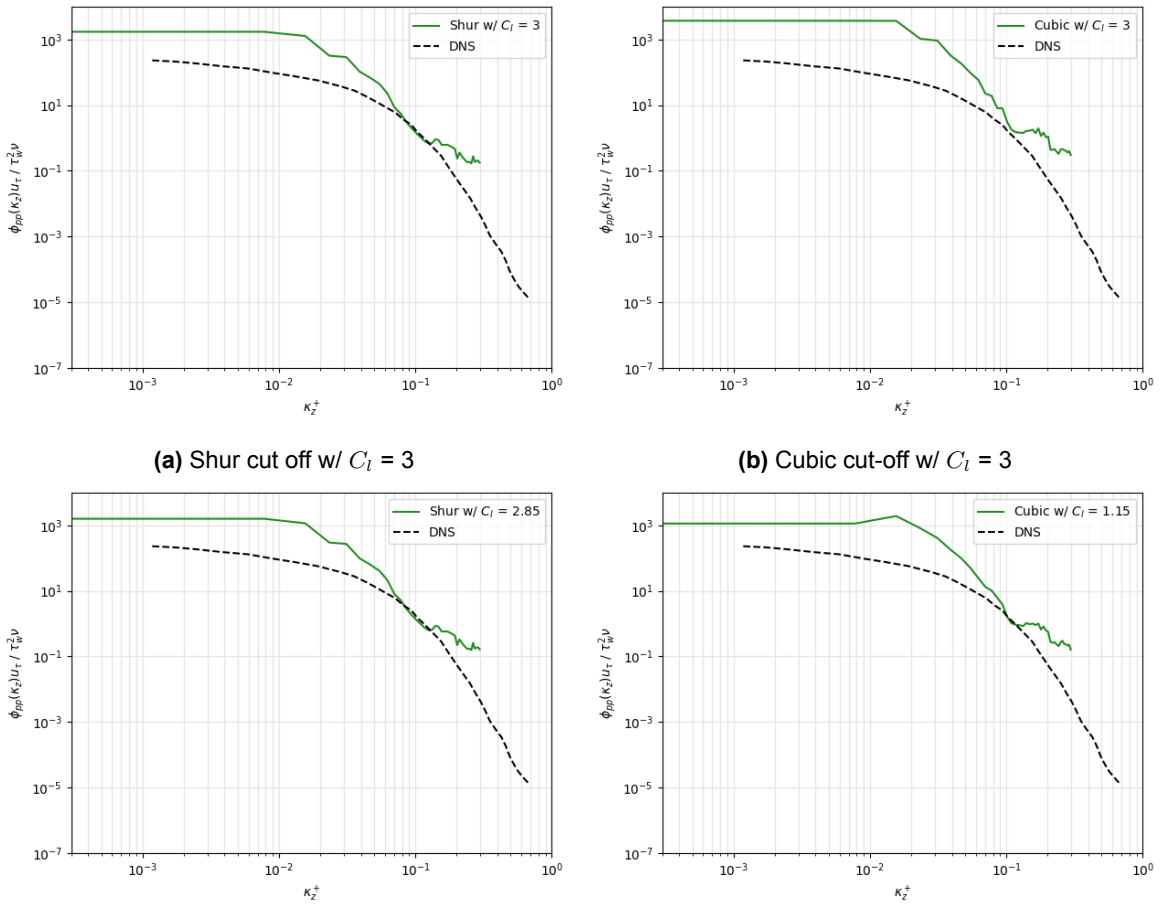

(a) Shur cut off w/ C_l = 3

(b) Cubic cut-off w/ C_l = 3

(c) Shur cut-off w/ C_l = 2.85

(d) Cubic cut-off w/ C_l = 1.15

Figure 8.25: Spanwise wavenumber power spectra of the wall pressure fluctuations.

8.7.3. Generalization

Until now in this section, it was studied the effect of the different cut-off length definitions, and it was shown for both methods that by calibrating the empirical constant in the definition of l_e, the energy of the velocity fluctuations can be calibrated allowing the pressure fluctuations magnitude to be calibrated as well. It is important to notice that the studies performed until now regarding this were done in the coarse mesh, as it allows faster computations and thus more iterations. However, from the mesh convergence study it was seen that this mesh is not considered converged. Thus, it is now important to obtain a calibrated C_l coefficient for the converged meshes. Figure 8.26 shows the RMS pressure fluctuations along the wall-normal coordinate for the different meshes. Here the Shur cut-off definition was used and C_l = 2.0. As expected a lower value for this empirical constant is needed. The same approach was applied to simulations using the cubic cut-off and a C_l = 0.6 was found as the optimal value. While these values are set for this specific flow case, it is important to check if they can be used in similar but different cases with varying flow conditions.

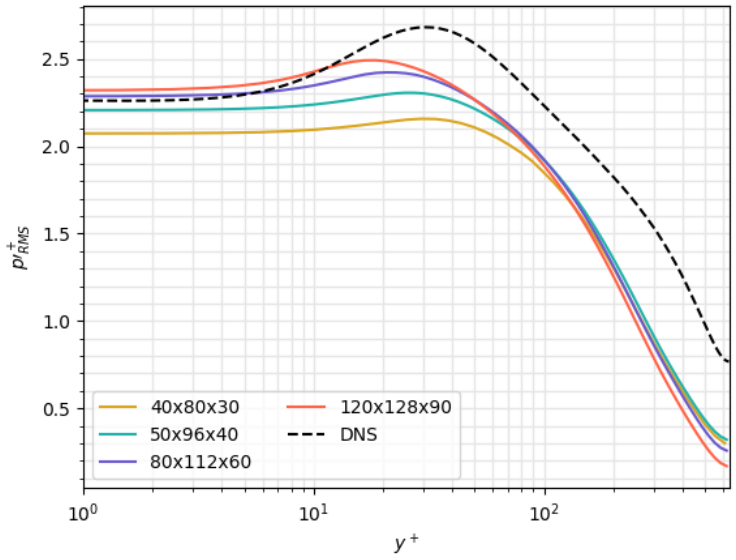

Figure 8.26: RMS pressure fluctuations along the wall-normal coordinate for various meshes, using the Shur cut-off and C_l = 2.0.

8.8. Summary

In this chapter, simulations of the turbulent channel flow at Re_τ = 640 were performed using AniPFM. An introduction was provided, highlighting the significance of TCF in the study of wall bounded turbulence. Following that, the simulation setup was detailed. Subsequently, the qualitative results were presented as a sanity check to ensure everything was running as anticipated and to offer the reader a visual demonstration of AniPFM's capabilities. Next, a mesh study was performed, ensuring the independence of future analysis from discretization errors.

In the subsequent sections, various time correlation methods for the velocity fluctuations produced by AniPFM were examined. The C&EC method emerged as more effective than the pure convection method. It displayed less reliance on user input parameters (indicating reduced uncertainty), such as the number of modes and random seed. Additionally, it showed a stronger correlation with DNS data, especially in terms of quadrant analysis and two-point correlation of near-wall turbulence. Furthermore, a calibration of the control parameter, f_τ, in the C&EC time correlation method was conducted, establishing that the range of acceptable values is 25-100. Values lower than 25 were shown to put too much weight on the convected velocity fluctuations over the newly generated ones, which leads to a more noticeable loss in energy due to numerical diffusion. Moreover, the rescaled version of the C&EC method was shown to incorrectly rescale the energy, leading to higher energy than the input (U)RANS TKE. The reason for this is not clear.

Moving forward, attempts were made to understand why AniPFM overpredicts the RMS pressure fluctuations near the wall. The governing dynamics of the pressure fluctuations were simplified for the TCF, taking advantage of its statistical homogeneity in the streamwise and spanwise directions. The simplified equation revealed that the generated pressure fluctuations exhibit significant dependence on the wall-normal component of the Reynolds stresses. While the relationship between them is not linear, it helps to understand why AniPFM was overpredicting the pressure fluctuations near the wall, despite the TKE being far from reaching DNS level, as well as the streamwise and spanwise normal components of the Reynolds stress tensor.

Once it was better understood why AniPFM was overpredicting the pressure fluctuations near the wall, solutions were sought. Through lowering the empirical constant, C_l, which is part of the expression for l_e, it was observed that it was possible to calibrate this constant to match the RMS pressure fluctuations at the wall with DNS data. It was shown that this was feasible when using any of the cutoff length definitions considered: Shur and cubic. Since the cubic cutoff leads to a higher cutoff wavenumber than Shur's, the calibrated C_l for this cutoff definition is significantly lower than the one for Shur's.

Using the cubic cutoff resulted in Reynolds stresses much closer to DNS data, proving to be a promising method. The power spectral density of the wall pressure fluctuations was then compared between the simulations using the different cutoff definitions, as well as between using the baseline and calibrated values of the C_l constant. The calibrated versions were much closer to DNS data, which further verifies the solution proposed. This solution needs to be validated later through FSI simulations. With this section studying the TKE spectrum, the influence of C_l and l_e was better understood. The effect of the cutoff was elucidated as well, but its influence is not fully grasped yet; therefore, further research on this will be carried out in the following chapter.

9 Turbulent annular flow

The analysis performed in Chapter 8 compared different methods and definitions, tested hypothesis and tried to verify them. This chapter is a continuation of the previous chapter's work, but now focusing on the turbulent annular flow. On one hand, the use of this test case can be justified by its similarity with the flow over a fuel rod. On the other hand, this test case provides extra validation data to further assess the hypothesis, assumptions and conclusions that were taken in the previous chapter. As it was seen, the TCF is statistically homogeneous in the streamwise and spanwise directions. In the case of the turbulent annular flow (for fully developed flow), it is statistically homogeneous in the orthoradial and streamwise directions. The main difference compared with TCF, is the adding of curvature. This further increases the complexity of the flow.

The chapter starts with the layout of the methodology used to tackle this case. Then, qualitative results are presented as a sanity check of AniPFM's performance. Furthermore, the quantitative results are presented, with focus on the TKE and Reynolds stresses. These results are compared with validation data. Subsequently, the time correlation methods were analysed using the two-point correlation again, but this time providing a more visual representation. Lastly, the TKE spectrum parameters cut-off length and l_e are analysed in-depth, with the aim of better understanding their influence in AniPFM.

9.1. Methodology

This case is based off the turbulent annular flow run by Norddine et al. [14]. They ran a wall resolved LES and have data such as velocity, TKE and Reynolds stresses profiles which are of great interest for the validation of AniPFM. The geometry of the setup used is shown in Figure 9.1. The shaded region represents where there is no flow. In terms of dimensions, r_o = 10.5mm is the outer radius, r_i = 5mm is the inner radius, D_h = 11mm, represents the hydraulic diameter and the length of the rod is L = 6D_h. This case was chosen as it is tailored specifically for the flow over fuel rods. Norddine et al. [14] ran this case as a precursor simulation to their LES simulation of the flow over a cantilever rod, which aims to replicate the experimental setup of Cioncolini et al. [18], who studied the flow induced vibrations of the flow over a clamped-free rod. This precursor simulation has the same geometry has the annular part of the flow in the experimental setup.

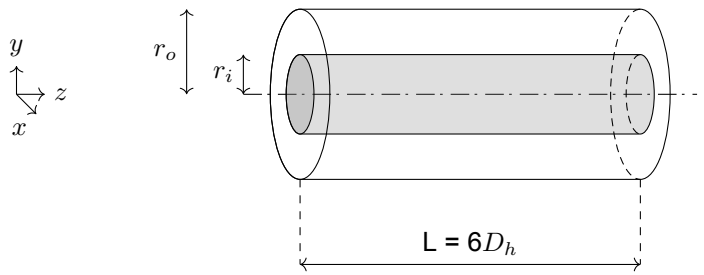

Figure 9.1: Annular cylinder domain.

The annular bulk velocity is U_b = 3.45 m/s, which leads to a Reynolds number based on the hydraulic diameter of Re_H = 4.5e4. Periodic boundary conditions are used in the inlet and outlet, whereas no slip are used in the inner and outer walls. Similarly to TCF, in order to impose a constant bulk velocity, a pressure source term is added to the momentum equation. The turbulence model used is $k-\omega$ SST. The simulations are first run as steady state until the residuals converge. The flow field from these initial simulation is used to initialise the transient simulation using AniPFM. The numerical solvers setup is the same as the one used in TCF. Furthermore, the max CFL number is constrained at 1.0. The AniPFM simulation are run for 2 seconds, which is equivalent to roughly 100 flow passes through the domain. For the quantitative results, the flowfield is then averaged in space in the streamwise and orthoradial directions, as well as in time for the last 10 flow-throughs. The settings used in AniPFM in the different sections are summarized in Table 9.1.

Table 9.1: Summary of AniPFM parameters used in each section/subsection

(Sub)section	#modes	Rand. seed	Time corr.	f_τ	l_e	C_l	Cut-off
section 9.2	256	Default (0)	C&EC	25	$C_l l_t$	3.0	Shur
section 9.3			C&EC	25			Shur
section 9.4			C&EC, PC	Various			Shur
subsection 9.5.1			C&EC	25			Both
subsection 9.5.2			C&EC	25			Shur

Three different meshes were considered. The resolution of these different meshes is shown in Table 9.2 and a cross section of each can be visualised in Figure 9.2.

Table 9.2: Annular flow mesh resolutions

Mesh	N_r	N_θ	N_z	N_{cells}	r^+_{avg}
Coarse	24	20	30	57,600	2
Medium	36	30	54	233,280	0.85
Fine	50	40	60	480,000	0.6

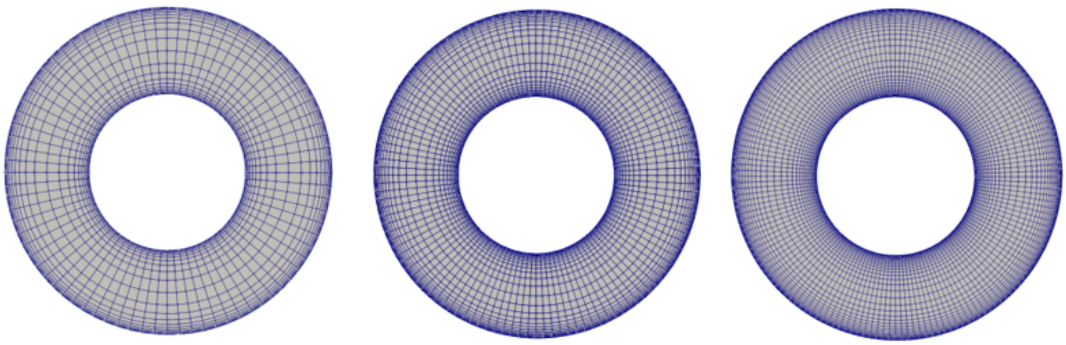

(a) Coarse **(b)** Medium **(c)** Fine

Figure 9.2: Turbulent annular flow meshes.

9.2. Qualitative results

To better understand the flow and also as a sanity check of AniPFM to see if everything is working as expected, qualitative results are key. Figure 9.3 shows the instantaneous velocity and pressure fluctuations at a slice in the middle of the channel. Once again the values from the velocity fluctuations look spurious, but upon closer look it can be seen that most of the higher magnitude fluctuations are located close to the wall. In the pressure fluctuations plot this can be even better seen.

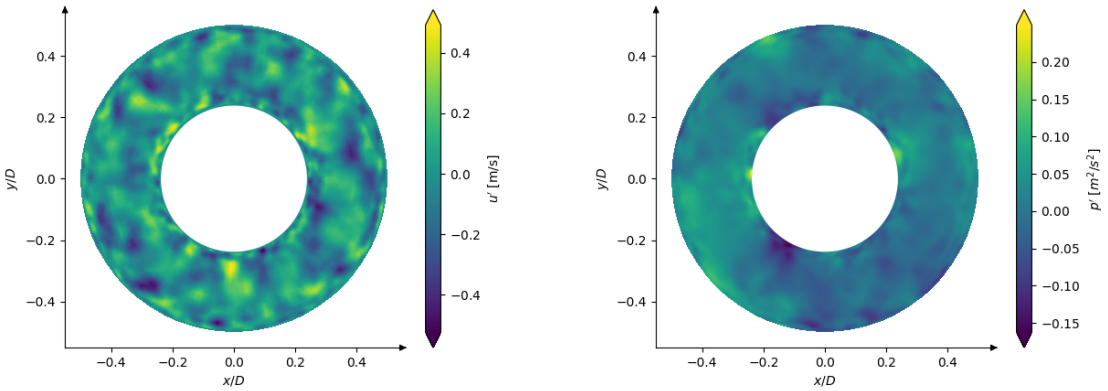

(a) Velocity fluctuations **(b)** Pressure fluctuations

Figure 9.3: Instantaneous velocity and pressure fluctuations at a slice in the middle of the channel.

While the instantaneous fluctuations seem to be what one would expect from AniPFM, it is really hard to actually take any conclusions or to fully check if everything is working as it should. This is why it is necessary to also look at the mean squared velocity and pressure fluctuations. These are shown in Figure 9.4 for a slice in the middle of the channel. The figure is very similar to the one seen for TCF, with higher values of the mean squared fluctuations close to the wall and lower closer to the center of the channel. Taking the mean square of the fluctuations also helps in visualizing the statistical homogeneity in the orthoradial direction that was mentioned earlier.

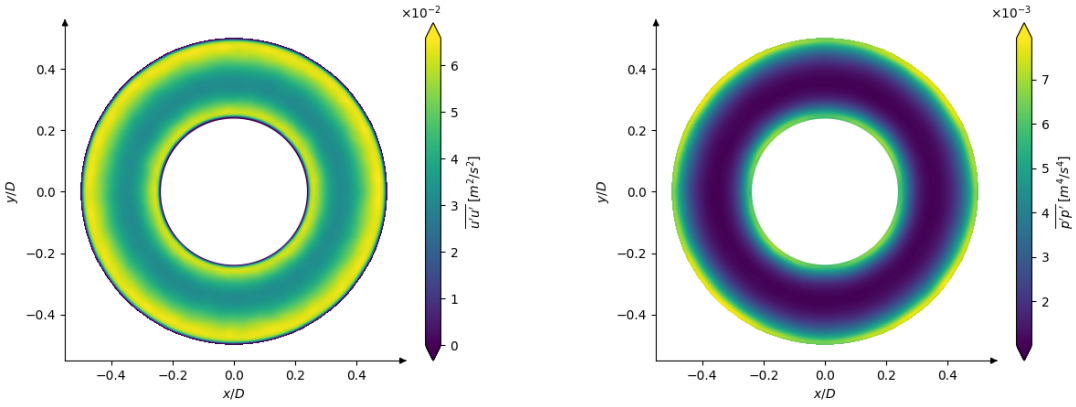

(a) Mean squared velocity fluctuations **(b)** Mean squared pressure fluctuations

Figure 9.4: Mean squared velocity and pressure fluctuations at a streamwise normal plane in the middle of the channel.

Lastly, Figure 9.5 depicts the instantaneous velocity fluctuations in a slice along the streamwise direction. This figure aims at giving the reader a further grasp of how AniPFM synthetic velocity fluctuations look like at a given instant.

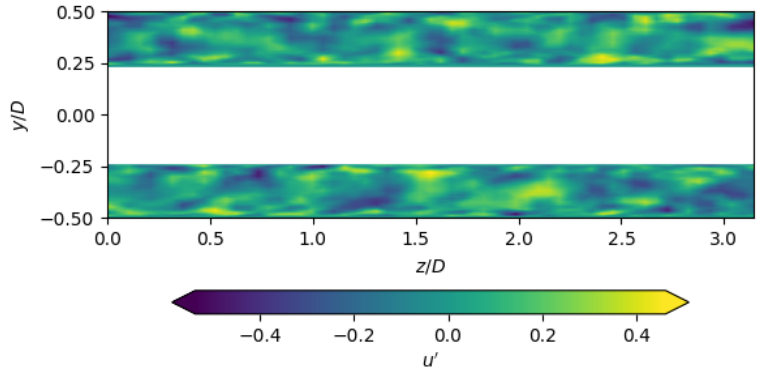

Figure 9.5: Instantaneous velocity fluctuations in a slice along the streamwise direction.

9.3. Quantitative results

In this subsection, a detailed analysis will be conducted on quantitative results obtained from the simulations with the different meshes performed with AniPFM. These findings will be compared with data sourced from the research of Norddine et al. [14]. This is what is showed in Figure 9.6, where the streamwise velocity, TKE, and normal Reynolds stresses profiles are shown along the wall normal coordinate. The results presented here were obtained using Shur's cut-off length definition and with the default C_l value. Looking at all the plots in general, it is clear that there is a convergence of the profiles as the mesh resolution increases, with the medium mesh already providing almost the same results as the fine mesh with about half its amount of cells.

Going into the specific plots now, the streamwise velocity profile, shown in Figure 9.6a, is in agreement with the LES data. This is not really relevant for the validation of AniPFM, as this is purely based on the input RANS information, but still it is a good sanity check. Moving onto the more interesting results, in Figure 9.6b, is shown the TKE profile. Near the walls, the TKE is underpredicted compared to the LES data. This is in agreement with the comparisons with DNS data seen in the previous chapter. Moreover, near the middle of the channel the TKE is overpredicted. Analysing the streamwise normal Reynolds stress component, shown in Figure 9.6c, the profile shape resembles the one seen in the TKE. The very low values of this component near the wall when compared with high fidelity data are also in agreement with the findings from the previous chapter.

Lastly, Figure 9.6d shows the wall normal component of the RST. This is a very important component when it comes to the generation of pressure fluctuations as it was shown in section 8.6. The equation for the pressure fluctuations in the case of the annular flow is the same as the one shown for the TCF (assuming streamwise and orthoradial statistical homogeneity) with the difference that instead of considering cartesian coordinates, one would consider cylindrical coordinates. From analysing Figure 9.6d, it an be said that AniPFM is in good agreement with the LES data. For the most important part, which is close to the inner wall (left part of the plot), for the finer meshes, AniPFM is very close to matching the validation data, just slightly underpredicting. Furthermore, for the middle of the channel, AniPFM is predicting higher values than LES data. This was also seen in the streamwise component of the RST as well as in the TKE. This will be analysed later on the chapter.

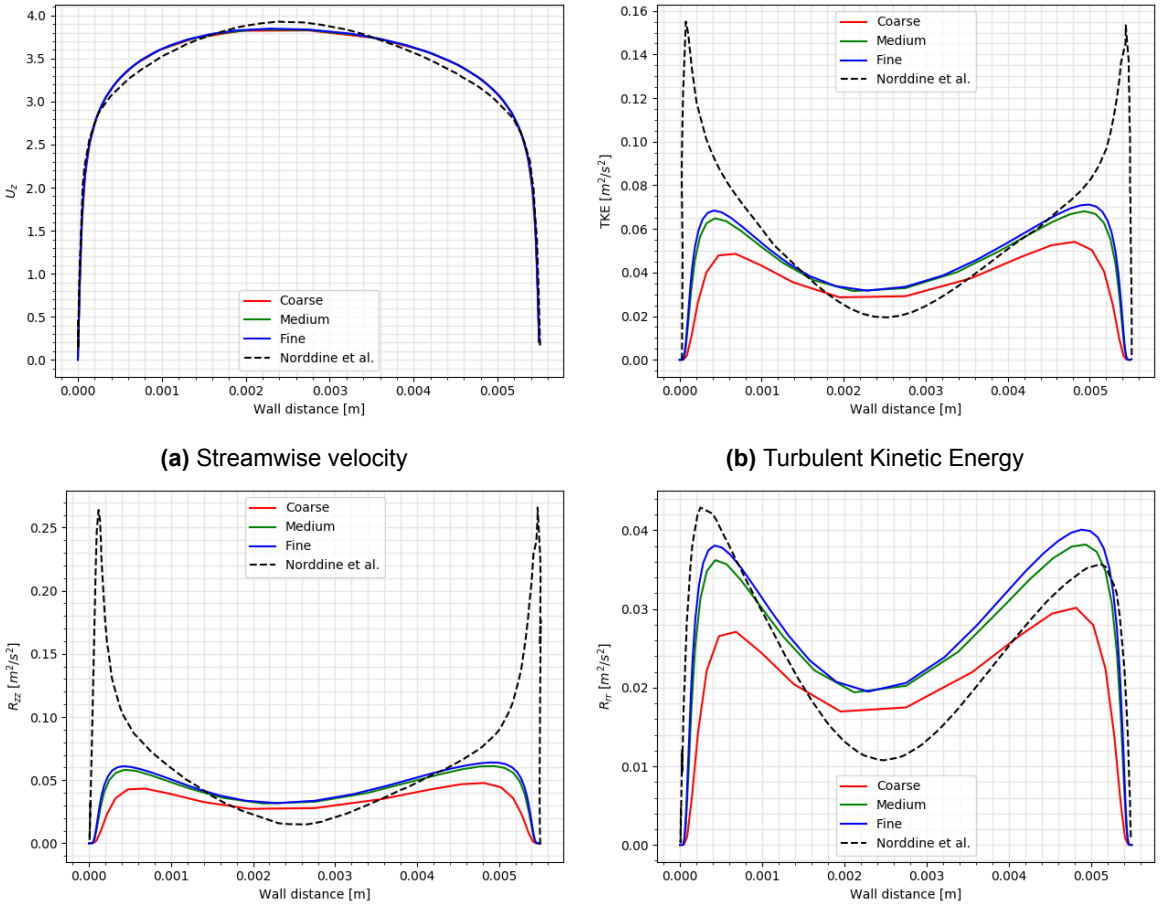

(a) Streamwise velocity

(b) Turbulent Kinetic Energy

(c) Streamwise RST component

(d) Wall normal RST component

Figure 9.6: Comparison of quantitative results with the ones from Norddine et al. [14].

9.4. Time Correlation

In the previous chapter, an extensive analysis was made comparing pure convection and C&EC time correlation methods. Additionally, the fine-tuning parameter, f_τ, of the C&EC method was also studied. In the previous chapter the two point correlation was always visualized as a line. The work presented in this subsection is complementary to the study performed in the previous chapter, as it is regarding a different case and also because it provides a more visual representation of the two-point correlation. Figure 9.7 shows the two-point correlation of the streamwise velocity fluctuations for different time correlations in a cross section along the z direction. The inlet section is taken as the baseline as it can be seen in the figure by the value of 1.0. The correlations have been averaged in time and in space in the orthoradial direction.

First, looking at the pure convection, one can see streaks of stronger correlation or decorrelation that are present from the inner to the outer wall with a very similar behaviour at different streamwise positions but smearing down as the middle of the channel is approached. This behaviour can to a certain extent also be seen in C&EC with $f\tau$ = 1, as this case is the closer one to pure convection. However, as f_τ is increased the streaks stop dominating the two-point correlation and it starts looking more spurious, which is a result of the decorrelation and formation of new turbulent structures. In the case of the pure convection, the same turbulent structures are simply convected (frozen turbulence), resulting in the more streaky appearance of the two-point correlation. Moreover, as expected, the high correlation region near the inlet increases with a decrease of the correlation factor for the C&EC cases.

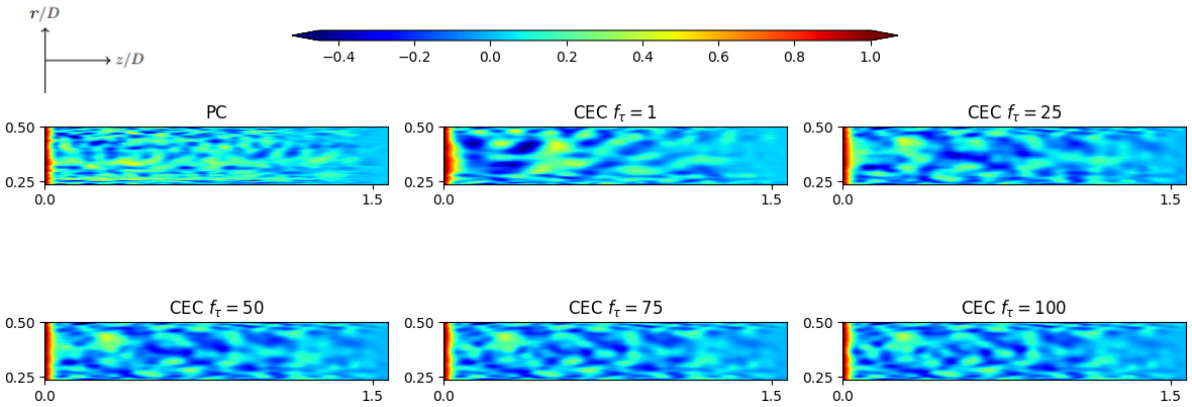

Figure 9.7: Two-point correlation of the streamwise component of the velocity fluctuations for different time correlation methods.

9.5. TKE spectrum

The turbulence kinetic energy spectrum parameters analysed in Chapter 8 - the length scale associated with the energy peak of the spectrum, l_e, and the cut-off length scale, l_{cut} - are once again analysed here. Emphasis is placed on their impact on the turbulence statistics relevant to AniPFM. Additionally, efforts are made to gain a deeper understanding of their influence, not just by examining AniPFM's results, but also by analyzing the distribution of these length scales throughout the domain.

9.5.1. Cut-off wavenumber

In Figure 9.8 is displayed the cut-off wavenumber w.r.t the wall normal direction for its different definitions. Upon comparing the plots, it becomes evident why earlier findings indicated that the cubic cut-off results in higher magnitude velocity fluctuations than the Shur cut-off. The cut-off wavenumber predicted by the cubic method is consistently higher than that predicted by Shur's across the entire domain.

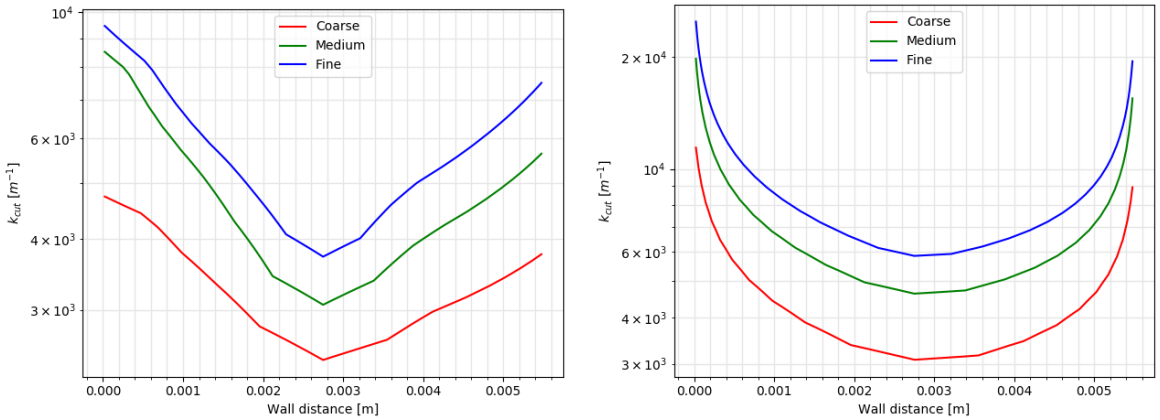

(a) Shur cut-off

(b) Cubic cut-off

Figure 9.8: Cut-off wavenumber for different definitions.

As it was mentioned before, in Figure 9.6 were shown the quantitative results for the simulation run with Shur's cut-off. In Figure 9.9 these are shown for simulation with the cubic cut-off. Looking at Figure 9.9a, it is very interesting to see that the TKE near the wall is much greater than the one in Figure 9.6b, while near the middle of the channel it is pretty much the same. This is exactly the kind of behaviour wanted. The TKE profile becomes much closer (although still far away obviously) from the LES one. Furthermore, the gradient of the TKE profile near the wall is extremely close to the one of LES for the finer meshes using AniPFM and cubic cut-off, while using Shur's cut-off the gradient fails

to match LES data. Furthermore, the same differences seen in the TKE can be seen in the streamwise RST component, as it can be seen in Figure 9.9b. Lastly, looking at the wall normal RST component, Figure 9.9c, it can be observed that AniPFM's profile almost matches LES data, at least for the inner wall region. The results show great promise in using the cubic cut-off with AniPFM, provided that the model is well calibrated for using this cut-off in terms of TKE.

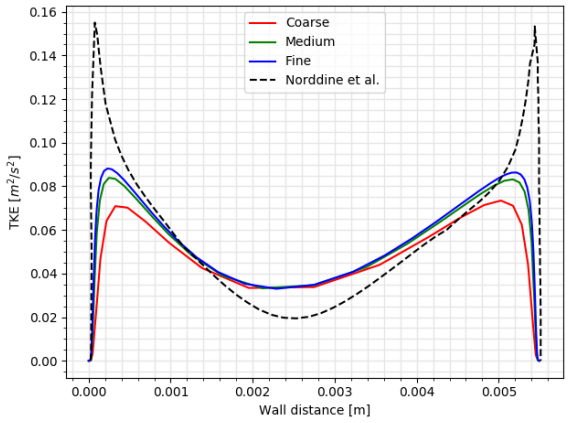

(a) Turbulent Kinetic Energy

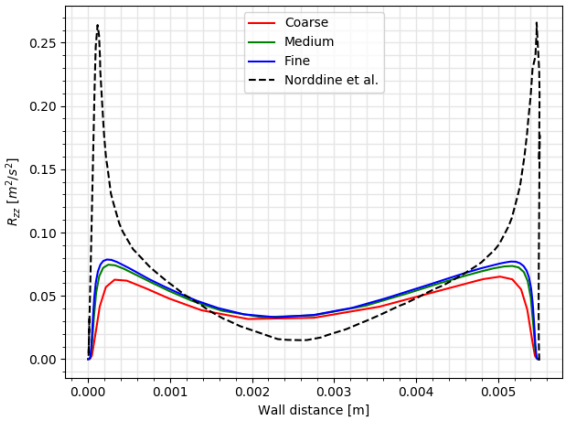

(b) Streamwise RST component

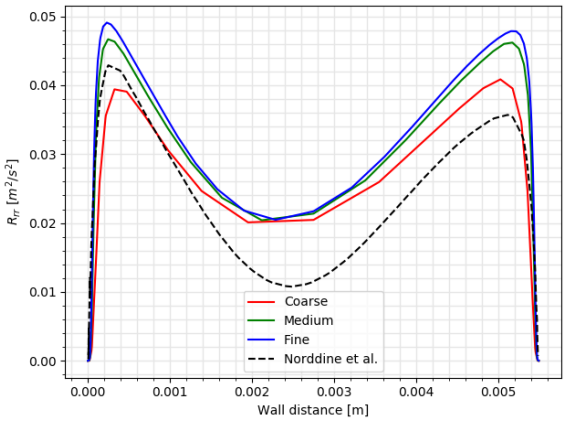

(c) Wall normal RST component

Figure 9.9: Comparison of quantitative results using the cubic cut-off filter with the ones from Norddine et al. [14].

9.5.2. TKE peak wavenumber

In this subsection the focus will be shifted to the definition of l_e. In Figure 9.10 is shown the distribution of l_e w.r.t the wall distance. Both quantities are non-dimensionalised by the hydraulic radius. The definition used was l_e = 3l_t. The figure, as expected, resembles the analogous line in Figure 7.1 by Shur et al [10], as both are wall bounded channel flows.

From the figure, it can be observed that the lengths scale in question predicted by this definition is up to 2.2 times the max possible length scale geometrically (r_H). This happens for most of the channel, with length scales already at the maximum geometrically at a distance of 0.2r_H the wall. At first, this overprediction was thought to be the possible reason why AniPFM was showing TKE and RST values higher than LES data for the middle of the channel. Upon deeper study, this thought was proved to be incorrect. In Figure 9.10, it is also shown a line for l_{start}. This length scale is associated with k_{start}, which is the starting wave number for the energy spectrum. This wavenumber is defined as shown in Equation 7.19. Inside the minimization function in this expression is k_{start*}, which is defined by Equation 7.17, and 0.5k_e. A thorough analysis of the distribution of the values of these expression throughout the domain for the different simulations, showed that this definition of k_{start*} results in very low wavenumbers, which means that it always gives unphysical starting length scales.

This results in the minimization function to result always in k_{start*}. This is not a problem however, because $2\pi/l_{user}$ is always higher than k_{start*}, thus k_{start} is equal to the max geometrical length scale always. Consequently, this means that if l_e is more than the maximum geometrical length scale, it does not have any effect as the wavenumber is k_e is lower than the starting wavenumber and hence not represented by it. So what happens in reality is that the distribution of l_e in the channel looks like the one showed in Figure 9.11.

The overprediction of AniPFM of the TKE in the middle of the channel is not due to the definition of l_e then. But why does it happen then? It is actually due to the RANS input. Van den Bos et al. [34] studied the effect of the turbulence model used in the RANS input of AniPFM, mainly the turbulence models $k-\epsilon$ and $k-\omega$ SST. Examining their studies, it can be observed that $k-\omega$ SST slightly overpredicts the TKE near the middle of the channel compared to DNS data. While the $k-\epsilon$ model does not, it has less accurate near wall performance than the $k-\omega$ SST, when compared with DNS data.

Lastly, it should be noted that the definition of k_{start*} is not suitable and should be revised. As it was seen, this is the cause why k_{start} = $2\pi/l_{user}$. While at first this does not seem problematic, it turns out to be depending on the flow case being analysed. In the case of flows where the maximum geometrical physical length scale is always the same (constant cross section area flows - e.g.: annular flow, TCF), this definition is representative. However, for cases where the cross section area where there is flow is not always the same, as for example the cantilever rod with incoming axial flow that will be discussed in Chapter 11, it is clear that this definition is not representative. In the area where there is no beam this length scale would be higher that in the area where there is a beam (essentially annular flow in this region). To conclude, further study is necessary to find a more suitable expression for the starting wavenumber.

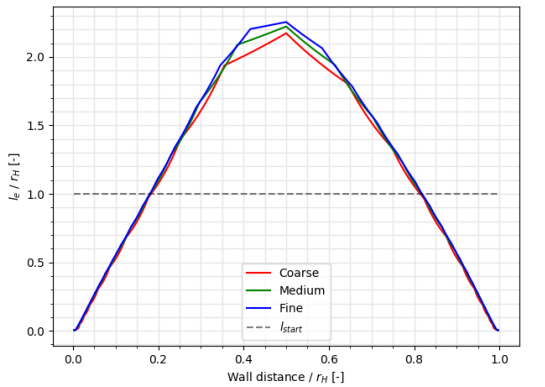

Figure 9.10: Distribution of l_e w.r.t the wall distance.

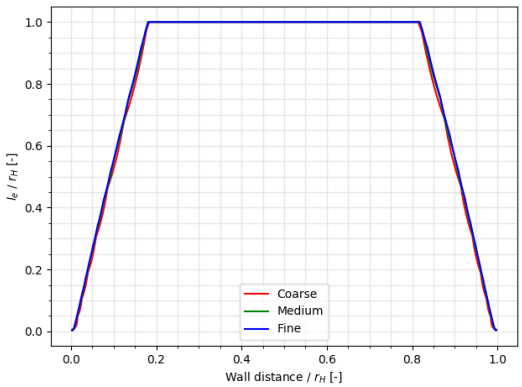

Figure 9.11: Real distribution of l_e w.r.t the wall distance.

9.6. Summary

In this chapter, turbulent annular flow was analysed using AniPFM and compared with high-fidelity data from LES. The methodology was presented, alongside qualitative and quantitative results. The quantitative results focused around turbulence statistics. These showed good correlation with validation data is terms of the wall normal component of the Reynolds stresses, but not so much in terms of the streamwise component or the TKE. Using the cubic cut-off shows more TKE near the wall, which leads to better matching Reynolds stresses with LES data. This method shows good promise, but in conjunction with calibration of the length scale associated with the TKE peak, so that it does not overpredict the energy near the wall. Additionally, the behaviour of the cut-off filter along the channel was analysed, helping further understand its effect on AniPFM. Moreover, the two-point correlation was discussed for different time correlation methods. A visual representation was shown, allowing for a better understanding of the effect of the time correlation on the behaviour of the generated turbulence along the channel. Lastly, the distribution of l_e along the channel was analysed, exposing flaws in the definition of k_{start}.

10

Brass beam in turbulent axial water flow

Until now, the discussion of AniPFM has revolved around fluid only simulations. The ultimate goal of AniPFM is to be integrated into an FSI framework to simulate TIV in nuclear fuel rods. Thus, it is of the upmost importance to perform FSI simulations. In this chapter, the first FSI case is presented: a flexible brass beam in turbulent axial water flow. This case was chosen due to the amount of comparison data available from other numerical simulations, as well as the experimental data it is based on, and because of its simplicity.

The chapter is structured into three main sections. The initial section focuses on the simulation setup, breaking it down into the experiment and previous numerical setups, as well as the current setup. The following section presents the results and is further divided into examining time correlation, the calibrated model, and a comparison with other numerical approaches. The concluding section addresses the question of trying to understand which wavenumbers contribute most to the vibrations, with the end goal of more affordable simulations.

10.1. Simulation setup

In this section, the experiment of Chen & Wambsganss [15] of a flexible brass beam is presented alongside numerical setups replicating it. Moreover, the numerical setup used in this thesis, based on the one used by van den Bos et al. [34], is also presented.

10.1.1. Experiment and previous numerical setups

Chen & Wambsganss [15] conducted an experiment with a flexible brass beam in turbulent water, which has become a benchmark for many FSI studies concerning nuclear fuel rods [17, 32, 34, 128]. This experiment's appeal lies in its straightforward design and the provision of data on modal frequencies and root-mean-squared vibration amplitudes for different flow conditions. A sketch of the numerical replication of this experiment can be seen in Figure 10.1. The beam is clamped on both sides. In terms of dimensions, it has a diameter of D_i = 0.0127m, while the enclosing cylinder has a diameter of D_o = 0.0254m, and the beam has a length of L = 1.19m, resulting in an L/D ratio of 93.7. The turbulent intensity and length scale at the inlet were unspecified by Chen & Wambsganss [15], leading subsequent researchers to make assumptions [17, 32, 34, 128]. They assumed a turbulence intensity of 5% and a turbulent length scale of 0.1 cm and for this reason in this thesis the same parameters will be used. The experiment was conducted with various mean inlet velocities, ranging from 8-33 m/s, resulting in Reynolds numbers between 101,600-419,100. The rod has a density of 8400 kg/m^3 which gives a density ratio of ρ_s/ρ_l = 8.4. The Poisson ratio was not specified in the experiment, but a nominal value of 0.33 was used based on earlier simulations [17]. Lastly, a Young's modulus of E = 107 GPa was specified [15].

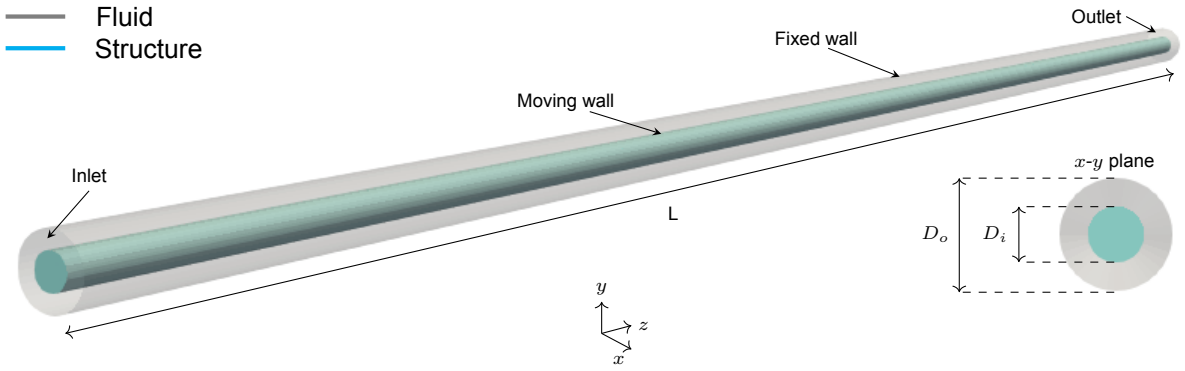

Figure 10.1: Fluid and solid domains.

As it was mentioned before, this experiment has been replicated numerically by many researchers. De Ridder et al. [32] used FSI simulations with an initial displacement of the beam to calculate the natural frequency of the fundamental mode. They solved fluid dynamics using a URANS $k-\omega$ SST turbulence model and structural mechanics using a commercial finite element solver, Abaqus. The IQN-ILS method was used to couple the solvers. The simulations were conducted at speeds of 10-30 m/s. Modal frequencies were calculated for all three flow cases, with and without pre-stress. Furthermore, De Ridder et al. [16] also performed wall resolved LES simulations without FSI. In order to reduced the computational cost, the rod was not simulated at its full length, instead a smaller rod was used with a length/diameter ratio of 10. For this case, the mesh used had 76.8 million cells. Extrapolating this for a full length rod, it would yield roughly 720 million cells just for the fluid side.

Kottapalli et al. [17] used a similar FSI approach to De Ridder et al. [32], but also simulated the rod without initial displacement using a pressure fluctuation model (PFM, predecessor of AniPFM).

Nazari et al. [128] also used FSI simulation with URANS and LES models for fluid dynamics and a finite element solver for structural mechanics, but the coupling method is unclear. The $k-\omega$ SST turbulence model was used for URANS, and the Dynamic Smagorinsky-Lilly model was used for LES.

Van den Bos et al. [34] ran simulations replicating this experimental setup for pure AniPFM simulation, URANS FSI simulation (using $k-\omega$ SST turbulence model) and AniPFM FSI simulations.

10.1.2. Current setup

The current setup is the same used by van den Bos et al. [34], which in turn made their setup in a way to be similar to the other numerical approaches before, as to ensure a more fair comparison. The same assumptions are taken. At the inlet, 5% turbulence intensity and 0.1 cm turbulent length scale are used. The effect of these settings were studied by De Ridder et al. [32] and showed to have minimal impact on the results of URANS based simulations. Additionally, a uniform inlet velocity is used, which is in agreement with previous researchers [17, 32, 34, 128]. Van den Bos et al. showed that this assumption has no effect on the prediction of the natural frequency, but has a 3% effect on the damping ratio. Nevertheless, this assumption is taken in this thesis to ensure a fairer comparison between the different approaches.

The fluid and solid domains are shown in Figure 10.1. The inner beam is modeled as elastic whereas the outer cylinder is fixed. The structural solver used is based on linear elasticity. This is possible to do if the relative displacements are much smaller that one (A_{rms}/L $\ll 1$), which is the case. The coordinate system used is the one shown in the figure. In terms of the fluid side, URANS with the turbulence model $k-\omega$ SST is used. The fluid meshes are all wall resolved. Van den Bos et al. [34] performed mesh studies showing that 40 elements in the tangential direction are enough to get converged results. The mesh discretization in the radial direction is chosen as to ensure a wall resolved mesh (r^+ = 1.05) and in the axial direction it is changed to analyse the effect on the results. The same structural mesh from van den Bos et al. is used here as well. They performed a mesh convergence study to ensure independence of the results on the mesh. In Figure 10.2 are shown the fluid and solid meshes. Regarding time marching schemes, second order methods are used for both fluid and structural solvers.

Van den Bos et al. employed an implicit coupling scheme, IQN-ILS, due to the low density ratio. For mesh mapping, they opted for local radial basis functions. This approach was chosen over global

radial basis functions to reduce computational effort while achieving comparable FSI results. The same settings are used in the current thesis.

In order to run the FSI simulations, first steady state fluid only simulations are run. These are stopped when the residuals are converged, after which, the flowfield is used to initialize an unsteady simulation (fluid only also) using AniPFM, which is run for 10 seconds (roughly 84 flow passes through the domain). This simulation is in turn used to initialize the domain of the fluid part of the FSI simulation, which are run for 10 seconds or until the RMS of the displacements are considered converged.

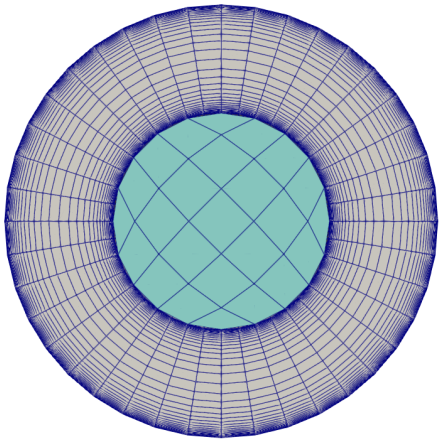

Figure 10.2: Fluid and solid meshes.

10.2. Results

In this section, the results of the FSI simulations are presented. The time correlation methods pure convection and C&EC are compared now in terms of FSI related quantities, such as amplitude of vibrations, for example. Moreover, the study on the different cut-off length definitions and their calibrated versions is continued, with the aim of validating and deepening the analysis done with just flow cases. Lastly, a comparison is made between the current calibrated version of AniPFM and other researchers work of this same case.

No initial force is applied on the beam, all displacements are purely due to the pressure fluctuations generated by AniPFM. In terms of AniPFM user input settings that are kept constant throughout the simulations: 256 modes are used for the Fourier series decomposition and the maximum wave length is equal to hydraulic radius. Concerning BCs, for the pressure fluctuations, zero gradient BCs are used for the inner and outer walls, whereas for the inlet and outlet Equation 7.36 is used. For the velocity fluctuations, no slip BC is imposed in the inner and outer walls and a mapped BC is used for the inlet and outlet. When not mentioned, the used mesh is 50x40x300. A summary of AniPFM's parameters used in each section of this chapter is presented in Table 10.1.

Table 10.1: Summary of AniPFM parameters used in each section/subsection

(Sub)section	#modes	Rand. seed	Time corr.	f_τ	l_e	C_l	Cut-off
subsection 10.2.1	256	Default (0)	C&EC, PC	25	$C_l l_t$	3.0	Shur
subsection 10.2.2		Default (0)	C&EC			2.0 & 0.6	Both
subsection 10.2.3		Various	C&EC			0.6	Shur
section 10.3		Default (0)	C&EC			3.0	Shur

10.2.1. Time correlation

In this subsection, the pure convection and C&EC time correlation methods are compared. Previously, van den Bos et al. [34] already did some analysis regarding the differences between these methods in FSI simulations, but mostly analysed power spectral densities, such as the one of pressure fluctuations or the amplitude of vibrations. They exhibited similar results in these quantities. The first goal with the

research presented here is go more in-depth and understand what is the actual effect the methods have on how the vibrations, avoiding looking at statistics such as the RMS, which may hinder some interesting characteristics. The second goal is to assess the uncertainty inherit to each method and quantify it.

The simulations were run with the same mesh (50x40x300). The C&EC used a correlation factor f_τ = 25. This was chosen as in the previous chapters it was seen that there was not much difference between f_τ = 25-100. The time step used for pure convection is Δt = 2.(6)e-4, whereas for C&EC, a more conservative time step has to be taken to ensure convergence, Δt = 2e-4. This difference in time step leads to a slightly longer simulation when using the latter time correlation method.

To start off the comparison between the methods, in Figure 10.3 are displayed the displacements of the center of the beam in the x and y direction with respect to time. Looking at the results from the simulation using PC, Figure 10.3a, it can be noticed the difference between the amplitude of displacements in the x and y directions, where the latter shows much higher displacements (reaching 5x the displacement in the x direction sometimes) throughout the whole time series. This difference is unphysical. There is no physical reason why there should be a difference in the displacements in each direction. This difference is hypothesized to be due the inherit nature of the method, whereby if a velocity field which leads to stronger pressure fluctuations in the top and bottom regions of the inner wall is generated, then this velocity field is simply convected throughout the whole domain, resulting in a similar behaviour throughout the whole time series. On the other hand, looking at the results from the simulation using C&EC method, Figure 10.3b, this behaviour is not seen. Instead the displacements in the different directions are balanced out, resulting in more physically reasonable vibrations.

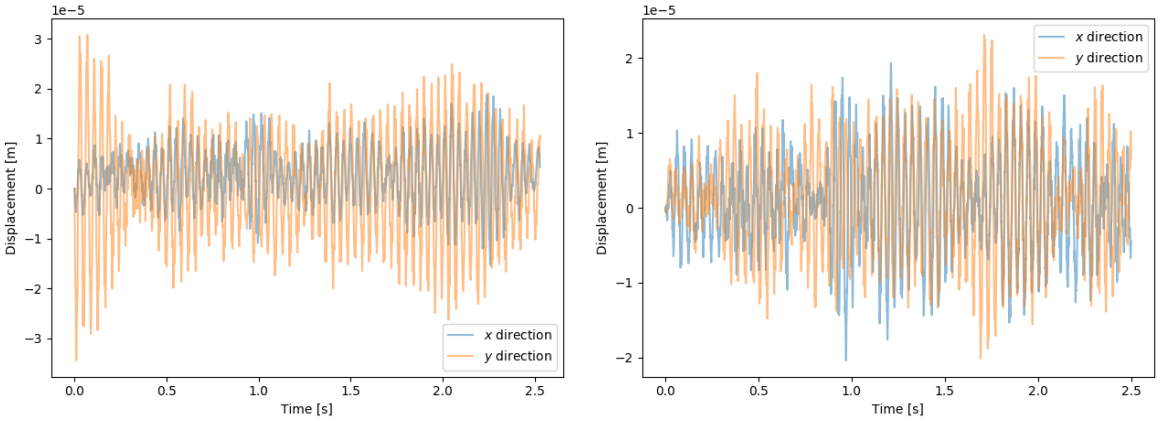

(a) Pure convection

(b) Convection & exponential correlation

Figure 10.3: Displacement in the x and y directions in the center of the beam for different time correlation methods.

The variations in x and y displacements are clearly depicted in Figure 10.4, which showcases the center-of-beam displacement for the two time correlation methods. This illustration provides a more visual representation of the points discussed earlier. For a more comprehensive understanding, the 3D representation of the displacements with respect to time can be found in Figure 10.5.

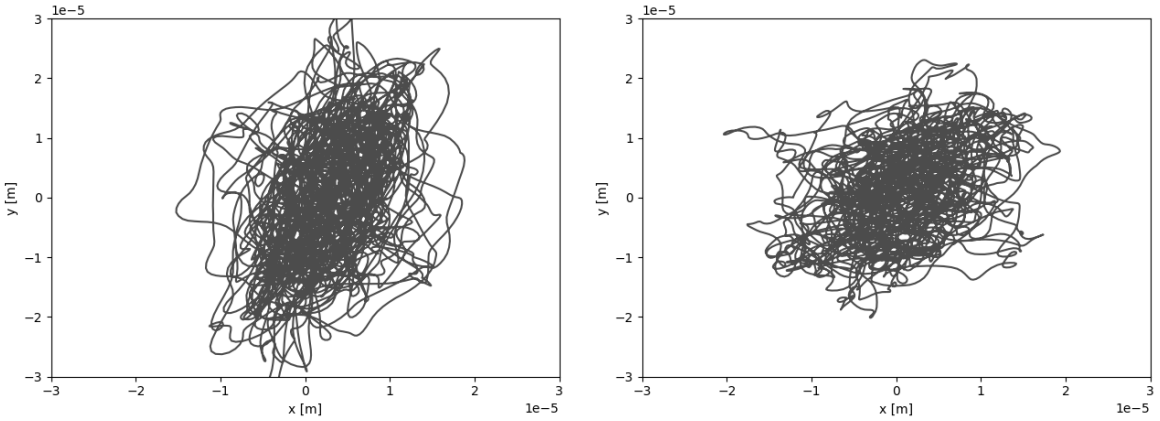

(a) Pure convection **(b)** Convection & exponential correlation

Figure 10.4: Front displacement in the center of the beam for different time correlation methods.

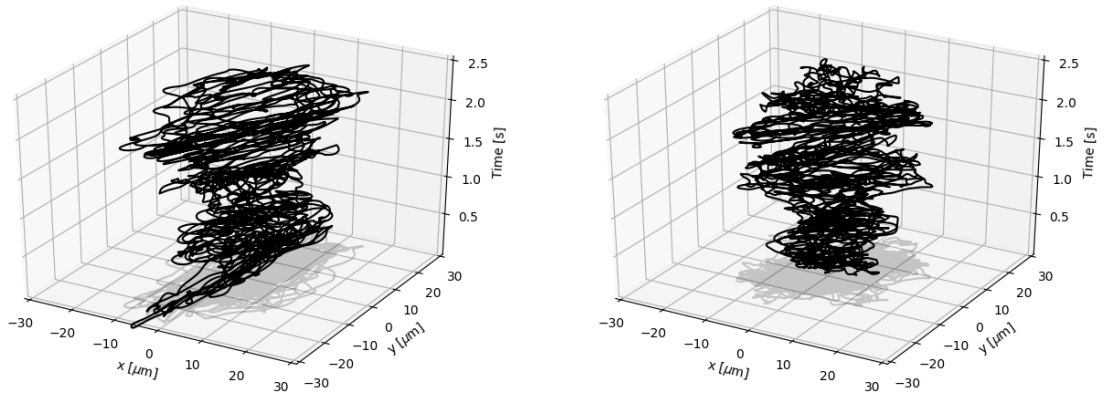

(a) Pure convection **(b)** Convection & exponential correlation

Figure 10.5: Evolution with time of the displacement in the center of the beam for different time correlation methods.

To supplement the earlier figures, Figure 10.6 showcases polar plots of the displacement in the center of the beam using different time correlation methods. Here, kernel density estimation (KDE) is applied to estimate the probability density function of the data, illustrating the concentration of points and hence facilitating a clearer understanding of previously discussed trends and behaviors.

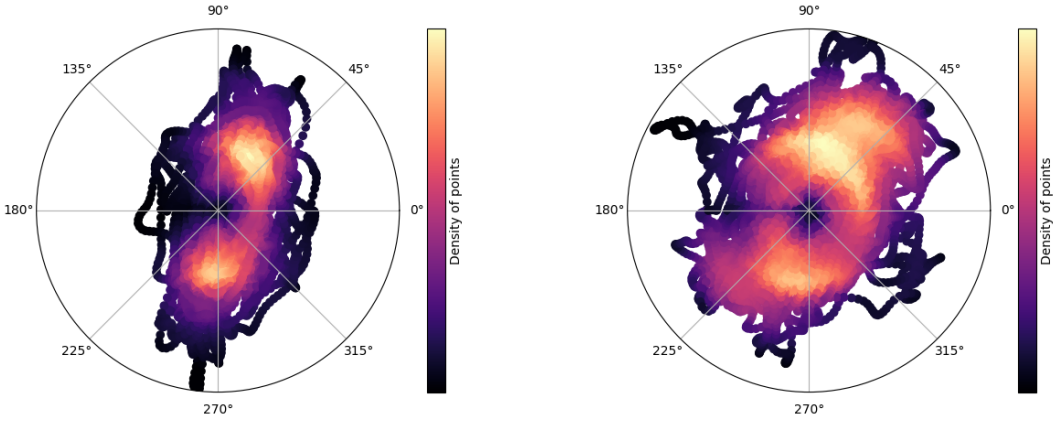

(a) Pure convection

(b) Convection & exponential correlation

Figure 10.6: Polar plots of the displacement in the center of the beam for different time correlation methods.

Having analysed the observable trends in displacement behaviors across different time correlation methods, the focus now shifts to the quantification of uncertainty inherent to each method. This will be accomplished through an analysis of the root mean square of the amplitude of displacements, taking into account variations in user-input parameters. In Chapter 8, it was showed that the PC method was dependent on model parameters such as the number of modes and random seed, whereas the C&EC was mostly independent. This dependency or not is now studied for the FSI cases. Figure 10.7 displays the root mean square (RMS) of displacement amplitudes, comparing various meshes, time correlation methods, and random seeds. All the PC simulations presented here, except the one with random seed = 2, were run by van den Bos et al. [34]. Firstly, looking at the C&EC results, it can be seen that with the mesh resolution increase there is a convergence of the results, which is a good sign. Moreover, for the mesh 50x40x300, the simulations run with different random seeds result in very similar displacements, which confirms what had been seen before. The uncertainty introduced by the random seed in the C&EC is estimated to be roughly 2.5% based on the data obtained here. This is in agreement with what was seen in the TCF case, where it showed 1.37%. Moving to the PC method, it is once again clear the dependency this method shows on the random seed. In the case of this method the uncertainty introduced by the random seed is estimated to be 19%. The difference in uncertainty between the two methods is significant, making the added computational cost of a slightly more restrictive time step well worth it.

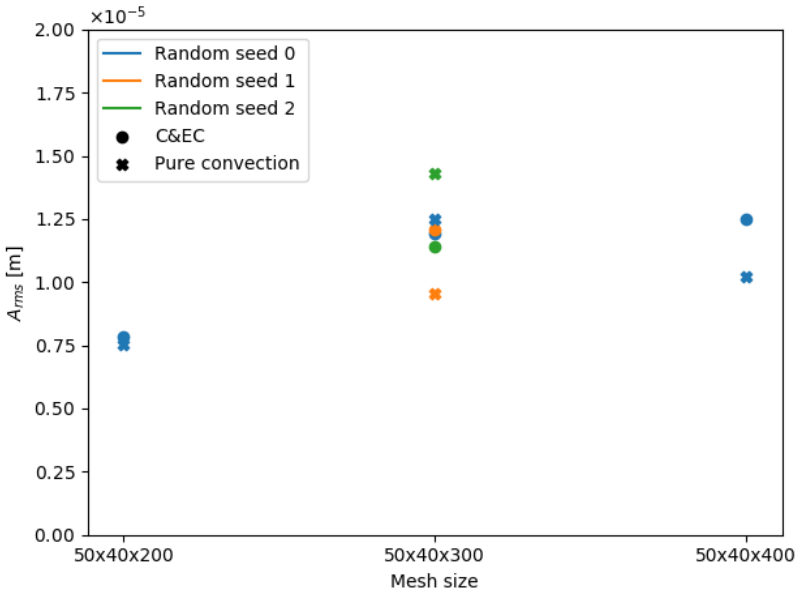

Figure 10.7: Comparison of the RMS of the displacement amplitude at the center of the beam for different meshes and time correlation methods.

As mentioned before, there are other parameters that introduce uncertainty in AniPFM. One of them is the number of modes used in the generation of the synthetic velocity fluctuations. While this parameter was not analysed for FSI simulations, it was for the TCF case (section 8.5) and an estimate can be constructed on the uncertainty introduced. Based on the data available, PC shows an average of 5% difference between using different number of modes, with no visible convergence towards higher number of modes. On the other hand, C&EC simulations show barely no difference in the results, with a sub 0.5% discrepancy in using different number of modes.

Another source of uncertainty is the size of the window on which the RMS of the displacements are computed. When comparing values computed over the entire simulation to those from the last 10 flow-throughs, it's evident that the PC simulations exhibit greater uncertainty than the C&EC simulations. Specifically, the former shows an average difference of approximately 3.4% uncertainty, while the latter displays around 0.7%.

The various sources of uncertainty mentioned for the different time correlation methods are summarized in Table 10.2. The quantification and summarizing of this information concludes the study of this topic. It is advised that the C&EC time correlation should be used over the pure convection method for lower uncertainty in the results.

Table 10.2: Uncertainty sources (%)

		Number of modes[1]	Random seed[2]	A_{RMS} calculation window size[2]
Time correlation method	PC	5	19	3.4
	C&EC	0.4	2.5	0.7

[1] Based off fluid-only simulations
[2] Based off FSI simulations

10.2.2. Calibrated model

The FSI results are now evaluated in terms of the baseline and calibrated versions, for both cut-off definitions, through changing the C_l value. The baseline corresponds to C_l = 3 and the calibrated versions correspond to the optimal values found in Chapter 8 - C_l = 2.0 for the Shur cut-off and C_l = 0.6 for the cubic cut-off. In that chapter, the hypothesis made was that by calibrating the magnitude of the

power fluctuations, the amplitude of displacements would decrease and increase AniPFM's accuracy in simulating TIV. This hypothesis is now tested here through the brass beam case. All the simulations were run with the C&EC time correlation method.

Table 10.3 shows the RMS amplitude of displacements for Shur's and cubic cut-off definitions, for both the baseline and calibrated versions. The findings confirm the validity of the initial hypothesis. By using the calibrated C_l values obtained before, the A_{RMS} are reduced in both cases, getting much closer to the validation data from Chen et al. [15].

Table 10.3: RMS amplitude of displacements

Cut-off	C_l	A_{RMS} [m] [1]
Shur	Baseline	1.13e-5
	Calibrated	7.16e-6
Cubic	Baseline	1.61e-5
	Calibrated	7.28e-6

[1] Validation data [15]: A_{RMS} = 6e-6

This reduction in the RMS of the amplitude of displacements should be associated with a decrease in the magnitude of the pressure fluctuations. In Figure 10.8 is displayed the pressure and amplitude power spectra for the different cut-off definitions, for their baseline and calibrated versions. First, by looking at the different pressure spectra, it is clear that indeed the reduction in the amplitude of displacements is associated with a lower power of the pressure fluctuations. Additionally, the difference in the magnitude of pressure fluctuations between Shur and cubic cut-off is clear, as it was seen before. Moreover, the calibrated versions of the different cut-off definitions show very similar pressure spectra, and also very similar A_{RMS}. This shows that both cut-offs can be used, given that they are properly calibrated. Shifting the attention from the pressure spectra to the amplitude, it can be observed that the different plots look very similar. The only difference between them is mainly a slight shift in the y axis, which corresponds to lower or higher amplitudes. In terms of shape they appear the same. This is expected as each peak corresponds to the different frequencies of vibration of the structure, and this is not expected to change. The first peak, which corresponds to the natural frequency (the most important one), is predicted to be f_1= 27 Hz by the current FSI framework, whereas Chen et al. [15] validation data have f = 28 Hz. This difference is in line with other numerical researcher's work. This is not relevant for the current discussion, as the predicted natural frequency has more to do with the structural parameters used in the model, as well as the structural solver and coupling algorithm. The focus of the current chapter is on the amplitude of displacements.

The outcomes of the analyses in this subsection are highly encouraging as they not only validate the initial hypothesis but also mark a significant milestone in the calibration, verification, and validation of AniPFM. These findings provide solid evidence for the robustness and accuracy of the model. It is worth noting that the empirical constant C_l was selected to match the RMS pressure fluctuations at the wall for the TCF case, rather than to fit the brass beam validation data. Using this calibrated constant in the brass beam simulations produced results that closely align with the validation data. This suggests that the calibration was successful for channel flows.

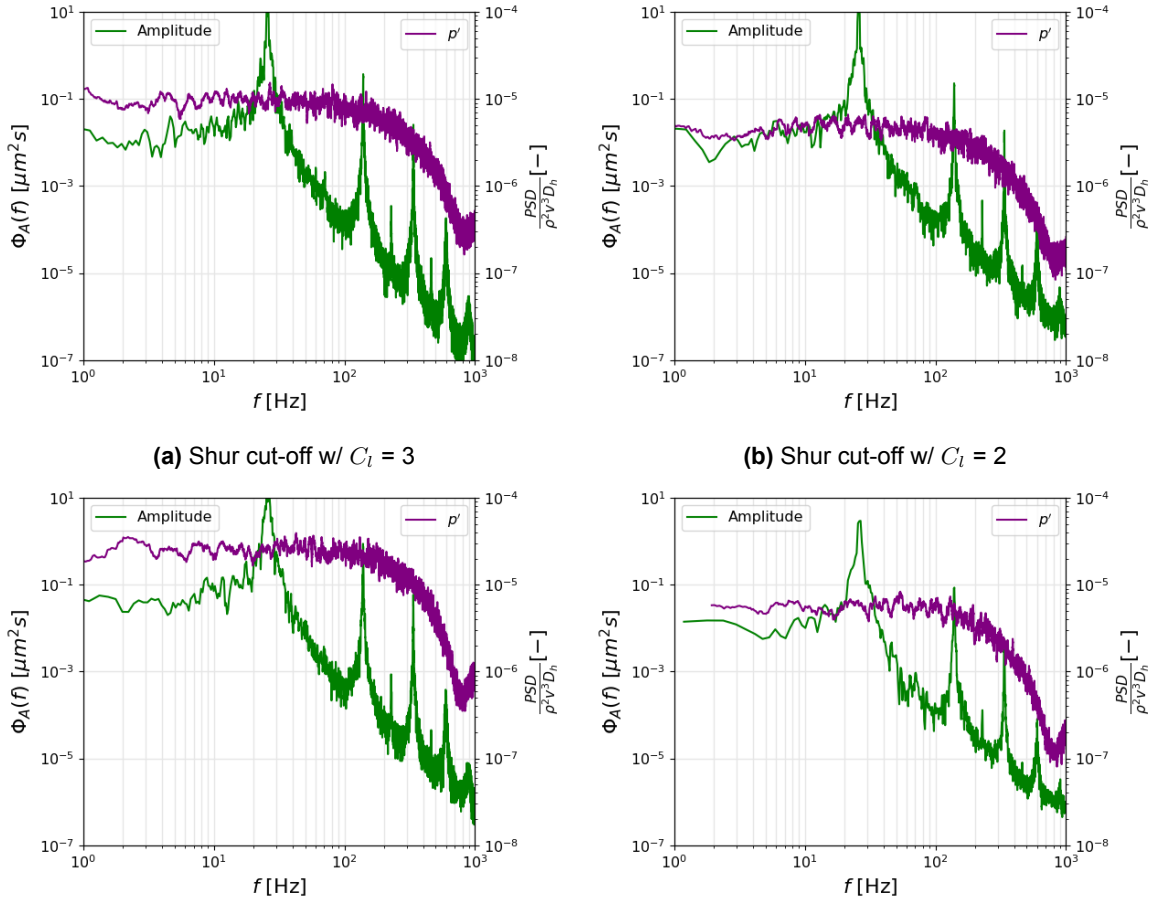

(a) Shur cut-off w/ C_l = 3

(b) Shur cut-off w/ C_l = 2

(c) Cubic cut-off w/ C_l = 3

(d) Cubic cut-off w/ C_l = 0.6

Figure 10.8: Pressure fluctuations and displacement amplitude spectra for different cut-off length definitions.

10.2.3. Comparison with other numerical approaches

It is important to compare AniPFM's approach to the problem of simulating TIV in fuel rods with other state of the art numerical approaches. This is the goal of this subsection, where the results of the LES from De Ridder [16], the PFM model from Kottapalli et al. [17] and the AniPFM FSI simulations ran by van den Bos et al. [34] are compared with the simulations run in the context of the current thesis, as well as with validation data from Chen et al. [15] and their analytical model. The difference between the simulations run by van den Bos et al. [34] and the ones presented as the 'Calibrated AniPFM' is that the former used pure convection, and the latter uses the calibrated C&EC and a calibrated C_l value. Both use Shur cut-off and the mesh is 50x40x300 with a random seed of 0 as the baseline value.

The comparison is presented in Figure 10.9. The root mean square of the amplitude of the displacements is plotted w.r.t the mean flow velocity for the different numerical approaches as well as validation data. The error bars in AniPFM data points represent the uncertainty associated with each time correlation method. These uncertainties were computed based off the values of Table 10.2, assuming independence of each uncertainty source. Comparing both AniPFM approaches, it can be seen that the calibrated version performs much better than the baseline one, when compared to validation data. And also with much less uncertainty. For example, for 10 m/s, the calibrated AniPFM shows a 19% $\pm$ 2.6% deviation from Chen et al. [15] data, whereas previous AniPFM simulations show a 108% $\pm$ 19.9% deviation. The LES approach from De Ridder et al. [16] shows a 38% discrepancy compared to experimental data. The calibrated AniPFM shows the possibility of outperforming LES while requiring significantly lower computational resources. While further validation and testing are required, the results are highly encouraging to continue working on this model.

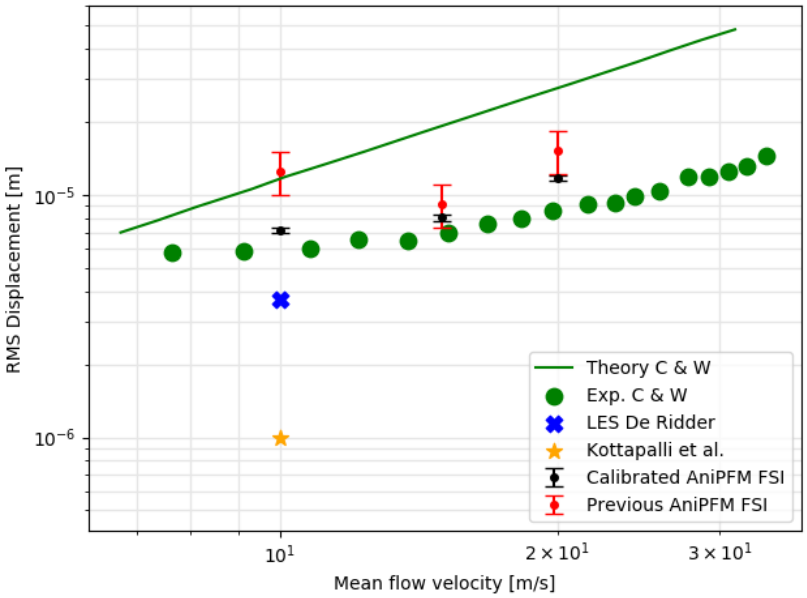

Figure 10.9: Comparison of the RMS vibration amplitudes of the calibrated AniPFM with other researcher's work [15–17].

10.3. Which wavenumbers most contribute to the vibrations?

Turbulence is inherently a multiscale phenomenon, and capturing more of these scales in simulations increases the computational burden. If it would be possible to simulate only the most important scales (wavenumbers), the computational cost of such numerical simulation would decrease. Although wavenumbers and time frequencies are not directly linked, a structure's natural frequency may provide clues to identifying significant wavenumbers. An attempt can be made to tailor the cut-off filter to include wavenumbers that relate to the natural frequency of the structure and exclude the ones that are less relevant. The aim would be to assess whether limiting the range of considered wavenumbers could still accurately model the fluctuations that trigger structural vibrations. If successful, this approach could enable the use of coarser meshes, significantly reducing the computational cost of AniPFM without compromising the model's accuracy. This preliminary approach is the focus of the current section. While the work is still in its early stages, its potential success could justify more extensive research efforts to refine and expand upon this method.

It is not trivial to link a frequency with a wavenumber. Frequencies are inherently linked to time, whereas wavenumbers are to space. Through the use of dimensional analysis an attempt was made at figuring out the most important wavenumbers to the excitation of the natural frequency vibration of the structure. This is shown in Equation 10.1, where f is the frequency of the rod, in this case f = 28 Hz. The dimension resulting from this expression is correct as per the dimension of a wavenumber. The hardest part is to find the correct or most appropriate value for the magnitude of the velocity fluctuations, U'_{mag}.

$$k = \frac{2\pi f}{U'_{mag}} = \frac{T^{-1}}{L^1 T^{-1}} = L^{-1} \tag{10.1}$$

By taking into account the amplitude of displacement seen in FSI simulations, multiple probes were placed very near the wall. The probe signal was averaged over time and the different probes were also averaged among them, providing a magnitude of velocity fluctuations that is averaged both in time and space. The value obtained was U'_{mag} = 0.089 m/s. Introducing this in Equation 10.1, a wavenumber k = 1976 m^{-1} is obtained.

In order to only account for the wavenumber obtained and the ones lower, the cut-off length was modified. The cut-off definition used was Shur's. To this definition, it was subtracted a value such that at the wall k_{cut} = 2100 m^{-1}. This value is slightly higher than the one obtained above. This is meant to give

some margin as these calculations are not fully reliable to predict the velocity fluctuations magnitude that should be introduced in the equation. This modification of the cut-off wavenumber is displayed in Figure 10.10. Note that while, the whole channel is affected, the only part of interest for this study is the inner wall behaviour.

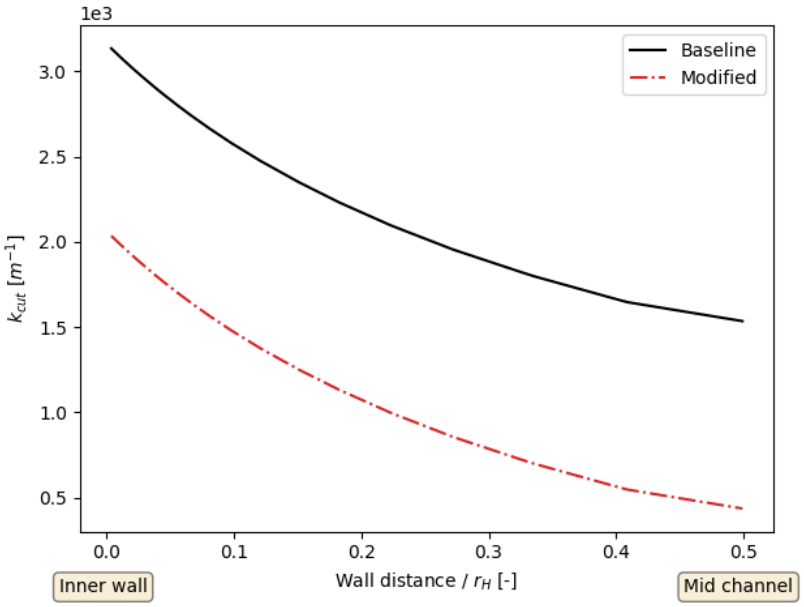

Figure 10.10: Modified cut-off wavenumber.

An FSI simulation was run with this cut-off wavenumber modified definition. The inflow velocity is 10 m/s and C_l is set to the baseline value of 3.0. As a result of this simulations, the RMS of the displacement obtained was A_{RMS} = 8.89e-6. Compared to the equivalent value in Table 10.3, this simulation shows a decrease of 21%. While the difference is not substantial, it can be attributed to multiple wavenumbers contributing to the same frequency. The most significant wavenumbers are retained, but some that contribute less are cut off. Therefore, a difference in the amplitude of displacements between the two approaches is expected.

To better understand the effect this modification of the cut-off wavenumber has on the results, the pressure fluctuations and amplitude spectra are analysed. These can be visualised in Figure 10.11. Compared to Figure 10.8a, the pressure spectrum here shows an overall decrease in energy. Note also that the local peak in energy in the higher frequency scales is no longer present. Despite this, the spectrum looks different from what was expected. It was expected that the energy would remain closer to the baseline simulation near the natural frequency, and decrease mostly for frequencies higher that this. This is different from the general decrease across all frequencies that can be observed when comparing both plots. There is no clear understanding of the reason behind this as of now. Due to lack of time, this study had to be cut short, but it results show that this could prove interesting and thus further research would be advised.

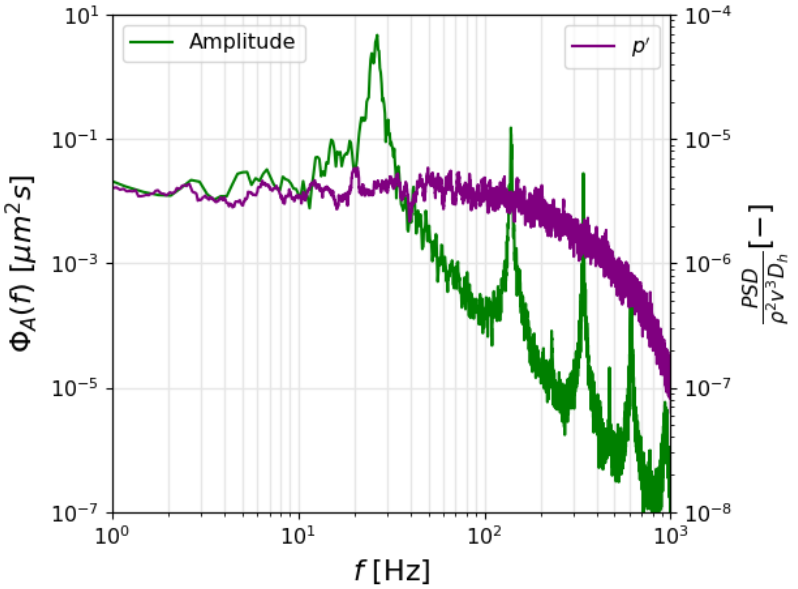

Figure 10.11: Pressure fluctuations and displacement amplitude spectra for the simulation using the modified cut-off wavenumber.

10.4. Summary

In this chapter, the brass beam in turbulent axial water flow was simulated as elastic through FSI simulations, utilizing AniPFM as the source of excitation generation. The simulation setup was described in detail and benchmarked against other state-of-the-art approaches. Different time correlation methods were analyzed in terms of their displacements, both visually and quantitatively. Simulations utilizing the pure convection method displayed unphysical vibrations, characterized by a significantly higher amplitude of displacement in the y direction compared to the x direction. This phenomenon was not observed with the C&EC method, which exhibited vibrations more in line with what was expected. The uncertainty sources inherent to each method were also evaluated, encompassing factors such as the number of modes, the random seed, and the window size used in calculating the RMS of displacement amplitudes. The C&EC and PC methods demonstrated total uncertainties of 2.6% and 19.9%, respectively.

Moreover, the calibrated version of AniPFM was analysed, substantiating the earlier hypothesis in the thesis that calibrating the empirical constant in the definition of the length scale, associated with the TKE peak, would consequently calibrate the pressure fluctuations. This adjustment reduced the overprediction of displacement amplitudes in FSI simulations that were evident in the baseline AniPFM model. The calibrated versions using the different cutoff lengths definitions performed very similarly and close to validation data. Additionally, AniPFM was compared with other numerical approaches, proving to be a promising cost-effective model to be integrated into FSI simulations of vibration of fuel rods. Lastly, an analysis was undertaken to identify the primary wavenumbers contributing to the beam's vibrations, aiming to decrease computational costs by concentrating solely on these key wavenumbers. While additional research is required for definitive conclusions, this strategy seems promising.

11

Cantilever rod

In an effort to continue the validation of AniPFM's integration into NRG's FSI framework, another test case is devised. This case concerns turbulent axial flow over a flexible rod with a clamped-free configuration. It is chosen due to the vast amount of data available for comparison, both from numerical replications of the experiment as well as the experiment itself. The chapter starts with the description of the experimental setup of Cioncolini et al. [18] as well as the state of the art numerical replications of Salacha et al. [19] and Norddine et al. [14]. The setup used in this thesis is then described. Subsequently, the results obtained from the simulations considering the rod fixed are showcased. Lastly, the URANS FSI simulation results are shown and compared with experimental values.

11.1. Experiment and previous numerical setups

This section entails the detailed description of the experiment performed of a flexible cantilever rod in turbulent axial flow. Additionally, it also describes the approaches taken by some researchers to numerically replicate this setup.

11.1.1. Experiment

An experiment performed by Cioncolini et al. [18] examined axially induced vibrations of a cantilever rod for nuclear applications. The rod, which is of cylindrical shape, is clamped at one end and free at the other. It is confined within a tube, and experiments were done with flow from the free to the clamped end as well as the opposite. This is a simplified representation of a nuclear fuel rod, as it does not include the mixer grid, and only one rod is used, thus no multi-body effects are present. The experiment is a great benchmarking case because of the strong two-way coupling between the flow field and the structure, together with the simplified geometry. The test setup, as shown in Figure 11.1, has a confining tube with diameter D_o = 21 mm and a rod with diameter D_i = 10 mm. The rod length is L_{rod} = 1.06 m, and two configurations of rod ends were used: a blunt end and a hemispherical end. The confining tube has a length of L = 2.5 m. A flow straightener was used to remove any swirls or secondary flow effects. Instead of a one-pipe radial outlet, a symmetric two-pipe outlet was used to avoid any localized cross flow near the fixed end of the rod. The flow velocity varied between 1.01-3.45 m/s, with the maximum flow velocity approximately 30% less than a nominal reactor core. The Reynolds number was equal to 10% of typical reactor applications, partly due to the use of water in ambient conditions and partly due to the smaller hydraulic diameter of the rod compared to that of a nuclear reactor core. The experimental data includes full time series of the total displacement, from which the modal frequencies can be derived. The RMS displacement and the frequencies of the rod are available for both configurations for the entire range of Reynolds number and flow velocity. For certain flow velocities and Reynolds numbers, the displacement history of the first 5 seconds, the power spectrum of the displacement, and the auto-correlation function are given. PIV measurements were also performed at the free end of the rod, which were used to visualize the flow field in this area.

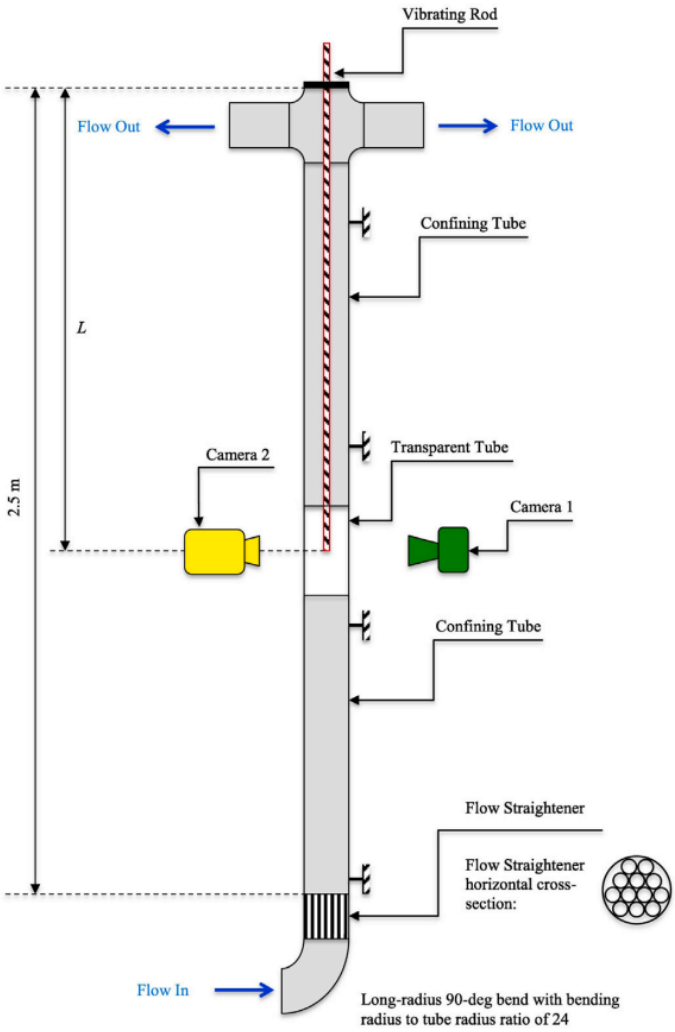

Figure 11.1: Schematic representation of the test rig of the experiments conducted by Cioncolini et al. [18].

11.1.2. Numerical replications

The experiment described has gained significant attention from researchers in recent years, primarily due to its extensive dataset, its resemblance to flow conditions in nuclear fuel rods and its relative simplicity. As a result, it has often been numerically replicated as a means to validate various computational approaches.

Salachna et al.

A few years after the experiment was performed, Salachna et al. [19] investigated the computational modelling of flow induced vibrations of cantilever rods subjected to turbulent axial flow at operating conditions relevant to those of fuel rods of pressurized water cooled nuclear reactors. For this, they replicated numerically the experiment described above. The aim of their research is to ensemble and validate a URANS modelling strategy of FIV. For this they used a RSM model approach of turbulence, more specifically LRR model, integrated into an FSI framework.

Norddine et al.

As part of the Vibration ImpaKt In Nuclear power Generation (VIKING) consortium, Norddine et al. [14] conducted preliminary wall-resolved Large Eddy Simulation (WR-LES) experiments on cantilevered rods (same geometry as mentioned above for Salachna et al.). These simulations were performed at a Reynolds number of 60,000, featuring both blunt and curved rod ends. The standard Smagorinsky

model with the Van-Driest wall damping function was applied. The study investigated flow statistics and mechanical stresses exerted on the rods. Only fluid simulations were run.

11.2. Simulation setup

The simulation setup used in this thesis is now described. It is based on the one by Salachna et al. [19]. A sketch of the fluid and solid domains is shown in Figure 11.2. The different regions are shown: inlet, outlet, fixed wall (outer wall) and moving wall (beam). The inlet velocity is set as uniform U = 1 m/s. The beam is clamped on the outlet region and free on the other end. As such, the flow is going from the free to the clamped end. The main difference between this setup and the experimental one is the use of an annular outlet versus the symmetric two-pipe outlet. This approach was chosen for various reasons. First, being that it replicates the numerical setup of Salachna et al. [19] providing means for a fairer comparison. Additionally, this region is not expected to have a significant effect on the results as it is very close to the clamped end of the beam. The last reason for this choice is the simplicity of this outlet setup versus the experimental one. The solid properties of the rod are the same ones used by Salachna et al. [19], which were adapted to match the natural frequency of the vibrating beam of Cioncolini et al. [18] experiments. While, this approach is not ideal, it is accepted here. The rod used in the experimental apparatus is a stainless steel tube which is filled with lead shots (to approximate the density of PWR fuel rods). This is not trivial to replicate numerically, and as such the simplified approach of Salachna et al. [19] is taken here. This also allows for comparison with their numerical approach. The solid properties of the rod are summarized in Table 11.1. Similarly, the fluid properties are summarized in Table 11.2.

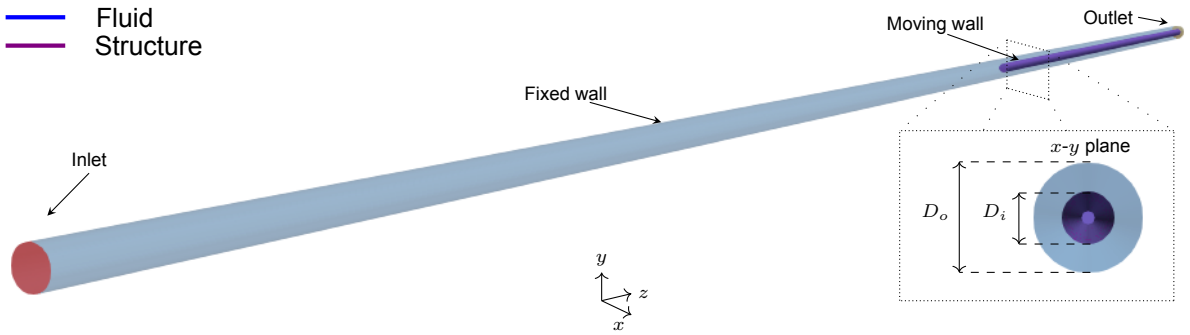

Figure 11.2: Fluid and solid domains.

Table 11.1: Solid properties

Solid properties	
Length, L[m]	1.06
Diameter, d [m]	0.01
Density, $\rho_S \left[\frac{\text{kg}}{\text{m}^3} * 10^3\right]$	7.49
Young modulus, E [GPa]	76.4

For the discretization of the fluid domain, three meshes were constructed. Their different resolutions can be seen in Table 11.3. Compared to the previous cases analysed in this thesis, this case is a clear step up in terms of computational cost, as the coarsest mesh is already in the order of millions. Besides the number of cells, in the table it is also shown the r^+ and z^+ associated with each mesh for the wall of the rod (named 'inner' here) and for the tip of the rod, which is separated here, as it is influenced by the mesh discretization in the z direction (streamwise) rather than in the r direction (radial). Looking at the different meshes parameters, it can be observed that while the 'inner' wall region is wall resolved, the tip region is not so much. This is because of the inherit cost of having such a long domain. Even though there is grading in the z direction, in order to have a z^+ close to 1 in this direction, a mesh of at least 10M is needed, given that the domain is kept the same. One could think of increasing the grading

Table 11.2: Fluid properties

Fluid properties	Value
Chanel diameter, D [m]	0.021
Chanel length, L[m]	2.5
Hydraulic diameter d_h[m]	0.011
Density, ρ_F $\left[\text{kg m}^{-3}\right]$	997
Kinematic viscosity, v_F $\left[\text{m}^2\ \text{s}^{-1}\ \left(*10^{-6}\right)\right]$	0.893
Inlet velocity, U $\left[\text{m s}^{-1}\right]$	1
Reynolds, Re_{ann} [-]	$16.1 * 10^3$

intensity instead of the number of cells, but as it is now, the grading is already the maximum possible that does not lead to very low quality cells. The grading is of course limited by the dicretization in the other directions as well, as such to avoid flat cells (volume near zero). In Figure 11.3c, it is shown a close-up of the grading in the z direction in the region of the tip of the rod for the coarse mesh. In addition, Figure 11.3a shows a close-up of the mesh at the inlet and Figure 11.3 shows a cross-section of the annular region, where both fluid and structural meshes are displayed. The grading of the fluid mesh in the radial direction can be seen here. The structural mesh has a discretization of 6x6x50. The effect of this discretization was not studied, but it is something that should be done in the future. Although it is expected that this mesh is fine enough, as it is similar to the one used in the brass beam case (which has a slightly longer length and radius), which was proven to be fine enough. Moreover, the fluid and structural solvers, as well as FSI coupling algorithm and settings used are the same ones that have been presented and used in the previous chapters.

As it is right now, this case is extremely costly computationally. One way of reducing this cost is to reduce the domain size in the region where the flow is developing. By running simulations of just the developing region it is possible to obtain the velocity profile of the fully developed flow. This is then used as input for another simulation with a reduced 'developing' region, thereby reducing the number of mesh cells. For this it is necessary to perform an independence study to understand what is the minimal size possible for the initial region. While this was not performed in this thesis, it is advised for the future.

Table 11.3: Cantilever rod flow mesh resolutions

Mesh	N_{cells}	$r^+_{inner_{avg}}$	$r^+_{inner_{max}}$	$z^+_{tip_{avg}}$	$z^+_{tip_{max}}$
Coarse	1.9M	0.46	1.02	13.10	22.99
Medium	4.2M	0.34	0.69	9.74	19.21
Fine	8.2M	0.31	0.62	4.22	12.34

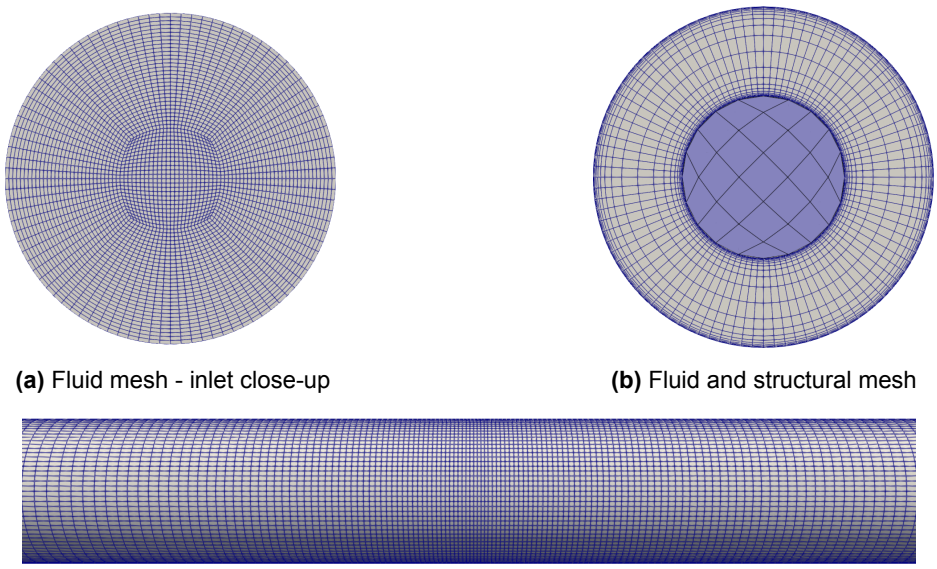

(a) Fluid mesh - inlet close-up

(b) Fluid and structural mesh

(c) Fluid mesh - z grading close-up

Figure 11.3: Fluid and structural meshes close-ups.

11.3. Pure flow simulation results

Initially, a simulation with the rod considered fixed is run. This simulation is purely a fluid simulation, without any structural solver integration. Due to a lack of time, it was only possible to run this simulation with the coarse mesh. First, a URANS simulation is run (without AniPFM), similarly to the other cases, so it can serve as initialization of the domain later on. An adaptive time step is taken with the max CFL number constrained at 1.0. Figure 11.4 shows the comparison of the flowfield around the tip of the rod between the current simulation and the one performed by Salachna et al. [19]. The results are very similar: as expected, there is a stagnation point at the tip of the rod, very high velocities coming out of the edges of the said rod and a small separation zone near the wall after the tip. The length of this separated region is also very similar for both simulations (around $0.6D$), even though in the current simulation the linear $k-\omega$ SST turbulence model is used and in Salachna et al.'s [19] simulation, the RSM LRR is used. Anyways, the results between both simulations are very similar for the whole area of interest seen here, with the maximum value of the velocity being very similar for both cases.

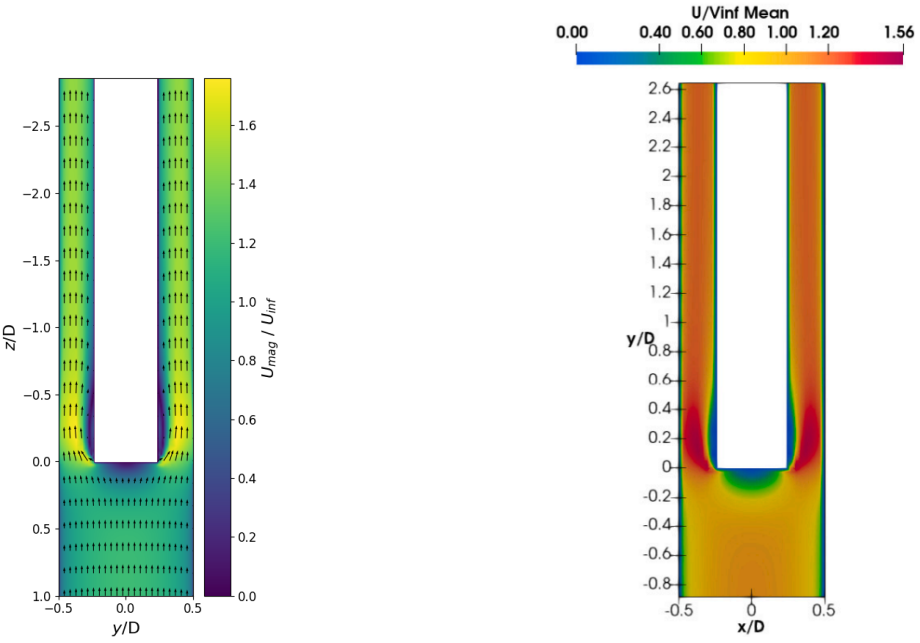

(a) Current simulation **(b)** Salachna et al. [19]

Figure 11.4: Comparison of the flowfield around the rod tip with other numerical approaches results [19].

Once the initialization simulation was performed, AniPFM could be turned on. For this the C&EC time correlation method was used as well as the Shur cut-off with C_l = 3.0. The simulation was run for 10 seconds, which is equivalent to 4 flow-throughs. The mesh used was the coarse one. The profiles of velocity, turbulent kinetic energy and normal Reynolds stresses can be observed in Figure 11.5. These results are taken at a plane at z = 1.8m (0.74m from the tip), which is already in the annular region. The results by themselves are not conclusive, as this was the only simulation performed. The coarseness of the mesh is clearly visible in the results. Additionally, the profiles look as expected from an annular region, with a similar shape to the annular turbulent flow seen in Chapter 9.

Unfortunately, Salachna et al. [19] does not have turbulence statistics as the ones shown here. Norddine et al. [14] do have these statistics at multiple planes along the streamwise direction, which is extremely useful for comparison. However, they only performed simulations at an inlet velocity of U = 3.45 m/s. Since the initial goal of the current simulation was to then compare with the numerical approach of Salachna et al. [19], who only ran simulations at an inflow of U = 1 m/s, only this case was considered. However, for future work, running cases at U = 3.45 m/s, is extremely valuable due to the amount of important comparison data available from Nordinne et al. [14].

The results highlighted in this section, although in the initial stages, lay a solid foundation for future research in fluid and FSI simulations of the cantilever rod using AniPFM.

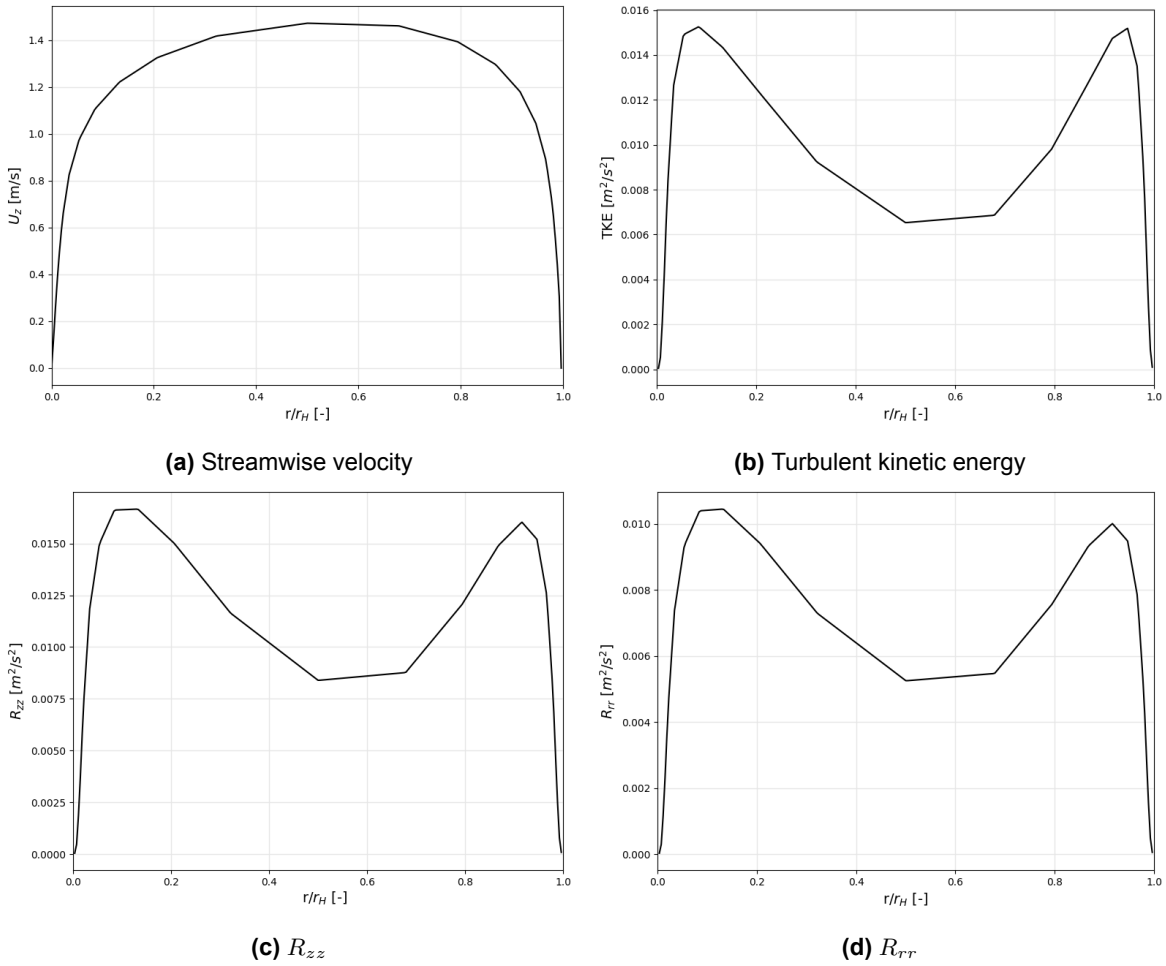

(a) Streamwise velocity

(b) Turbulent kinetic energy

(c) R_{zz}

(d) R_{rr}

Figure 11.5: Profiles of velocity, TKE and Reynolds stresses at z = 1.8.

11.4. URANS FSI results

In order to check the correctness of the fluid and structural parameters used in this simulation, an initial FSI simulation was run without AniPFM. Since this simulation has no excitation source for the vibrations, an initial force has to be set. For this, a force of 0.1N was applied in the y direction for 0.1s. The beam was then left vibrating freely. The displacement in the y direction of the free end w.r.t time is displayed in Figure 11.6. From this displacement, the modal characteristics of the vibrations of the beam can be computed. These are shown in Table 11.4 in comparison with the experimental data of Cioncolini et al. [18]. The close agreement of the results with the experimental data offers a validation of the FSI framework, setting a solid foundation for the continuation of this project. Due to a lack of time, no FSI simulations were run using AniPFM. This is considered future work and will be discussed in Chapter 13.

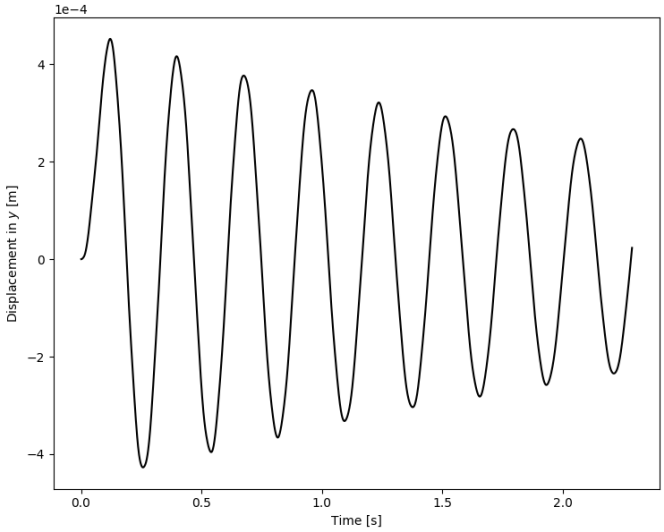

Figure 11.6: Time series of displacement in the y direction.

Table 11.4: Comparison of results with experimental data

Value	Simulation	Experiment (Cioncolini et al. [18])
Natural frequency, f_1 [Hz]	3.59	3.60
Damping ratio, ζ [-]	0.013	0.012

11.5. Summary

In this chapter, the details of the numerical replication of the experimental cantilever rod experiment conducted by Cioncolini et al. [18] were discussed. Initially, the experiment was introduced: it involves a cylinder clamped at one end and left free at the other, with an enclosing tube concentric to the cylinder. Water flows from the free end to the clamped end. Subsequently, the numerical replications of this experiment available in literature were summarized: this entails the work of Salachna et al. [19] and Norddine et al. [14].

Next, the setup used in the current thesis was described to detail. This setup follows closely the one presented by Salachna et al.. Following this, the results of the simulations were showcased. Initially, simulations were conducted with the rod considered rigid, involving fluid-only simulations. The mean flow results align with those reported by Salachna et al. [19]. Moreover, turbulence statistics, including TKE and normal Reynolds stresses, derived from the AniPFM simulations, were also presented. Lastly, the outcomes of a URANS FSI simulation were exhibited, where the modal characteristics were compared with experimental data, and good correlation was obtained.

The research delineated in this chapter, though in its initial phase, offers a robust starting point for future researchers working on this project. Additionally, recommendations are made throughout the chapter for possible future improvements in the numerical setup.

Part IV

Closure

”*We do not learn from experience... we learn from reflecting on experience*.”

John Dewey

12 Conclusion

The research questions outlined in Chapter 2 are reiterated here, accompanied by a discussion on the conclusions drawn regarding each question. Subsequently, the main research objective is repeated, followed by its conclusions.

12.1. Research questions

What are the optimal parameters of the AniPFM that maximize accuracy and reduce computational cost and uncertainty?

Across three chapters: two fluid-only cases (TCF - Chapter 8, and turbulent annular flow - Chapter 9) and one FSI case (brass beam - Chapter 10), an in-depth analysis was conducted on AniPFM's parameters that were mentioned at the end of Chapter 7. Previously, the model's sensitivity to these parameters was not fully understood, and optimal parameters had not been identified.

First, regarding the time correlation method of the velocity fluctuations. The pure convection method showed great dependency on parameters such as the random seed used in the pseudo-random number generator for the angles that constitute the equation for the wavenumber vector, as well as the number of modes used in the Fourier series decomposition that generates the non-dimensional space-only velocity fluctuations. This dependency leads to a higher uncertainty in the results obtained using the model. This dependency was confirmed through FSI cases for the random seed. On the other hand, the convection and exponential correlation method does not exhibit this strong dependency that the pure convection does on these parameters. This allows AniPFM to produce realizations which have a very low variance and thus, generate results which are 'more deterministic' even though they come from an inherently stochastic model. This time correlation method is the one that is advised to be used. Although at a slightly higher computational cost than PC, it offers much more reliable results. Within the C&EC method, the correlation factor, f_τ, was studied. It was shown that a value within 25-100 is ideal, and there is not much difference between them. Values lower than this show a greater decrease in the velocity fluctuations magnitude due to an increased weight onto the numerically diffused field.

Secondly, concerning the TKE spectrum, two length scales were studied: the length scale associated with the peak of the spectrum, l_e, and the cut-off length scale, l_{cut}. Two formulations were considered for the definition of l_e: $C_l l_t$ and min($2d_w$, l_e). The latter greatly underestimates l_e near the wall and was discarded. The former was calibrated through the empirical constant C_l. This constant was set to its default value, which stems from the calibration performed by Shur et al. [10] on a plane mixing layer. The idea of calibrating this constant arose not only as a further effort in calibrating the model to its respective use case but also as a way to possibly avoid the overprediction of the amplitude of displacements seen before by FSI simulations using AniPFM. The results of fluid-only simulations showed that indeed calibrating this constant reduced the pressure fluctuations magnitude near the wall, both the mean square root as well as the spectral power density over all frequencies and wavenumbers. This hypothesis was then tested in the FSI case of the brass beam and proved successful. Further validation is needed, but this greatly reduced the overprediction of the A_{RMS}, bringing AniPFM FSI results much closer to validation data over all the velocities simulated. Regarding the cut-off length, both the Shur and cubic cut-off definitions were able to obtain good results if calibrated accordingly through the

C_l constant. The cubic cut-off requires a lower value of this empirical constant, as it cuts off the TKE spectrum at a higher wavenumber than the Shur definition. The cubic cut-off results in a better near-wall behavior of the Reynolds stresses than Shur's. But Shur's leads to a more correct distribution of the energy across the different frequencies/wavenumbers. It is not clear yet if one method is better than the other. Each one has its advantages and disadvantages.

What is the influence/sensitivity of the AniPFM input Reynolds stresses in the RMS of the generated velocity and pressure fluctuations fields?

In an effort to understand why AniPFM was overpredicting the pressure fluctuations near the wall, the governing equation for the pressure fluctuations was analyzed. Through its simplification for the TCF case by assuming statistical homogeneity in the spanwise and streamwise directions, it became possible to better understand the influence of the RST on the generated pressure fluctuations. It was observed that there was a clear influence of the wall normal component of the Reynolds stresses (the only statistically inhomogeneous direction). This dependence aided in understanding why, even though the other components of the Reynolds stresses were far from DNS data, the pressure fluctuations were still being overpredicted. While the influence of the RST on the generated pressure fluctuations is not trivial, there is now a better understanding of it.

This reinforces the importance of the anisotropy in the model, as it allows for a better prediction of the different components of the RST, which clearly have different near wall behaviours as well as different weights on the importance they have on the generated pressure fluctuations. As such they should not be treated equally (isotropy).

What is the accuracy and computational cost of NRG-FSIFOAM with AniPFM in simulating TIV in fuel rods when compared to other state of the art methods?

Reflection upon the performance of the calibrated AniPFM in the brass beam case, it has showcased promising potential, demonstrating a deviation of 19% $\pm$ 2.6% when compared against the data presented by Chen et al. [15] at a speed of 10 m/s. This positions it favorably against the LES approach of De Ridder et al. [16], which recorded a 38% discrepancy with the experimental data. The mesh used by De Ridder et al., extrapolated to a full rod would be of around 720 million cells, whereas the meshes used in this thesis for this case are always less than 1M cells. Although further validation is needed, the results obtained through the integration of AniPFM in NRG-FSIFOAM framework to simulate turbulence induced vibrations of fuel rods seem promising.

12.2. Research objective

> *To delve into a comprehensive exploration of AniPFM to fully grasp its sensitivity to various user-defined parameters. This endeavor aims not only to enhance understanding but also to pinpoint the optimal set of parameters that can potentially reduce uncertainty and increase accuracy in simulating near wall pressure fluctuations*.

Reviewing the research performed and its findings, it becomes clear that the research objective was successfully pursued, resulting in a deeper understanding of AniPFM, its sensitivities, and ideal parameters. While there is much to be done to enhance the model's accuracy and reliability through validation, this research helps foster confidence in the model's potential for successful integration into a low-cost framework for simulating TIV of fuel rods.

13

Recommendations

Based on the research presented in this thesis, recommendations are made for future work:

- Continue the development of the validation case of the cantilever rod. Run unsteady fluid only simulations with AniPFM for the medium and fine meshes. Use these results to run FSI simulations and compare the results with the experimental data from Cioncolini et al. [18] and the numerical data from Salachna et al. [19].
- Do the same procedure as above for fluid only simulations, but for an inlet velocity of U = 3.45 m/s. Norddine et al. [14] ran LES of the same configuration at this inlet velocity and provides turbulence statistics at various planes in the domain. This is useful for comparison with AniPFM, without the burden of running FSI simulations.
- Consider reducing the fluid domain of the cantilever rod. Use an inlet velocity equivalent to a fully developed velocity profile and reduce the 'developing region' as much as possible without influencing the flow at the rod.
- The calibrated values obtained for C_l for the different cut-offs have only been tested on the TCF at a specific Re_τ and on the brass beam. While the values calibrated for TCF showed a very good behaviour in the brass beam case, it would be important to validate this with other cases. Ideally, fluid only cases, to speed up computations and to reduce the overall complexity. Some recommended cases include: TCF at other Re_τ values (relevant for nuclear fuel rods applications), turbulent annular flow at other conditions. These are simple but useful cases. For the TCF there is a lot of high fidelity data available, for the turbulent annular flow not so much. If needed, considering running in-house LES or DNS. This was considered early on this thesis, but dismissed for lack of time.
- The understanding of what changing the C_l does to the TKE spectrum comes purely from an analytical perspective as well as causal inference based on the p'_{RMS} profiles. To confirm this, it would be useful and interesting to use the HIT box to study the effect of changing the C_l constant on the energy spectrum. This flow case is extremely simple and there is plenty of validation data.
- Further validate the integration of AniPFM in FSI simulations of fuel rods. A step up in complexity can be considering fuel rod bundles instead of a single rod. While a single fuel rod is ideal for the development and validation of a recent model like AniPFM, the ideal end goal would be rod bundles in axial flow. The flow physics are more challenging as there are multi body effects.
- The simulations performed during this thesis showed the importance of having a fine and high quality mesh in order to obtain relevant results using AniPFM. Only structured meshes were used. These meshes are only possible for simple cases, such as the ones considered here. For more complex cases, unstructured meshes would be needed eventually. This thesis did not extend to the exploration of unstructured meshes; nonetheless, it would be worthwhile to explore the performance of AniPFM in scenarios that necessitate unstructured mesh configurations.

- Continue the work performed during this thesis in understanding what are the most fundamental wavenumbers/frequencies that affect the structural vibration. The current approach showed that the A_{rms} is still within validation data range even though the cut-off wavenumber was greatly reduced. However, unlike expected, the drop in the pressure fluctuations power spectral density occurred across all frequencies, instead of mostly on the higher frequencies. It is then important to understand what is causing this and also if the current approach is the most correct one.
- Until now, only EVMs with Wilcox correction have been used in the URANS input of AniPFM. It would be interesting to study the effect of using RSMs, such as the ones already implemented in OpenFOAM (LRR and SSG). It is expected that this will lead to a more accurate representation of the input Reynolds stresses.
- Despite being more computationally economical than RSM while potentially offering better accuracy compared to EVMs, explicit algebraic RSM (EARSM), remain unimplemented in OpenFOAM. Future research could explore the implementation of an EARSM in OpenFOAM to improve the accuracy of the input URANS in AniPFM.
- In AniPFM, the energy spectrum is presumed to be isotropic initially, before being adjusted to represent the anisotropy in the input Reynolds stress tensor. This approach inherently dictates that the cut-off length is represented by a scalar value, a simplification that may not hold near walls where cells in the mesh are generally anisotropic and exhibit greater refinement in the wall-normal direction. Castro et al. [129] introduced an alternative by devising a synthetic turbulence model based on a distinct energy spectrum defined for each principal axis, thereby enabling the specification of a cut-off length aligned with these axes. It is recommended to study this approach and evaluate whether this can be implemented into AniPFM.
- As it was seen during this thesis, the expression for k_{start} has some flaws. The distribution of k_{start} should be studied for flow cases where the cross section area is not constant along the domain (as the cantilever rod case). If the value of this wavenumber remains $2\pi/l_{user}$ across the whole domain (as it was seen for the channel flows studied in this thesis), it is recommended that a new expression is devised for k_{start*}.

Bibliography

[1] The Federation of Electric Power Companies of Japan, Pressurized water reactor, https://www.fepc.or.jp/english/nuclear/power_generation/mechanism/sw_mechanism_02/index.html.

[2] Encyclopedia Britannica, Nuclear reactor - types of reactor, https://www.britannica.com/technology/nuclear-reactor/Types-of-reactors.

[3] E. Naudascher, D. Rockwell, Flow-Induced Vibrations, Courier Corporation, 2012.

[4] M. P. Paidoussis, Dynamics of flexible slender cylinders in axial flow Part 2: Experiments, Journal of Fluid Mechanics 26 (1966) 737–751.

[5] J. Degroote, Partitioned simulation of fluid-structure interaction, Archives of Computational Methods in Engineering 20 (3) (2013) 185–238. doi:10.1007/s11831-013-9085-5.

[6] B. Gatzhammer, Efficient and flexible partitioned simulation of fluid-structure interactions, Ph.D. thesis, TU MUnich (2014).

[7] C. Farhat, M. Lesoinne, Two efficient staggered algorithms for the serial and parallel solution of three-dimensional nonlinear transient aeroelastic problems, Computer Methods in Applied Mechanics and Engineering 182 (3-4) (2000) 499–515. doi:10.1016/s0045-7825(99)00206-6.

[8] S. B. Pope, Turbulent Flows, Cambridge University Press, 2000. doi:10.1017/cbo9780511840531.

[9] F. Ries, Numerical modeling and prediction of irreversibilities in sub- and supercritical turbulent near-wall flows, Ph.D. thesis, Technische Universitat Darmstad (2018).

[10] M. L. Shur, P. R. Spalart, M. K. Strelets, A. K. Travin, Synthetic turbulence generators for RANS-LES interfaces in zonal simulations of aerodynamic and aeroacoustic problems, Flow, Turbulence and Combustion 93 (1) (2014) 63–92. doi:10.1007/s10494-014-9534-8.

[11] M. Billson, L.-E. Eriksson, L. Davidson, Jet noise modeling using synthetic anisotropic turbulence, in: 10th AIAA/CEAS Aeroacoustics Conference, American Institute of Aeronautics and Astronautics, 2004. doi:10.2514/6.2004-3028.

[12] S. Hickel, S. Hulshof, CFD 3 – Large Eddy Simulation reader - wall bounded turbulence.

[13] J. Kim, P. Moin, R. Moser, Turbulence statistics in fully developed channel flow at low reynolds number, Journal of Fluid Mechanics 177 (1987) 133–166. doi:10.1017/s0022112087000892.

[14] T. Norddine, S. Benhamadouche, Wall-resolved LES and URANS simulations of an axial flow on a cantilevered rod at a moderate reynolds number, EDF R&D.

[15] S. sheng Chen, M. W. Wambsganss, Parallel-flow-induced vibration of fuel rods, Nuclear Engineering and Design 18 (2) (1972) 253–278. doi:10.1016/0029-5493(72)90144-6.

[16] J. de Ridder, Computational analysis of flow-induced vibrations in fuel rod bundles of next generation nuclear reactors, Ph.D. thesis, Ghent University (2015).

[17] S. Kottapalli, A. Shams, A. Zuijlen, M. Pourquie, Numerical investigation of an advanced URANS based pressure fluctuation model to simulate non-linear vibrations of nuclear fuel rods due to turbulent parallel-flow, Annals of Nuclear Energy 128 (2019) 115–126. doi:10.1016/j.anucene.2019.01.001.

[18] A. Cioncolini, J. Silva-Leon, D. Cooper, M. K. Quinn, H. Iacovides, Axial-flow-induced vibration experiments on cantilevered rods for nuclear reactor applications, Nuclear Engineering and Design 338 (2018) 102–118. doi:10.1016/j.nucengdes.2018.08.010.

[19] J. Salachna, A. Cioncolini, H. Iacovides, Benchmark simulation of the flow-induced vibrations for nuclear applications, SSRN Electronic Journal (2022). doi:10.2139/ssrn.4102496.

[20] A. J. B. John R. Lamarsh, Introduction to nuclear engineering, 2001.

[21] I. N. S. A. G. (INSAG), The chernobyl accident: Updating of insag-1, Tech. rep., International Atomic Energy Agency (IAEA) (1992).

[22] The fukushima daiichi accident, Tech. rep., International Atomic Energy Agency (IAEA) (2011).

[23] The tmi-2 accident: A summary of events and consequences, Tech. rep., Nuclear Regulatory Commission (NRC) (1980).

[24] Global warming of 1.5°c, Tech. rep., Intergovernmental Panel on Climate Change (IPCC) (2018).

[25] D. J. MacKay, Sustainable Energy - Without the Hot Air, 2009.

[26] J. Lovelock, Nuclear Power: The Energy Solution, Basic Books, 2006.

[27] Y. Shu, J. Wu, Y. Yang, Z. Zhao, Fretting wear and fatigue life analysis of fuel bundles subjected to turbulent axial flow in CEFR, Science and Technology of Nuclear Installations 2019 (2019) 1–11. doi:10.1155/2019/5613737.

[28] D. S. Weaver, S. Ziada, M. K. Au-Yang, S. S. Chen, M. P. Paı¨doussis, M. J. Pettigrew, Flow-induced vibrations in power and process plant components—progress and prospects, Journal of Pressure Vessel Technology 122 (3) (2000) 339–348. doi:10.1115/1.556190.

[29] D. Basile, J. Fauré, E. Ohlmer, Experimental study on the vibrations of various fuel rod models in parallel flow, Nuclear Engineering and Design 7 (6) (1968) 517–534. doi:10.1016/0029-5493(68)90102-7.

[30] M. P. Paidoussis, An experimental study of vibration of flexible cylinders induced by nominally axial flow, Nuclear Science and Engineering 35 (1) (1969) 127–138. doi:10.13182/nse69-a21121.

[31] M. Wambsganss, S. Chen, Tentative design guide for calculating the vibration response of flexible cylindrical elements in axial flow, Tech. rep. (jan 1971). doi:10.2172/4020578.

[32] J. D. Ridder, J. Degroote, K. V. Tichelen, P. Schuurmans, J. Vierendeels, Modal characteristics of a flexible cylinder in turbulent axial flow from numerical simulations, Journal of Fluids and Structures 43 (2013) 110–123. doi:10.1016/j.jfluidstructs.2013.09.001.

[33] D. D. Santis, A. Shams, An advanced numerical framework for the simulation of flow induced vibration for nuclear applications, Annals of Nuclear Energy 130 (2019) 218–231. doi:10.1016/j.anucene.2019.02.049.

[34] N. van den Bos, Turbulence-induced vibrations prediction through use of an anisotropic pressure fluctuation model, Master's thesis, TU Delft (2022).

[35] M. Pettigrew, C. Taylor, N. Fisher, M. Yetisir, B. Smith, Flow-induced vibration: recent findings and open questions, Nuclear Engineering and Design 185 (2-3) (1998) 249–276. doi:10.1016/s0029-5493(98)00238-6.

[36] M. P. Paidoussis, The amplitude of fluid-induced vibration of cylinders in axial flow (1965).

[37] S. Rinaldi, Experiments on the dynamics of cantilevered pipes subjected to internal and/or external axial flow, Ph.D. thesis (2009).

[38] G. Ricciardi, S. Bellizzi, B. Collard, B. Cochelin, Modelling pressurized water reactor cores in terms of porous media, Journal of Fluids and Structures 25 (1) (2009) 112–133. doi:10.1016/j.jfluidstructs.2008.04.002.

[39] S.-S. Chen, Flow-induced vibration of circular cylindrical structures, Tech. rep. (jun 1985). doi:10.2172/6331788.

[40] M. P. Paidoussis, Fluid-Structure Interactions: Volume 2, Elsevier, 2016.

[41] Divaret, Normal forces exerted upon a long cylinder oscillating in an axial flow, Journal of Fluid Mechanics 752 (2014) 649–669.

[42] Paidoussis, Linear and nonlinear dynamics of cantilevered cylinders in axial flow. part 1: physical dynamics, Journal of Fluids and Structures 16 (2002) 691–713.

[43] S. Rinaldi, M. P. Pai¨doussis, Dynamics of a free-clamped cylinder in confined axial flow, in: Volume 4: Fluid-Structure Interaction, ASMEDC, 2011. doi:10.1115/pvp2011-58038.

[44] S. Rinaldi, M. P. Païdoussis, Theory and experiments on the dynamics of a free-clamped cylinder in confined axial air-flow, Journal of Fluids and Structures 28 (2012) 167–179. doi:10.1016/j.jfluidstructs.2011.07.006.

[45] J. Kadlec, E. Ohlmer, On the reproducibility of the parallel-flow induced vibration of fuel pins, Nuclear Engineering and Design 17 (3) (1971) 355–360. doi:10.1016/0029-5493(71)90097-5.

[46] H. Higuchi, P. van Langen, H. Sawada, C. Tinney, Axial flow over a blunt circular cylinder with and without shear layer reattachment, Journal of Fluids and Structures 22 (6-7) (2006) 949–959. doi:10.1016/j.jfluidstructs.2006.04.020.

[47] H. Higuchi, H. Sawada, H. Kato, Sting-free measurements on a magnetically supported right circular cylinder aligned with the free stream, Journal of Fluid Mechanics 596 (2008) 49–72. doi:10.1017/s0022112007008956.

[48] R. Camussi, M. Felli, F. Pereira, G. Aloisio, A. D. Marco, Statistical properties of wall pressure fluctuations over a forward-facing step, Physics of Fluids 20 (7) (jul 2008). doi:10.1063/1.2959172.

[49] Z. Liu, Y. Liu, J. Lu, Numerical simulation of the fluid–structure interaction for an elastic cylinder subjected to tubular fluid flow, Computers &amp Fluids 68 (2012) 192–202. doi:10.1016/j.compfluid.2012.08.010.

[50] Z. Liu, Y. Liu, J. Lu, Numerical simulation of the fluid–structure interaction for two simple fuel assemblies, Nuclear Engineering and Design 258 (2013) 1–12. doi:10.1016/j.nucengdes.2013.01.029.

[51] M. A. Christon, R. Lu, J. Bakosi, B. T. Nadiga, Z. Karoutas, M. Berndt, Large-eddy simulation, fuel rod vibration and grid-to-rod fretting in pressurized water reactors, Journal of Computational Physics 322 (2016) 142–161. doi:10.1016/j.jcp.2016.06.042.

[52] S. Benhamadouche, P. Moussou, C. L. Maitre, CFD estimation of the flow-induced vibrations of a fuel rod downstream a mixing grid, in: Volume 4: Fluid-Structure Interaction, ASMEDC, 2009. doi:10.1115/pvp2009-78054.

[53] A. Elmahdi, Flow induced vibration forces on a fuel rod by LES CFD analysis, International Topical Meeting on Nuclear Reactor Thermalhydraulics, 2011.

[54] F. Roelofs, D. Dovizio, H. Uitslag-Doolaard, D. D. Santis, A. Mathur, B. Mikuz, A. Shams, Core thermal hydraulic CFD support for liquid metal reactors, Nuclear Engineering and Design 355 (2019) 110322. doi:10.1016/j.nucengdes.2019.110322.

[55] H. Dolfen, S. Vandewalle, J. Degroote, Effect of stochastic deformation on the vibration characteristics of a tube bundle in axial flow, Nuclear Engineering and Design 411 (2023) 112412. doi:10.1016/j.nucengdes.2023.112412.

[56] C. Liu, A. Papukchiev, R. Macián-Juan, Uncertainty and sensitivity analysis of coupled multiscale simulations in the context of the SESAME EU-project, International Journal of Advanced Nuclear Reactor Design and Technology 2 (2020) 117–130. doi:10.1016/j.jandt.2020.11.002.

[57] H.-J. Bungartz, M. Schäfer (Eds.), Fluid-Structure Interaction, Springer Berlin Heidelberg, 2006. doi:10.1007/3-540-34596-5.

[58] M. Paz, Y. H. Kim, Structural Dynamics, Springer International Publishing, 2019. doi:10.1007/978-3-319-94743-3.

[59] Nonlinear finite elements for continua and structures, Choice Reviews Online 38 (07) (2001) 38–3926–38–3926. doi:10.5860/choice.38-3926.

[60] H. G. Weller, G. Tabor, H. Jasak, C. Fureby, A tensorial approach to computational continuum mechanics using object-oriented techniques, Computers in Physics 12 (6) (1998) 620. doi:10.1063/1.168744.

[61] B. Leonard, A stable and accurate convective modelling procedure based on quadratic upstream interpolation, Computer Methods in Applied Mechanics and Engineering 19 (1) (1979) 59–98. doi:10.1016/0045-7825(79)90034-3.

[62] J. P. V. Doormaal, G. D. Raithby, Enhancements of the simple method for predicting incompressible fluid flows, Numerical Heat Transfer 7 (2) (1984) 147–163. doi:10.1080/01495728408961817.

[63] H.-J. Bungartz, F. Lindner, B. Gatzhammer, M. Mehl, K. Scheufele, A. Shukaev, B. Uekermann, preCICE – a fully parallel library for multi-physics surface coupling, Computers & Fluids 141 (2016) 250–258.

[64] S. Turek, J. Hron, Proposal for numerical benchmarking of fluid-structure interaction between an elastic object and laminar incompressible flow, in: Lecture Notes in Computational Science and Engineering, Springer Berlin Heidelberg, pp. 371–385. doi:10.1007/3-540-34596-5_15.

[65] E. Lillberg, Tailored experiments for validation of cfd with fsi for nuclear applications, NURETH-16 (2015).

[66] C. Liu, Fluid-structure interaction for a cantilever rod in axial flow: An experimental study, Ph.D. thesis, University of Manchester (2017).

[67] Introduction, in: An Informal Conceptual Introduction to Turbulence, Springer Netherlands, 2009, pp. 1–33. doi:10.1007/978-90-481-3174-7_1.

[68] J. L. L. H. Tennekes, A first course in turbulence, The MIT Press, 1972.

[69] L. F. Richardson, Weather Prediction by Numerical Process, Cambridge University Press, 1922.

[70] The local structure of turbulence in incompressible viscous fluid for very large reynolds numbers, Proceedings of the Royal Society of London. Series A: Mathematical and Physical Sciences 434 (1890) (1991) 9–13. doi:10.1098/rspa.1991.0075.

[71] M. S. Chong, J. Soria, A. E. Perry, J. Chacin, B. J. Cantwell, Y. Na, Turbulence structures of wall-bounded shear flows found using DNS data, Journal of Fluid Mechanics 357 (1998) 225–247. doi:10.1017/s0022112097008057.

[72] Y. Wang, Y. Yang, G. Yang, C. Liu, DNS study on vortex and vorticity in late boundary layer transition, Communications in Computational Physics 22 (2) (2017) 441–459. doi:10.4208/cicp.oa-2016-0183.

[73] L. Agostini, E. Touber, M. A. Leschziner, Spanwise oscillatory wall motion in channel flow: Drag-reduction mechanisms inferred from dns- predicted phase-wise property variations at Re = 1000, in: Proceeding of Eighth International Symposium on Turbulence and Shear Flow Phenomena, Begellhouse, 2013. doi:10.1615/tsfp8.1310.

[74] R. D. Moser, J. Kim, N. N. Mansour, Direct numerical simulation of turbulent channel flow up to Re_τ=590, Physics of Fluids 11 (4) (1999) 943–945. doi:10.1063/1.869966.

[75] T. Tsukahara, Y. Seki, H. Kawamura, D. Tochio, DNS of turbulent channel flow at very low reynolds numbers, in: Proceeding of Fourth International Symposium on Turbulence and Shear Flow Phenomena, Begellhouse, 2005. doi:10.1615/tsfp4.1550.

[76] D. Carati, G. S. Wicklemans, H. Jeanmart, On the modelling of the subgrid-scale and filtered-scale stress tensors in large-eddy simulation, Journal of Fluid Mechanics 441 (2001) 119–138. doi:10.1017/s0022112001004773.

[77] S. Krajnović, L. Davidson, Large-eddy simulation of the flow around simplified car model, in: SAE Technical Paper Series, SAE International, 2004. doi:10.4271/2004-01-0227.

[78] IV. On the dynamical theory of incompressible viscous fluids and the determination of the criterion, Philosophical Transactions of the Royal Society of London. (A.) 186 (1895) 123–164. doi:10.1098/rsta.1895.0004.

[79] D. C. Wilcox, Turbulence modelling for CFD, DCW industries, 2006.

[80] D. B. Spalding, Kolmogorov's two-equation model of turbulence., Proceedings: Mathematical and Physical Sciences 434 (1890) (1991) 211–216.

[81] W. Jones, B. Launder, The prediction of laminarization with a two-equation model of turbulence, International Journal of Heat and Mass Transfer 15 (2) (1972) 301–314. doi:10.1016/0017-9310(72)90076-2.

[82] F. Menter, Zonal two equation $k-\omega$ turbulence models for aerodynamic flows, in: 23rd Fluid Dynamics, Plasmadynamics, and Lasers Conference, American Institute of Aeronautics and Astronautics, 1993. doi:10.2514/6.1993-2906.

[83] F. Lien, W. Chen, M. Leschziner, Low-reynolds-number eddy-viscosity modelling based on non-linear stress-strain/vorticity relations, in: Engineering Turbulence Modelling and Experiments, Elsevier, 1996, pp. 91–100. doi:10.1016/b978-0-444-82463-9.50015-0.

[84] J. Z. T.H. Shih, J. Lumley, A realizable reynolds stress algebraic equation model, NASA Technical Memorandum 105993 (1993).

[85] V. Yakhot, S. A. Orszag, S. Thangam, T. B. Gatski, C. G. Speziale, Development of turbulence models for shear flows by a double expansion technique, Physics of Fluids A: Fluid Dynamics 4 (7) (1992) 1510–1520. doi:10.1063/1.858424.

[86] T.-H. Shih, W. W. Liou, A. Shabbir, Z. Yang, J. Zhu, A new $k-\epsilon$ eddy viscosity model for high reynolds number turbulent flows, Computers & Fluids 24 (3) (1995) 227–238. doi:10.1016/0045-7930(94)00032-t.

[87] B. E. Launder, G. J. Reece, W. Rodi, Progress in the development of a reynolds-stress turbulence closure, Journal of Fluid Mechanics 68 (3) (1975) 537–566. doi:10.1017/s0022112075001814.

[88] C. G. Speziale, S. Sarkar, T. B. Gatski, Modelling the pressure–strain correlation of turbulence: an invariant dynamical systems approach, Journal of Fluid Mechanics 227 (1991) 245–272. doi:10.1017/s0022112091000101.

[89] J. Rotta, Statistische theorie nichthomogener turbulenz, Zeitschrift for Physik 129 (6) (1951) 547–572. doi:10.1007/bf01330059.

[90] C. D. Donaldson, A computer study of an analytical model of boundary-layer transition., AIAA Journal 7 (2) (1969) 271–278. doi:10.2514/3.5085.

[91] B. J. Daly, Transport equations in turbulence, Physics of Fluids 13 (11) (1970) 2634. doi:10.1063/1.1692845.

[92] J. Lumley, A model for computation of stratified turbulent flows, Int. Symp. on Stratified Flow (1972).

[93] S. C. Crow, Viscoelastic properties of fine-grained incompressible turbulence, Journal of Fluid Mechanics 33 (1) (1968) 1–20. doi:10.1017/s0022112068002314.

[94] W. Reynolds, Computation of turbulent flows-state-of-the-art, Stanford University Mech. (1970).

[95] S. Wallin, A. V. Johansson, An explicit algebraic reynolds stress model for incompressible and compressible turbulent flows, Journal of Fluid Mechanics 403 (2000) 89–132. doi:10.1017/s0022112099007004.

[96] R. Laraufie, S. Deck, Assessment of reynolds stresses tensor reconstruction methods for synthetic turbulent inflow conditions. application to hybrid RANS/LES methods, International Journal of Heat and Fluid Flow 42 (2013) 68–78. doi:10.1016/j.ijheatfluidflow.2013.04.007.

[97] G. J. Kunkel, I. Marusic, Study of the near-wall-turbulent region of the high-reynolds-number boundary layer using an atmospheric flow, Journal of Fluid Mechanics 548 (-1) (2006) 375. doi:10.1017/s0022112005007780.

[98] D. Wilcox, M. W. Rubesin, Progress in turbulence modeling for complex flow fields including effects of compressibility (1980).

[99] C. Geng, G. He, Y. Wang, C. Xu, A. Lozano-Durán, J. M. Wallace, Taylor's hypothesis in turbulent channel flow considered using a transport equation analysis, Physics of Fluids 27 (2) (2015) 025111. doi:10.1063/1.4908070.

[100] W. K. George, The decay of homogeneous isotropic turbulence, Physics of Fluids A: Fluid Dynamics 4 (7) (1992) 1492–1509. doi:10.1063/1.858423.

[101] T. Deng, An improved inflow turbulence generator for large eddy simulation evaluation of wind effects on tall buildings, Engineering applications of computational fluid mechanics 17 (2023).

[102] D. Kleinhans, R. Friedrich, A. P. Schaffarczyk, J. Peinke, Synthetic turbulence models for wind turbine applications, in: Springer Proceedings in Physics, Springer Berlin Heidelberg, 2009, pp. 111–114. doi:10.1007/978-3-642-02225-8_26.

[103] T. Kitagawa, T. Nomura, A wavelet-based method to generate artificial wind fluctuation data, Journal of Wind Engineering and Industrial Aerodynamics 91 (7) (2003) 943–964. doi:10.1016/s0167-6105(03)00037-0.

[104] J. Schmiegel, J. Cleve, H. C. Eggers, B. R. Pearson, M. Greiner, Stochastic energy-cascade model for (11)-dimensional fully developed turbulence, Physics Letters A 320 (4) (2004) 247–253. doi:10.1016/j.physleta.2003.11.025.

[105] S. Sharma, Numerical study of turbulence induced vibrations using synthetic fluctuation field modeling in nuclear reactor applications, Master's thesis, TU Delft (2017).

[106] M. Pamiès, P.-É. Weiss, E. Garnier, S. Deck, P. Sagaut, Generation of synthetic turbulent inflow data for large eddy simulation of spatially evolving wall-bounded flows, Physics of Fluids 21 (4) (2009) 045103. doi:10.1063/1.3103881.

[107] A. Keating, U. Piomelli, E. Balaras, H.-J. Kaltenbach, A *priori* and a *posteriori* tests of inflow conditions for large-eddy simulation, Physics of Fluids 16 (12) (2004) 4696–4712. doi:10.1063/1.1811672.

[108] J. U. Schlüter, H. Pitsch, P. Moin, Large-eddy simulation inflow conditions for coupling with reynolds-averaged flow solvers, AIAA Journal 42 (3) (2004) 478–484. doi:10.2514/1.3488.

[109] N. Li, E. Balaras, U. Piomelli, Inflow conditions for large-eddy simulations of mixing layers, Physics of Fluids 12 (4) (2000) 935–938. doi:10.1063/1.870346.

[110] N. S. Dhamankar, G. A. Blaisdell, A. S. Lyrintzis, An overview of turbulent inflow boundary conditions for large eddy simulations (invited), in: 22nd AIAA Computational Fluid Dynamics Conference, American Institute of Aeronautics and Astronautics, 2015. doi:10.2514/6.2015-3213.

[111] X. Wu, Inflow turbulence generation methods, Annual Review of Fluid Mechanics 49 (1) (2017) 23–49. doi:10.1146/annurev-fluid-010816-060322.

[112] F. G. Aguilera, J. R. Gill, X. Zhang, X. Chen, T. Node-Langlois, Leading edge noise predictions using anisotropic synthetic turbulence, in: 22nd AIAA/CEAS Aeroacoustics Conference, American Institute of Aeronautics and Astronautics, 2016. doi:10.2514/6.2016-2840.

[113] R. Ewert, J. Dierke, J. Siebert, A. Neifeld, C. Appel, M. Siefert, O. Kornow, CAA broadband noise prediction for aeroacoustic design, Journal of Sound and Vibration 330 (17) (2011) 4139–4160. doi:10.1016/j.jsv.2011.04.014.

[114] C. Bailly, D. Juve, A stochastic approach to compute subsonic noise using linearized euler's equations, in: 5th AIAA/CEAS Aeroacoustics Conference and Exhibit, American Institute of Aeronautics and Astronautics, 1999. doi:10.2514/6.1999-1872.

[115] D. Adamian, A. Travin, An efficient generator of synthetic turbulence at RANS–LES interface in embedded LES of wall-bounded and free shear flows, in: Computational Fluid Dynamics 2010, Springer Berlin Heidelberg, 2011, pp. 739–744. doi:10.1007/978-3-642-17884-9_94.

[116] N. Jarrin, R. Prosser, J.-C. Uribe, S. Benhamadouche, D. Laurence, Reconstruction of turbulent fluctuations for hybrid RANS/LES simulations using a synthetic-eddy method, International Journal of Heat and Fluid Flow 30 (3) (2009) 435–442. doi:10.1016/j.ijheatfluidflow.2009.02.016.

[117] L. Davidson, M. Billson, Hybrid LES-RANS using synthesized turbulent fluctuations for forcing in the interface region, International Journal of Heat and Fluid Flow 27 (6) (2006) 1028–1042. doi:10.1016/j.ijheatfluidflow.2006.02.025.

[118] S. Arvidson, S.-H. Peng, L. Davidson, Feasibility of hybrid RANS-LES modeling of shock/boundary-layer interaction in a duct, in: Progress in Hybrid RANS-LES Modelling, Springer Berlin Heidelberg, 2012, pp. 245–256. doi:10.1007/978-3-642-31818-4_21.

[119] P. R. Spalart, The 2007 hybrid RANS-LES symposium: An outsider's view, in: Notes on Numerical Fluid Mechanics and Multidisciplinary Design, Springer Berlin Heidelberg, pp. 1–9. doi:10.1007/978-3-540-77815-8_1.

[120] G. Comte-Bellot, S. Corrsin, Simple eulerian time correlation of full-and narrow-band velocity signals in grid-generated, 'isotropic' turbulence, Journal of Fluid Mechanics 48 (2) (1971) 273–337. doi:10.1017/s0022112071001599.

[121] R. Poletto, T. Craft, A. Revell, A new divergence free synthetic eddy method for the reproduction of inlet flow conditions for LES, Flow, Turbulence and Combustion 91 (3) (2013) 519–539. doi:10.1007/s10494-013-9488-2.

[122] H. Abe, H. Kawamura, Y. Matsuo, Direct numerical simulation of a fully developed turbulent channel flow with respect to the reynolds number dependence, Journal of Fluids Engineering 123 (2) (2001) 382–393. doi:10.1115/1.1366680.

[123] J. M. Wallace, H. Eckelmann, R. S. Brodkey, The wall region in turbulent shear flow, Journal of Fluid Mechanics 54 (1) (1972) 39–48. doi:10.1017/s0022112072000515.

[124] J. M. Wallace, Quadrant analysis in turbulence research: History and evolution, Annual Review of Fluid Mechanics 48 (1) (2016) 131–158. doi:10.1146/annurev-fluid-122414-034550.

[125] Z. W. Hu, C. L. Morfey, N. D. Sandham, Wall pressure and shear stress spectra from direct simulations of channel flow, AIAA Journal 44 (7) (2006) 1541–1549. doi:10.2514/1.17638.

[126] T. A. Brungart, G. C. Lauchle, S. Deutsch, E. T. Riggs, Outer-flow effects on turbulent boundary layer wall pressure fluctuations, The Journal of the Acoustical Society of America 105 (4) (1999) 2097–2106. doi:10.1121/1.426815.

[127] H. Abe, Y. Matsuo, H. Kawamura, A DNS study of Reynolds number dependence on pressure fluctuations in a turbulent channel flow, in: Proceeding of Fourth International Symposium on Turbulence and Shear Flow Phenomena, Begellhouse, 2005. doi:10.1615/tsfp4.320.

[128] T. Nazari, A. Rabiee, H. Kazeminejad, Two-way fluid-structure interaction simulation for steady-state vibration of a slender rod using URANS and LES turbulence models, Nuclear Engineering and Technology 51 (2) (2019) 573–578. doi:10.1016/j.net.2018.10.011.

[129] H. G. Castro, R. R. Paz, A time and space correlated turbulence synthesis method for large eddy simulations, Journal of Computational Physics 235 (2013) 742–763. doi:10.1016/j.jcp.2012.10.035.

This page intentionally left blank.

This page intentionally left blank.

Delft University of Technology

TU Delft